Designing Metal-Substituted WB_2 and MoB_2 as Efficient Bifunctional Electrocatalysts for Hydrogen and Oxygen Evolution Reactions

by

Ezgi Hatipoğlu

A Dissertation Submitted to the
Graduate School of Sciences and Engineering
in Partial Fulfillment of the Requirements for
the Degree of

Master of Science

in

Materials Science and Engineering

June 21, 2022

Designing Metal-Substituted WB_2 and MoB_2 as Efficient Bifunctional Electrocatalysts for Hydrogen and Oxygen Evolution Reactions

Koç University

Graduate School of Sciences and Engineering

This is to certify that I have examined this copy of a master's thesis by

Ezgi Hatipoğlu

and have found that it is complete and satisfactory in all respects,
and that any and all revisions required by the final
examining committee have been made.

Committee Members:

_____

Asst. Prof. Umut Aydemir (Advisor)

_____

Assoc. Prof. Uğur Ünal

_____

Assoc. Prof. Ferdi Karadaş

Date: 21.06.2022

To my lovely family…

ABSTRACT

Designing Metal-Substituted WB_2 and MoB_2 as Efficient Bifunctional Electrocatalysts for Hydrogen and Oxygen Evolution Reactions

Ezgi Hatipoğlu

Master of Science in Materials Science and Engineering

June 21, 2022

Over the past few years, the ever-increasing global energy demand, environmental problems, and climate change have fostered researchers to focus on designing economic and competent catalysts to produce pure energy originating from renewable energy sources. Transition metal diborides (TMDbs) have recently attracted the scientific community's attention because of their remarkable attributes as bifunctional catalysts for both oxygen and hydrogen evolution reactions (OER/HER) with excellent durability in alkaline media. The prominent features, such as superior electronic conductivity and a high density of active sites, are dominated in the 3D framework of MDbs due to the presence of due to the presence of borophene subunits as. In this thesis, metal substituted WB_2 and MoB_2 were investigated under the alkaline medium as promising electrocatalysts for OER/HER by comparing different substitution transition metals (Ni and Co), variety for concentration in the structure (x = 0, 0.1, 0.2, and 0.3 even higher for MoB_2), and two alternative synthesis techniques (molten salt-assisted (ms) and carbothermal reduction (ct)). The aim was to control the crystal structure and morphology, and tailor the electronic structure to optimize adsorption-desorption features on the surface. The results unraveled a general fact that materials synthesized by the molten-salt technique turned to be relatively better catalysts toward OER/HER. In particular, $W_{0.8}Co_{0.2}B_2$/ms demanded the lowest respective overpotentials of 340 and 363 mV to generate a current density of 10 mA cm^{-2} for OER/HER. While $Mo_{0.8}Co_{0.2}B_2$/ms provided 340 mV to reach 10 mA cm^{-2} for OER, $Mo_{0.9}Ni_{0.1}B_2$/ms ensured 220 mV overpotential for HER as a further improvement. Besides enhancement in overpotentials, $W_{0.8}Co_{0.2}B_2$/ms displayed durability of 12 h against OER/HER. For MoB_2 electrocatalysts, $Mo_{0.9}Ni_{0.1}B_2$/ms showed excellent HER stability for 12 h. Thanks to controlling the nano-size of the particles, their homogeneous distribution throughout the

samples, and keeping the layered structure for both metal diborides, the molten salt-assisted technique led to electrocatalysts with better electrocatalytic activity compared to the carbothermal reduction. These results demonstrate that layered metal diborides possess great potential as electrocatalyst toward hydrogen and oxygen evolution reactions.

ÖZETÇE

Hidrojen ve Oksijen Oluşum Reaksiyonları İçin Verimli ve İki Fonksiyonlu Metal Katkılı WB_2 ve MoB_2 Elektrokatalizörlerin Dizaynı

Ezgi Hatipoğlu
Malzeme Bilimleri ve Mühendisliği, Yüksek Lisans
21 Haziran 2022

Son yıllarda, enerjiye olan ihtiyacın artması, çevresel problemler ve iklim değişiklikleri sebebiyle araştırmacılar yeni ekonomik katalizörler araştırmaya başlamıştır. Elde edilecek yeni işlevsel katalizörler sayesinde yenilenebilir enerji kaynaklarından saf enerji üretimi sağlanması amaçlanmaktadır. Geçiş metalleri temelli borürler, dikkate değer özellikleri sayesinde hem hidrojen hem de oksijen oluşum reaksiyonları (HER ve OER, sırasıyla) için iki işlevli ve çok iyi kararlılıkları sayesinde göz önünde bulunmaktadır. Önde gelen elektronik iletkenlikleri ve yüksek yoğunlukta bulunan aktif bölgeleri gibi özelliklerinin başlıca sebebi 3 boyutlu sistemlerinde bulunan 2 boyutlu katmanlı yapıyı sağlayan bor alt kümeleridir. Bu tez çalışmasında, farklı geçiş metalleri (Ni ve Co) ve konsantrasyon oranlarıyla (x = 0, 0.1, 0.2, ve 0.3 hatta MoB_2 için daha fazla) katkılanmış, farklı iki alternatif yöntem ile sentezlenmiş (erimiş tuz ile asiste edilmiş ve karbotermal indirgeme yöntemi) metal katkılı WB_2 ve MoB_2 incelenmiştir. Amaç, kristal yapının ve morfolojinin kontrol edilerek, yüzeydeki elektronik yapının uygun hale getirilmesi ve yüzeye tutunma ve ayrılma özelliklerinin optimize edilmesidir. Sonuçlar göstermiştir ki erimiş tuz yardımıyla sentezlenen elektrokatalizörler hem OER hem HER için daha iyi özellik göstermiştir. Özellikle $W_{0.8}Co_{0.2}B_2$/ms örneği, OER için 340 mV aşırıgerilimi ile 10 mA cm^{-2} akım yoğunluğuna ulaşırken, HER için 363 mV ile ulaşmıştır. Benzer olarak, $Mo_{0.8}Co_{0.2}B_2$/ms elektrokatalizörü de 340 mV aşırıgerilimi ile OER ulaşırken, $Mo_{0.9}Ni_{0.1}B_2$/ms örneği daha da iyi bir ilerleme göstererek sadece 220 mV ile HER performansı vermiştir. Bu incelemelere ek olarak, $W_{0.8}Co_{0.2}B_2$/ms hem OER hem HER için 12 saat boyunca çok iyi bir kararlılık göstermiştir. Ancak, $Mo_{0.9}Ni_{0.1}B_2$/ms elektrokimyasal performansını diğerlerine göre en az kaybederek 12 saat boyunca mükemmel bir HER kararlılığı göstermiştir. Sonuç olarak, nano boyuttaki tanecikler

kontrol edilerek, örneklerdeki homojen dağılım sağlanarak ve metal diborürlerdeki katmanlı yap korunarak, erimiş tuz yardımıyla sentezlenen elektrokatalizörler; mikron yapıda bulunan ve farklı faz yapılarının oluşmasına olanak tanıyan karbotermal indirgeme yöntemi ile sentezlenenlere kıyasla gözle görülür şekilde iyi performans göstermiştir. Bu sonuçlara göre, katmanlı metal diborürler, verimli elektrokatalizörler olarak hidrojen ve oksijen oluşum reaksiyonları için kullanılma potansiyeline sahiptir.

ACKNOWLEDGEMENTS

I would like to thank all the people in my life who supports and gives motivation for my academic studies.

Firstly, I would like to express my grateful feelings to my supervisor Asst. Prof. Umut Aydemir since he gave me opportunity to work with him, supported me in every hard time, and shared his knowledge and wisdom in scientific field.

I would like to thank my thesis committee members Assoc. Prof. Uğur Ünal and Assoc. Prof. Ferdi Karadaş for their time and consideration to improve my master's work and thesis.

I am very grateful since I met Dr. Naeimeh Sadat Peighambardoust. She always encouraged me for my academic studies and guided me to be a better researcher with her beneficial experience. Besides her academic contribution, she has become a sister to me I never want to lose. Thank you to be understanding person. I would like to thank Samet Aydın for his endless help in my experiments and laboratory adventure, and Ebrahim Sadeghi for his support in electrochemical contributions to my research.

Thank you to all the KUBAM family for sharing these times together Özden Güneş Yıldız, Melis Özen, Arda Baran Burçak, İlayda Terzi, Dr. Yaprak Subaşı, Sanaz Chamani, Verda Berşan Genceli, Res. Asst. Prof. Özge Balcı, and all the students that spent our time. I would like to express my gratefulness to again Assoc. Prof. Uğur Ünal and his students Armin Asghari Alamdari, and all the students who help me for my studies. Thanks to laboratory neighbours Bengisu Yılmaz and Ghazaleh Azizi Saadatlou hallway conservations that we shared. I would like to thank members of KUYTAM, especially Dr. Barış Yağcı and Dr. Amir Motallebzadeh for SEM and XPS analyses.

I would like to give special part to Müjde Yahyaoğlu for her great friendship and sisterhood, good memories that we shared and advice in laboratory experiences with full time support.

I would like to thank person who guided me for choosing this field as a lifestyle Dr. Ayşegül Akyürekli Toktaş, a lovely sister to me in my social life, a role model in my academic life. Also, I have to give a part to my valuable friends Betül Korkmaz, Saliha Irmak, Betül Tekin, Esenbüke Mürselim, Güllü Gültuğ Yün, Ecenaz Duygun, Burçin Uzuntaş and Aziz Berkay Önay. They always believed in me more than I did and have been my important source of motivation.

My very special thanks are for my dear friend Bilgehan Murat Şeşen who is with me during our undergraduate years and my master's adventure. He is always the biggest part of my inspiration, motivation, and personality.

Last but not least, my precious parents Sema and Vasfi Hatipoğlu, I cannot express my gratitude and respect to them. Whenever I had a problem, they were there for me. They always did the best they could, had sacrifices for me, shared my happiness, sadness, and stress that I have encountered. Thank you for being my family, my everything and making my life easier in every point. I would like to express gratitude to my older brother individually, the best engineer that I have seen, Görkem Hatipoğlu. I have always been inspired by him since I was little and have envied from him. He is the biggest reason why I chose this profession and continued with eagerly. What a joy if I was successful as half him. My precious family, thank you so much for making me the luckiest little girl in this world throughout my life. If I didn't have you, I wouldn't be able to achieve this success.

TABLE OF CONTENTS

LIST OF TABLES

LIST OF FIGURES

ABBREVIATIONS

TMB	Transition Metal Boride
EWS	Electrocatalytic Water Splitting
OER	Oxygen Evolution Reaction
HER	Hydrogen Evolution Reaction
AWE	Alkaline Water Electrolysis
MDB	Metal Diborides
RHE	Reversible Hydrogen Electrode
NHE	Normal Hydrogen Electrode
MS	Molten Salt-Assisted
CT	Carbothermal Reduction
XRD	X-ray Diffraction
SEM	Scanning Electron Microscopy
TEM	Transmission Electron Microscopy
XPS	X-Ray Photoelectron Microscopy
SAED	Selected Area Electron Diffraction
EIS	Electrochemical Impedance Spectroscopy
OCP	Open Circuit Potential
CV	Cyclic Voltammetry
SSA	Specific Surface Area
ECSA	Electrochemical Active Surface Area

Chapter 1: **INTRODUCTION**

With an exponential increase in global economic development, serious energy demand rises to satisfy industrial applications, transportation, electrical power, etc. When the commercial energy sources are considered, fossil ones such as oil, natural gas, and coal are at a higher rate than renewable sources due to the high amount of energy that provides for the applications, ease of storage, and transportation [1]. However, fossil energy sources are limited in our world, and considering an increase in the energy needed in even daily life, a faster run out of these sources is inevitable. Also, besides the limited quantity of fossil energy sources, they contribute to the global climate change from extraction, storage, and burning due to releasing a large number of greenhouse gases such as carbon dioxide and methane and causing global warming. So, global warming leads to changes in sea level, warming weather, loss of living beings, food scarcity, etc. To avoid these situations, there should be alternative sustainable energy sources which obtain from the world's unlimited sources such as sun, wind, and biomasses and provide a high amount of energy, delivering in a clean way efficiently and recycling-reusing ability [1].

Hydrogen is one of the most prominent energy carriers in terms of sustainability, zero-carbon content, and clean transportation to reduce the usage of fossil fuels. Obtaining hydrogen from water as an electrolysis process presents a simple and efficient way. Renewable energy sources get involved here by making the reaction to obtain hydrogen and oxygen from water which utilizes directly with lower or no external power supply. There are several green energy systems for splitting water by taking advantage of renewable sources: solar cells, thermoelectric, photoelectrode, pyroelectric, electric energy devices, etc. [2]. Electrochemical splitting of water in electric energy devices provides a highly sustainable feature in obtaining molecular hydrogen directly from electricity and being environmentally friendly due to process steps [1], [2].

Electrochemical water splitting (EWS) depends on the two half-cell reactions: cathodic reduction reaction and anodic oxidation reaction and requires 1.23 V in theory thermodynamically. However, there is an overpotential need to overcome activation potential in the process caused by electron transfer kinetics. To handle this situation, the required overpotential should be diminished by designing electrocatalysts and tuning the expected features of electrocatalysts [1], [2].

When the best-performance electrocatalysts are investigated, Pt/C and RuO_2 become the lead of noble metals and their oxides for hydrogen and oxygen evolution reaction (HER and OER), respectively. However, there are limitations to the commercialization of these electrocatalysts due to the scarcity of these elements on earth and their high cost. To make this process feasible, alternative electrocatalysts should be designed by having properties such as highly efficient performance like noble metals, viable, sustainable, and cheap. In this regard, transition metal (TM)-based (Fe, Co, Ni-based) electrocatalysts have been investigated because of the high number of sources on earth, cheaper than noble metals, efficient electrochemical properties, and synthesizing in an ease way for desired shape and structure. Researchers have found that TM-based sulfides, phosphides, selenides, and borides become important alternatives in HER and OER due to having similar kinetics at all pH valuesa good activity for EWS [3].

Among them, metal borides (MDBs) come forward since they have borophene subunits in the 3D framework which provides high electrical and thermal conductivity, better chemical stability, and a high density of active sites [4], [5]. According to the recent studies on MDBs, there is a linear relationship between the catalytic activity and the d-band center of that metal diboride, proven by density functional theory (DFT) calculations (Park et al., 2019). From this research, TaB_2, VB2, α-MoB_2, and WB_2 show this linear relationship and give the best HER performance from left to right while closing the Pt most.

However, besides the DFT works in this type of electrocatalysts, there are a limited number of publications in the MDBs for the EWS field. The most prominent reasons are why MDBs require high temperature and pressure conditions to synthesize, and there are close stoichiometric ratios with their other compounds. Also, since MDBs have been a new electrocatalysts family, there is a vast need about their synthesis conditions for EWS, electrocatalytic activity, and sustainable features.

To fill these spaces, this thesis focuses on the electrochemical properties of tungsten diboride (WB_2) and molybdenum diboride (MoB_2) to catalyze both HER and OER separately. Main subjects will gain better electrocatalytic performance for EWS systems while optimizing the synthesis conditions, tailoring the structure and properties with phase engineering, morphological investigations, substitutional metal defects, surface oxidation, etc. The second chapter includes the literature review about EWS principles, the mechanism of HER and OER, important parameters to evaluate the electrocatalytic

activity and MDB electrocatalysts, and recent studies about this type of family. The third chapter covers the main characterization methods and the measuring techniques of the equipment. In the fourth chapter, the experimental procedures, synthesis techniques, chemical characterization results with different methods, and electrochemical activity results of the samples will be discussed in detail. Lastly, the conclusion section will summarize all research output for this study.

1.1 Electrocatalytic Water Splitting

By concerning the need for sustainable energy sources throughout the world, hydrogen has been investigated as one of the favored energy carriers. Earth has a high amount of hydrogen existing in water and hydrocarbons. Obtaining hydrogen gas from these sources and utilizing it in the industry generally depends on the catalytic steam forming, which causes a vast amount of CO_2 emission and energy consumption [7]. The remaining parts of commercial production pathways of low-purity hydrogen gas, which are partial oxidation, coal gasification, and pyrolysis, contribute to CO_2 emission [8]. Water splitting is the smaller piece of commercial hydrogen gas production by only 4 % although it has been studied for 230 years [9]. In the Chlor-alkali industry, high purity (> 99.6%) hydrogen gas is produced with the byproduct of chlorine and caustic soda [10] . Finding a way to produce high-quality hydrogen gas in a sustainable and fossil-free way is an important concern due to the current energy needs on Earth. In these cases, renewable energy becomes involved in storing the hydrogen in the chemical bond form by using devices that can transform this energy into electricity for the related users [11].

The electrocatalytic water splitting system cells consist of the anode side for the oxygen evolution reaction (OER), the cathode side for the hydrogen evolution (HER), an electrolyte to transport the ions, and enclosed with the electrical circuit to transport the electrons. When the potential is applied to the system/cell, water is oxidized into oxygen at the anode and is reduced to hydrogen gas at the cathode. Thermodynamically, there should be ΔG= 237.1 kJ/mol energy input corresponding to 1.23 V potential to splitting water into oxygen and hydrogen at 25 ˚C and 1 atm, regardless of the electrolyte's pH [12]. However, due to the multi-step reactions and poor kinetics for both OER and HER, there should be higher applied overpotentials in the current EWS systems.

Hence, electrocatalysts are used in the electrodes' surfaces to improve the EWS in an efficient way by providing higher energy conversion. To reduce the required overpotential, different types of materials have been studied as electrocatalysts since EWS have been developed. These electrocatalysts should meet a couple of desired features. One of the essential properties in here that is being bifunctional for both OER and HER mechanisms by providing high activity. Until now, the desired activities for half-reactions from the noble metals have not been achieved as electrocatalysts due to the poor stability in the different mediums and slow charge transfer rate in various mechanisms. When bifunctional electrocatalysts are integrated into EWS systems **Figure 1** , commercialization of EWS will become faster since there will be no need to manufacture individual electrocatalysts for different mediums and equipment. The association in the usage will lead to decreasement in fabrication cost directly [1].

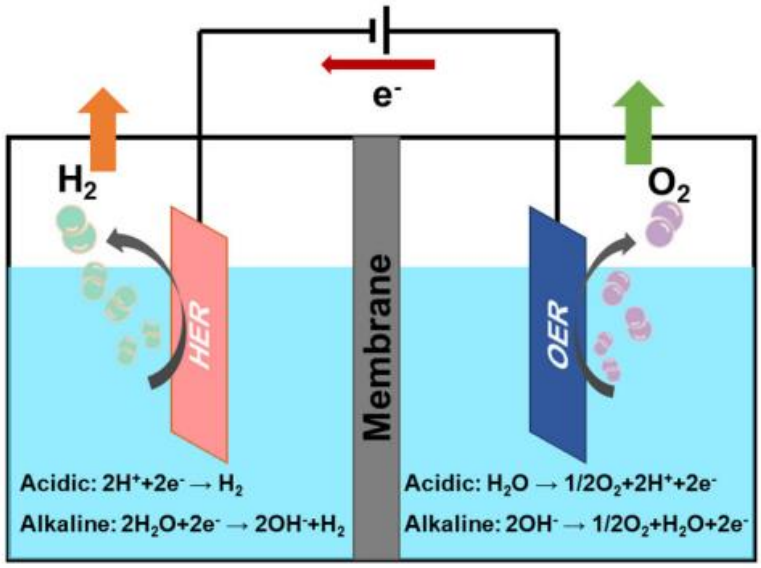

Figure 1. Schematic view of bifunctional electrocatalysts and water electrolysis system [13]

Up to date, the highest exchange current density and lowest overpotential for a wide pH range are obtained from noble metal electrocatalysts, which are Ir- and Ru- oxides for OER and Pt-based materials for HER [14]. Nonetheless, there is a limitation in the rate of commercialization of them since they have a low abundance on earth, high cost of synthesis and utilization, and low tolerance to passivation [10], [15].

When the sources of water on Earth are considered, less than 1 % of them is clean water. However, most of the electrolyzers, such as microbial and polymer electrolyte membrane (PEM), work with clean water and their pH range are different. For example,

microbial electrolyzers need a neutral medium, while PEM electrolyzers work under an extremely low pH range. Hence, the desired electrocatalysts should satisfy the same properties efficiently through various pH values and work with unclean water like seawater, oceans, or rain. The required pH range for rain is generally 4.2-6, while 8.1-9 for seawater [16]. Currently, finding the optimum electrocatalyst for these working conditions is the biggest concern for EWS systems.

In the literature, many research are based on the increase their catalytic activity by decreasing the percentage of noble metals with different procedures like surface modifications, doping of various elements, and chemical treatments [2]. For the noble metals, the best range is the acidic conditions by providing efficient and stable performance. In contrast, they have a high dissolution rate for operating in alkaline mediums due to HER kinetics. There is also a current trend to replace them entirely with nitrides, sulfides, carbides, and borides since transition metal-based materials provide low cost compared to noble metals, high chemical stability in various pH ranges, and high abundance [14].

The commercialization of alkaline water electrolysis (AWE) started in 1920 to satisfy the hydrogen energy need of the world by providing good durability, easy operation, and compability of non-precious metals [17]. Working conditions of industrial AWE are required 60-80 ˚C and 6-10 M KOH solution as medium [10]. Nevertheless, the overall cost for hydrogen production from AWE becomes higher due to the low current densities (0.2-0.4 $A.cm^{-2}$) and high ohmic losses, thereby being limited to stack systems' size [18]. When acidic electrolyzers like PEM are considered, they can provide higher current densities (closest to 2 $A.cm^{-2}$) but in extreme acidic pH values for noble metals. Lastly, neutral conditions are suitable for seawater applications as the most abundant water source on earth by delivering better stability due to less corrosive media. But ion poisoning is the side effect of electrocatalysts in these applications. The most common electrolyte solutions are 1 M KOH, 1 M PBS, and 0.5 M H2SO4 as alkaline, neutral, and acidic mediums, respectively [10].

1.2 Evolution parameters for EWS Half Reactions

1.2.1 Overpotential (η)

Theoretically, the standard reduction potential for HER is $E^0_{H/H2O}$= 0 V vs. reversible hydrogen electrode (RHE), while 1.23 V for OER [1]. There is a required potential to surpass an activation energy barrier due to the slow kinetics of two half-reactions which is defined as overpotential (η) in electrochemistry. Nernstian potential describes thermodynamic equilibrium potential (E_{RHE}) depending on pH, which can be nonvalid by referencing to RHE.

$E_{HER}= E^{0}_{(H^2/H^+)} – RT/F \times \ln (a_{H+} / P_{H2}^{½}) = -0.059 \times (pH)$ V vs. NHE = 0 V vs. RHE (1)

Nernstian potential increases linearly by 0.059 V for each pH increment in Equation (1), which equals zero versus the RHE scale directly. HER generally couldn't start at equilibrium in most cases and always requires a cathodic overpotential to overcome the activation barrier for that reaction. The interface of reaction gives information about the magnitude of the barrier. Applied potential (E) could be calculated from the Equation (2) for a specific current (i):

$$E = E_{RHE} + iR - \eta \quad (2)$$

In this formula, iR refers to the ohmic potential drop (iR compensation) related to the system's series resistances (R). There are three main reasons for overpotential for both half-reactions. Intrinsic activation overpotential can be decreased by using efficient materials such as electrocatalysts, while concentration overpotential decreases with stirring the electrolyte constantly. Resistance and current density multiplication could be beneficial to remove the overpotential caused by uncompensated resistance. These activities lead to smaller overpotential amounts and thereby higher activity for that reaction. The desired value from the HER catalyst to be reached should be less than 100 mV overpotential. But there are multiple effects of raising that activation barrier of the reaction. Providing a more active electrocatalyst on the electrode surface can minimize the activation barrier due to the interface relationships and reduce the required overpotentials for both OER and HER [4].

1.2.2 Tafel Plot (Tafel Slope and Exchange Current Density)

One of the critical parameters to evaluate and understand the electrocatalytic activity of materials is the Tafel plot, which is beneficial in terms of two important parameters: Tafel slope (b) and exchange current density (j_0). The linear part of the Tafel plot at the proper overpotential region gives the Tafel slope, which is obtained by fitting the i-E plot based on the Tafel equation as shown below:

$$\eta = a + b \log(j) \quad (3)$$

where η, a, b, and j are overpotential, Tafel constant, Tafel slope, and current density, respectively. The linear part of the plot can be drawn and obtained by replotting the polarization curve (linear sweep voltammogram as a $\log(|j|)$ versus η) [1] Tafel slope, as an intrinsic feature, is beneficial to getting knowledge about the reaction pathway and rate-determining step (RDS) of HER. In other words, the Tafel slope indicates the required overpotential to increase the current density for one order of magnitude [19]. A smaller Tafel slope leads to a steep rise of current density and means higher charge transferability. When the overpotential increases, the catalytic current increases sharply by smaller charge transfer coefficient which comes from smaller Tafel slope values [10].

The linear part of the Tafel plot also gives related data to derive exchange current density (j_0) by assuming the equilibrium condition for the reaction, which means overpotential equals to zero. So, exchange current density implies the rate at the potential at the thermodynamical equilibrium. As the best known HER electrocatalysts, Platinum has the highest j_0 value as 1 mA/cm^2 [11], [19]. The exchange current density changes according to the electrocatalysts' material, electrolyte, and temperature for the reaction and is the internal cause of the activation potential barrier.

To obtain higher overall activity, the optimum properties from an electrocatalyst should be smaller overpotential, lower Tafel slope, and larger exchange current density. But the lower Tafel slope sometimes expresses smaller current densities for HER electrocatalysts. By finding the limits of catalysts' performance for improvement, the required intrinsic properties should be tailored to lead to the best performance. In order to better comparison of HER electrocatalysts from the literature, the figure of merit for achieving the required potential is defined as 10 $mA.cm^{-2}$ current density [11].

1.3 Fundamentals of HER

HER is a simpler one between the two half-reactions of EWS processes since it occurs in only two steps. For this process, the reduction of protons takes place on the cathode side of the cell, and it requires two-electrons transfer for one molecule of H_2 production. During the HER process, a catalyst helps to compensate for the slow kinetics of proton absorption for the electrode surface by tailoring the desorption of hydrogen molecules [14]. Volmer adsorption and followed by desorption are the two steps for the HER. In the Volmer adsorption step, which is the first one that requires 120 mV/dec Tafel slope [14], there is a covering of H_2O or H^+ on the cathode by adsorption and binding of hydrogen intermediate to the catalysts:

$H_3O^+ + e^- \rightarrow H_{ads} + H_2O$

After the adsorption process, there are two possible pathways for obtaining H_2 and desorption from the cathode depending on the H_{ads} coverage, which are Tafel or Heyrovsky steps. HER kinetics are essential for determining the reaction pathway by controlling the catalyst. These two routes could be utilized simultaneously by having various crystalline facets on the single electrocatalysts' surface **Figure 2**. If H_{ads} has low coverage as in the electrochemical desorption step, the Heyrovsky process takes place with a 40 mV/dec Tafel slope [11]:

$H_{ads} + H^+ + e^- \rightarrow H_2$

However, suppose there is a higher H_{ads} coverage for the electrode surface. In that case, the second route occurs for the chemical desorption for H_2, which is the Tafel step (recombination reaction) with a lower Tafel slope of 30 mV/dec: [11].

$2\ H_{ads} \rightarrow H_2$

From the possible steps of the HER mechanism, the free energy of hydrogen ($\Delta G\ H_{ads}$) is a crucial feature for the electrocatalyst's activity descriptor since taking the place of adsorbed hydrogen. Sabatier's principles explain that there is a good balance relation (optimum bonding energy with intermediates) between the hydrogen bonding and desorption ability from the surface for an ideal HER catalyst without any change of pH. For the Platinum, as the highest HER activity electrocatalyst, $\Delta G\ H_{ads}$ is around 0 eV [10], [11]. Lower $\Delta G\ H_{ads}$ corresponds to stronger binding energy, so it slows down the hydrogen releasing. However, higher $\Delta G\ H_{ads}$ causes to endothermic proton/electron

transfer step [10]. Density functional theory (DFT) calculations analyze ΔG H_{ads} to specific elements.

An optimum HER catalyst should have a higher number of active sites with tailored electron density to have moderate bonding strength with adsorbed hydrogen to provide a desired relationship between the adsorption and desorption steps according to the Sabatier principle. Additionally, an ideal HER catalyst should have lower charge transfer resistance with the electrolyte and electrode interface while stabilizing long working hours [7]

In contrast to an acidic solution, many electrocatalysts lose their good HER activity when utilized in an alkaline solution due to the sluggish mechanisms of water dissociation. The kinetic barrier and its determination are important factors to analyze the intrinsic activity of electrocatalysts in HER with alkaline electrolytes [10].

The pH of the solution influences the H_2 molecule production pathway either reducing the water molecule or hydronium (H_3O^+). Hydronium replacement is the important key for hydrogen proton in acidic environments. But, having the low proton concentration may contribute to reduction of water molecule, too. For the neutral mediums, firstly reduction of water molecule occurs, but like acidic mediums, hydronium could occur in low concentrations. In alkaline mediums, water molecule reduction takes place due to the high current density utilization of water splitting cells [7].

Due to these changes in mechanisms, reaction steps differ for various pH ranges, which are shown below:

HER in acidic electrolyte:

$H^+ + e^- \rightarrow H_{ads}$ (Volmer)

$H^+ + e^- + H_{ads} \rightarrow H_2$ (Heyrovsky) or $2\ H_{ads} \rightarrow H_2$ (Tafel)

HER in alkaline electrolyte:

$H_2O + e^- \rightarrow H_{ads} + OH^-$ (Volmer)

$H_2O + e^- + H_{ads} \rightarrow H_2 + OH^-$ (Heyrovsky) or $2\ H_{ads} \rightarrow H_2$ (Tafel)

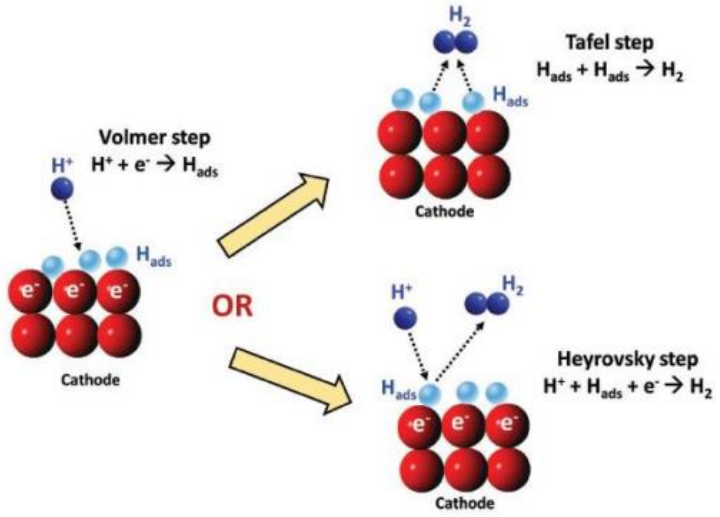

Figure 2. Schematic presentation of different pathways for HER [20]

The first step of HER mechanism is the Volmer step for both electrolyte mediums. The acidic solution depends on the reaction between hydrogen proton and electron by leading to adsorbed hydrogen. However, for the alkaline environment, the mechanism starts with the reaction between water molecule and electron by leading formation of hydroxide additionally to the adsorbed hydrogen **Figure 3**. Since there is extra H_2O adsorption and dissociation in the first step of alkaline HER, this leads to slower kinetics than acidic HER. Also, the ability for decomposing of water addition to the free energy change, is another feature for lower activity in alkaline HER than the acidic HER [7], [10].

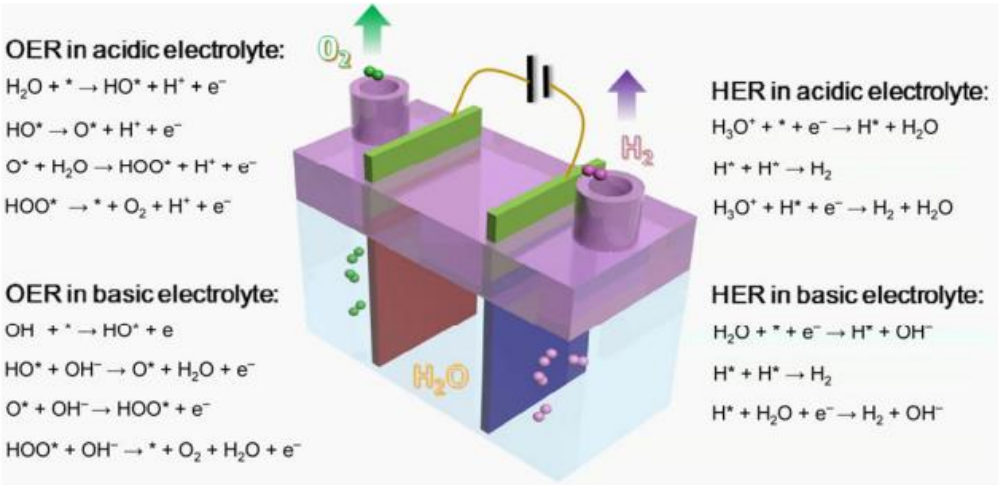

Figure 3. Possible pathways for both acidic and basic electrolytes in OER and HER [15]

1.4 Fundamentals of OER

The main reaction to obtain reversible processes with oxygen reduction reaction (ORR) and HER is the water oxidation or oxygen evolution reaction (OER), which takes place at the anode side of the electrochemical cell. Coupling procedures of proton and electron produce molecular oxygen [21] This evolution of one molecule of O_2 requires four-electron transfer which these steps of the mechanism are shown below:

1) $OH^- + * \rightarrow HO* + e^-$

2) $HO* + OH^- \rightarrow O* + H_2O + e^-$

3) $O*+ OH^- \rightarrow HOO* + e^-$

4) $HOO* + OH^- \rightarrow * + O_2 + H_2O + e^-$

where O*, OH*, and OOH* are the absorbed intermediates of the OER mechanism

Noble metal electrocatalysts such as Ir, Ru, and their oxides (IrO_2, RuO_2) show the best OER activity, especially for the acidic mediums. In the case of alkaline mediums, some of the 3d transition metals like Fe, Co, and Ni provide noticeable features in terms of OER activity and become an important group to examine detailly. With the investigation of different transition metal-based compounds, some of the reported ones, such as chalcogenides, phosphides, and borides, give better activity than oxides [15]. However, besides the efficient conduction of charges with the presence of a metallic core, surface oxides are helpful to the continuity of OER. Oxidation of catalyst generally provides OER, thereby producing intermediates creating an increasement in oxidation, leading to a higher scale range for current densities from $\mu A.cm^{-2}$ to $mA.cm^{-2}$. To avoid overestimation of the activity, 10 $mA.cm^{-2}$ metrics should be used. Utilizing the Hoffman apparatus in the cell during the reaction provides this value by measuring the system's volume and concentration of product gases. Evaluation of electrocatalysts' performance should be done without being affected by corrosion and capacitive currents by obtaining the exact current measurements from OER [15]. Taking advantage of the metallic core-shell from a metal boride structure provides both more surface-active sites and charge conduction pathways [16]. Since monometal borides have formated metal oxide and (oxy) hydroxide on the reaction interface like CoOOH on the CoB metal, they show high OER performance. However, donating electrons from boron elements is the primary reason for preventing complete cobalt oxidation in the structure [22]. Lastly, there are four electron transfer mechanisms in the OER for the producing oxygen molecule and taking the place

of one kinetically favorable process for each OER step by single-electron transfer. This causes an accumulation energy for each step, and more sluggish OER kinetics, leading to higher overpotentials and higher Tafel slopes [21].

1.5 MDBs in the Literature

With the latest research, the most promising non-noble metals have become transition metal/metalloid-based electrocatalysts. Due to their high performance, transition metal carbides, phosphides, chalcogenides, borides, and nitrides are investigated for the HER. When the OER is considered, transition metal oxides, hydroxides, and metalloids like N, P, S, Se, and B with transition metals come forward [15]. Transition metal borides (TMBs) are one of the essential groups of non-noble metals thanks to their superior unique properties for EWS applications than to other TM-based counterparts. Firstly, they have a reverse electron transfer feature due to their amorphous structure, thereby gaining electron-rich metal sites and increasing activity[16]. When the electronic structure of TMBs is modified to tailor the electrochemical properties, the kinetic barrier for the mechanisms decreases directly.

Nonetheless, there are missing points for explaining high activity for HER despite the fact that reaction pathway is still the same as usual for HER [11]. To clarify these missing, Gupte et al. presented a fact as electron transfer from boron to the d-band center of cobalt in Co-B compounds [16]. Boron has higher electronegativity, and thanks to this, the d-band orbitals of cobalt could be filled with more electrons. Consequently, due to the higher electron density of Co active sites, it enhances the donating ability of cobalt. Since boron doesn't behave as the direct active site itself, it satisfies the stability by donating electrons, increases the HER activity, and behaves as the sacrificial element to prevent oxidation of metal that contributes electrons. Promoting adsorption and desorption of H* and OH– intermediates provide from the electron transfer from 2p orbit of boron to 3d (or 4d) of TM [15]. The second unique property of TMBs is owing to the long-range disorder due to amorphous structure, chemical stability, and high concentration of unsaturated sites [23]. To achieve higher catalytic activity from TMBs, the structure could be tailored from amorphous to crystalline with the subsequent annealing [r]. Another reason for the enhancing OER performance is the formation of TM oxides, TM (oxy) hydroxides, borates, and boron oxides due to the surface oxidation [15].

The first investigation about the HER activity of diborides (NbB_2, ZrB_2, and TaB_2) and W_2B_5 has done by Kuznetsova et al. in 1974 in acidic electrolyte with 1 M H_2SO_4. [10], [11]. Amorphous Ni_2B for alkaline HER was investigated by Los and Lasia in 1992. [24]. After a slow time in terms of TMB investigation, commercially available MoB and Mo2C have been reported by Vrubel and Hu in 2012 to have high activity for HER in both acidic and alkaline environments [25].

There are 12 different transition metal diborides that can be classified into three groups: a) AlB_2, b) ReB_2, and c) RuB_2 type diborides (see **Figure 4**). AlB_2-type diborides as a first group have a P_6/mmm crystal structure, forming graphene-like layers of boron by covalent bonding. However, for the ReB_2, there are chair formations of boron atoms while introducing boat confirmations for RuB_2 [19]. These 2D borophene subunits in 3D metallic framework of TMBs have been investigated recently in more detail for electrocatalytic applications. They provide unique properties like low electrical resistivity, good chemical stability, hardness, and high thermal conductivity due to the layered structure that they have [26]. By comparing them with other types of electrocatalysts like metal disulfides, diborides have more abundant catalytic active sites and better conductivity in terms of electrical and thermal [19]. There is an open area to investigate the electrocatalytic activity of metal diborides due to the limited number of articles, especially for OER half-reaction, even though they have been studied highly due to their well-defined crystal structures in different applications. In the literature, the most important reasons for this lack of reports are the difficult synthesis conditions and inadequate experiences with the design principles.

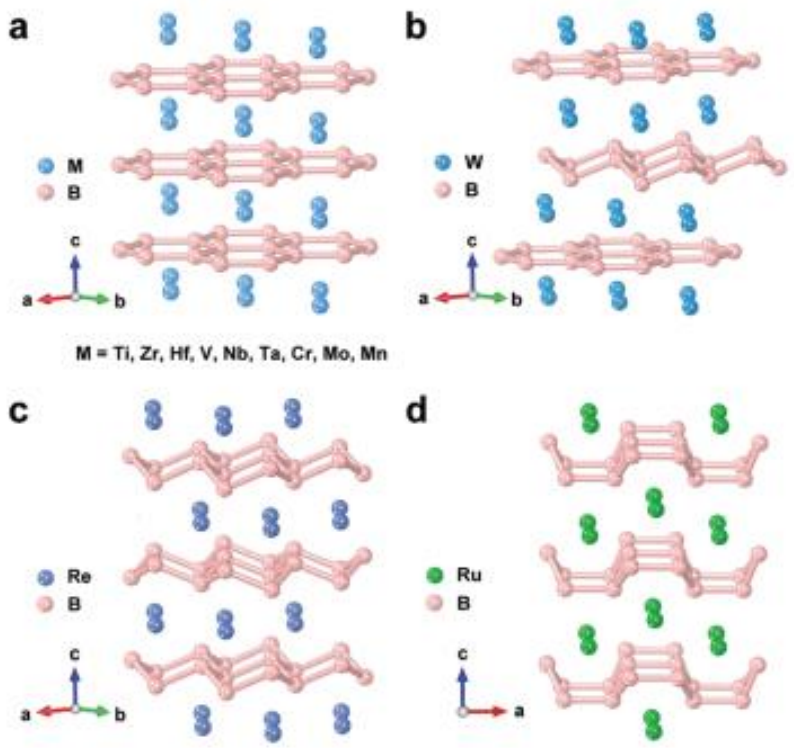

Figure 4. Twelve different metal diborides and their crystal structures: (a) MB_2 (M = Ti, Zr, Hf, V, Nb, Ta, Cr, Mo, and Mn), (b) WB_2, (c) ReB_2, and (d) RuB_2 whereas pink balls correspond to boron atoms, while the light blue, blue, bluish violet and green balls represent the referring metal atoms [27].

As mentioned before in the fundamentals of HER, ΔG Hads is a valuable feature for theoretically understanding the HER activity of electrocatalysts. This feature which is beneficial for evaluating the hydrogen adsorption capability of materials is caused by the intrinsic electronic structures of electrocatalysts [28]. To profoundly understand this feature, Li et al. studied the ΔG of atomic H bonding of 12 transition metal diborides for the most energetically favored plane of a metal surface (001) [19]. From these 12 metal diborides, the order was given in **Figure 5** according to three different groups: group VIII diborides (RuB_2 and OsB_2), group VII B diboride as ReB_2, group VI B diborides (TiB_2, HfB_2, and TiB_2). Since smaller ΔG (nearly zero) states better activity, RuB_2 has better

HER activity between 12 metal diborides from the linear correlation between Gibbs free energy and d-band center.

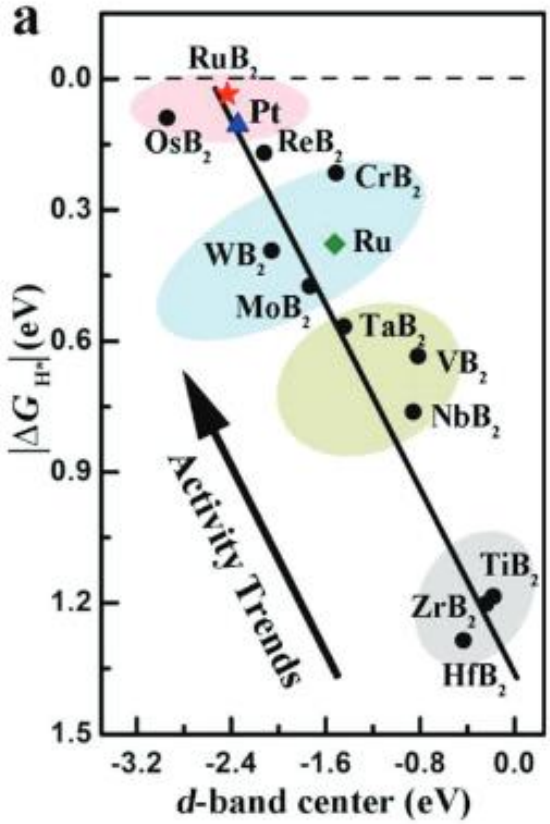

Figure 5. a) Linear correlation between d-band center of diborides in comparison to Pt and Ru versus absolute value of hydrogen adsorption free energy and d-band center of [19]

Another information obtained from the graph is that the comparison of RuB_2 and elemental ruthenium indicates the improving HER activity with boron addition due to the lowering d-band center and $\Delta G\ H_{ads}$. Additionally, by comparing the noble metal platinum and RuB_2, RuB_2 has a smaller absolute value of Gibbs free energy and a slightly lower d-band center, which causes an expectation to show a better HER-catalytic activity than Pt.

There would be a broadening bandwidth of the d-band of metallic Ru from 5.04 eV 2 to 7.18 eV in the RuB_2 compound due to the coupling interactions between metal d-orbitals and boron sp- orbitals. Center of RuB_2 shift through down from Fermi level with unchanged d-band filling thereby decreasement in the strength of hydrogen biding and leading to better activity [19]. To further understand and compare the inherent activity of various catalysts, the polarization curve versus current density could be normalized by

electrochemical active surface area (ECSA) or the surface area [7]. Again, 10 mA.cm^{-2} current density is decided as the figure of merit of EWS overpotential. From the HER overpotential for the RuB_2 and Pt/C catalysts, RuB_2 is closer to commercial Pt/C in acidic electrolytes, which are 18 mV and 17 mV, respectively **(Figure 6b)**. However, for the alkaline environments, RuB_2 catalysts need 28 mV while Pt/C requires 37 mV (**Figure 6c)** [10], [29] [19] Additional to these 12 metal diborides, cobalt, nickel, and iron-based mono/diborides have also been investigated due to their high OER performances besides the HER activities. The biggest reason for this is the formation of active species during the electrolysis mechanism, especially in alkaline environments, by having high corrosion resistance. Nevertheless, noble metal catalysts have still been a better option than the non-precious metal alloys for the acidic environments.

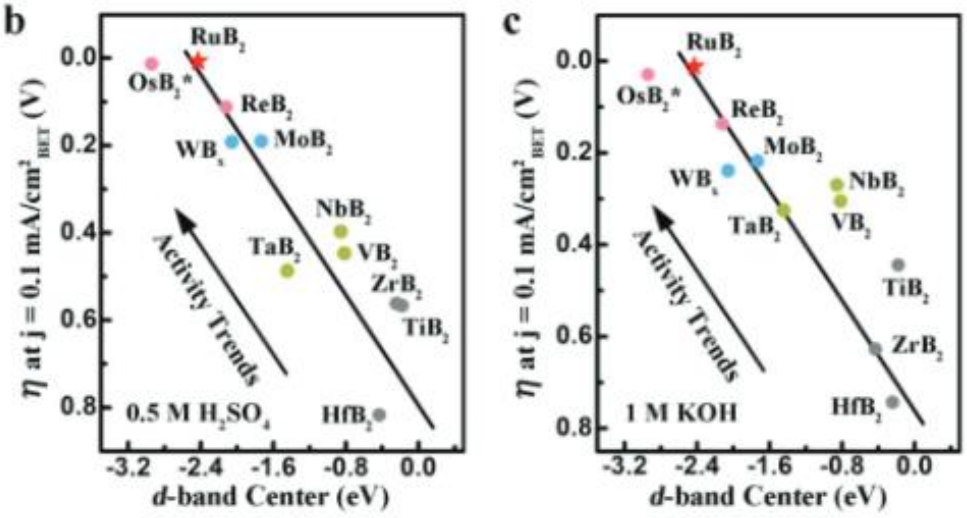

Figure 6. Linear plot of d-band center versus overpotentials at 0.1 mA.cm^{-2} current density b) in 0.5 M H_2SO_4 and c) in 1 M KOH [19]

WB_2, or so-called β-WB_2 (space group $P6_3/mmc$), encompasses graphene-like and puckered-type boron subunits [27]. The electrocatalytic activity of WB_2 was for the first time documented by Li et al. [19], a report in which a series of twelve MDbs were measured toward HER, and WB_2 was amongst those with decent catalytic performance with an overpotential of less than 300 mV to deliver 10 mA cm^{-2} (**Figure 7**). Followed by this report, similar studies appeared on the electrocatalytic HER performance of WB_2. Guo et al. [27] evaluated the HER activity of 12 monometallic MDbs, placing WB_2 within the white region—having desirable features and an overpotential of < 300 mV at 10 mA cm^{-2}. In addition, Park et al. [6]documented the HER performance of β-WB_2 with an overpotential of 271 mV to afford 10 mA cm^{-2}. Finally, Jin et al. [30] reported on the

electrochemical HER of an iron covalent-doped WB_2 catalyst (Fe-WB_2), revealing a very low overpotential of 68 mV to generate 10 mA cm^{-2}.

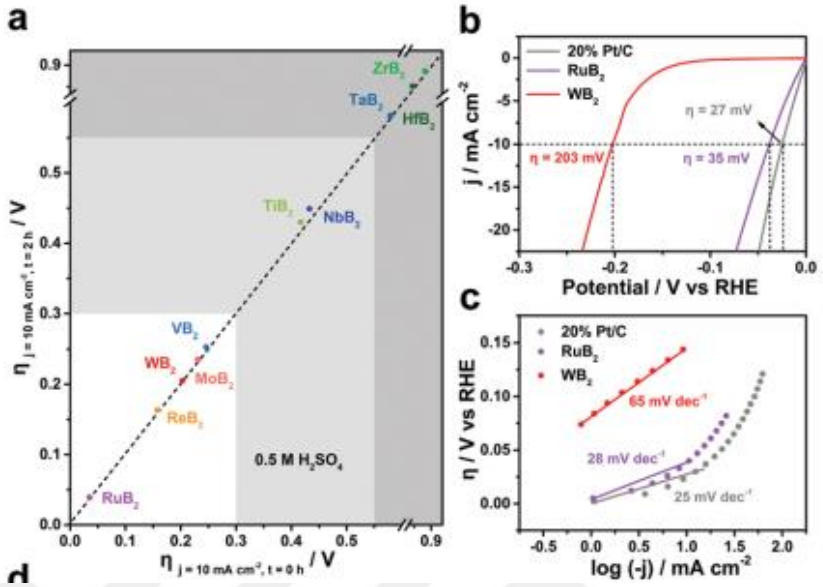

Figure 7. (a) The catalytic activity versus short-term stability of mentioned metal diborides for HER at time 0 h and 2 h by showing the ideal stable catalyst with the dashed line, (b) Polarization curves 20% Pt/C, RuB_2, and WB_2 for HER in 0.5 M H_2SO_4 medium, and (c) Tafel plots of 20% Pt/C, RuB_2, and WB_2 for HER [27]

The considerable difference between the recent work by Jin et al. [30] with those of previous studies in terms of HER activity originates from a heteroatom (Fe) incorporation into the structure of WB_2. According to the DFT calculations, Fe doping could effectively alter the surface charge redistribution of WB_2, which results in a diminution of the atomic hydrogen Gibbs free energy (ΔG_{H^*})—an indicator of HER performance—alleviating the HER kinetics barrier compared to blank WB_2. In this context, the electronic structure of a catalyst is indeed a game-changer that can directly impact ecteronic states, band structures, and adsorption capacity [31], [32].

1.6 Further Adjustments of MDBs and Their Features

Even though TMBs promise electrocatalysts for commercial EWS systems with pristine versions, there should be further adjustments to tailor their properties while providing better electrocatalytic performance. Phase engineering (like boron layer construction, crystallinity, etc.), morphological engineering (nanosizing, change in the particle shape, etc.), component regulation (doping of another element, changing the boron to metal ratio, etc.), surface oxidation, and hybridization (TMB/rGO, TMB/TMX,

etc.) are the main adjustments to improve the intrinsic activity, provide the more electrochemically active sites, and increase the stability of TMBs [15], [33].

Nano sizing

Nano sizing is vital to obtain a larger specific surface area (SSA) and electrochemically active surface area (EASA) due to a higher surface-to-volume ratio. However, during the synthesis, the agglomeration occurs between the nanoparticles and creates larger particle sizes. Especially for the conventional production techniques such as solid-state synthesis, the direct reaction of elements promoting grain growth due to high temperatures is inevitable since they process in elevated temperatures. For this reason, reducing this agglomeration and dispersing the particles should be considered to obtain the smallest achievable size and the highest SSA. Higher SSA leads to more space to satisfy the reaction between catalyst and electrolyte solution and improves the electrical contact. Two ways for these features are downsizing of material from micron to nanoscale and directly synthesizing nanostructures (like nanosheets, nano chains, and nanospheres) [23] are crucial strategies for the superior activity of electrocatalysts. Another important advantage of nanostructures is improving the penetration of electrolyte medium, thereby providing better diffusion in EWS systems [34]. During the downsizing, forming of structural disorders and defects in the structure creates more active sites to behave as a catalyst and leads to improving the electrocatalytic feature by changing the local electronic structure of the material. By investigating these different disorders in the structure, amorphous ones usually could maintain better activity for EWS systems due to the creating of lots of unsaturated regions on the catalytic surface, even a short-range in the amorphous structure is harmful to the electronic and photonic features [35].

Doping or alloying

A crucial adjustment for the TMBs electrocatalytic activity is the cationic doping to the structure by leading to more active sites, especially for the EASA. Doping provides higher conductivity and better intrinsic activity by tailoring the electronic structure and crystal structure of electrocatalysts. Also, Agglomeration generally decreases when a hetero metal is doped to the structure, creating more homogeneous morphology [15]. The non-metal and metal dual-doping as the anionic doping with the incorporation of Co and P together into the Fe-B resulted in a structure that provides better performance for both half-reactions due to the electronegativity differences between anions and boron[36]. The incorporation of metals like Fe, Ni, and W could increase the activity of metal-metalloid

catalysts thanks to the charge transfer between them [23]. To take advantage of each desired property from the materials separately, composite structures could be utilized by the best combination between them. Especially for the TMBs, hybrid structures with other promising catalysts satisfy the need of higher conductivity, electroactivity, better stability, and more active sites [15].

Degree of crystallinity

TMB nanomaterials with amorphous structure has important activity in the literature for both half-reactions [16], [28]. In the HER cases, a reduction of resistance at the electrocatalyst interface is occurred due to high electrical conductivity thereby charge transfer of all the electrocatalysts [37]. Higher electron density around the Fermi level assists higher conductivity since the Fermi energy level is the driving force of electron transport theoretically. By considering the effect of nanosizing in the number of active sites for exposure, annealing temperature is an important condition to optimize the crystallinity degree in consideration [4].

In the OER mechanism, if the annealing temperature increases, there would be a decreasement in the amorphous Co-Ni-B-O activity due to the higher degree of crystallinity [x]. However, like the other adjustments, there could be an optimum degree of crystallinity for tailoring the TMBs' activity [38], [39]. The important reason for this is facilitating the thermodynamic and kinetic barriers for the intermediates' formation (like OOH*) in OER with the lattice strain on metal atom due to the high annealing temperature, thereby the high degree of crystallinity. However, as a crucial consideration, catalytic activity sometimes decreases due to the formation of large grain and reduction in SSA with the elevated temperature synthesis conditions [15]. To investigate this effect, Li et al. studied with the catalytic activity of amorphous FeB2 with the annealing and dependence of crystallinity. According to this work, three different annealing temperatures and degrees of crystallinity were investigated (350 ˚C, 450 ˚C, and 600 ˚C). As a result, they obtained the best activity with the partially crystallinity sample (350 ˚C) compared to amorphous and higher degree of crystallinity [33].

Metal to boron stoichiometric ratio

Another adjustment is the stoichiometric ratio between metal to boron. In most cases, there is a positive trend of improving catalytic activity with the increasing boron content. According to DFT calculations, boron-rich metals tailor appropriate binding energy for adsorption and desorption of HER intermediates in the light of Sabatier's principle by

leading to an increase in activity by assisting electron transfer. When the same morphology and SSA are kept, FeB_2 provided better activity than Fe_2B for both HER and OER as a boron-rich compound [33]. As another example, for Mo-B electrocatalysts, an increasing in HER performance with the increasing boron content, especially for the acidic medium, is again a valid trend in the order of Mo_2B, MoB, and MoB_2 [40]. Also, the morphology of metal compounds could change with the boron ratio, like the average particle size. According to the Zhang et al. study, there is a reduction in the average particle size of NiB_x electrocatalysts when the boron content increases. They reported that this amount was from 2.27 to 0.55 μm and the trend of electrocatalytic performance showed an order for decreasement $NiB_{0.54}$, $NiB_{0.48}$, $NiB_{0.36}$, and $NiB_{0.27}$ [41]. DFT calculations have investigated the reason for the higher activity in metal-rich borides is the raising the electron amount in the d-orbitals of metal. Also, the introduction of boron vacancies could lead to increasing the Fermi level's electron density and improving activity for electrocatalysts [40]. From these examples, the overall features of the TMBs catalysts could be affected by different aspects of their optimum metal to boron ratio of them.

Supporting materials

When the electrocatalysts work with low electrical conductivity, there could be an additional overpotential due to the voltage drop through the electrode. If a highly conductive substrate (higher electron density near Fermi level) is utilized and loaded with electrocatalysts to its porous structure, it leads to facilitating the charge transfer, providing better activity, and avoiding the undesired resistance at the catalysts interface. Due to usage of porous support materials without any binder to loading, the problem caused by binder's corrosion resistance is blocked [19]. Three important types of support materials are carbon-based ones, nickel foams, and copper foams [34]. The porous structure of supports provides the dispersion of catalyst particles and leads to higher in the active sites and SSA. Ni foam, as favored support for metal diborides, is active for both half-reactions compared to other current collectors. So, the separation of electrocatalysts' activity individually is an important problem. Performing measurements with inert support solve this problem as a fair comparison [15].

Surface oxidation

Surface oxidation is an inevitable process when TMB comes across water or air. OER performance could be improved by taking advantage of metallic core and shell structure

adjustments. One of the reasons of high OER performance from the TMB electrocatalysts is due to the unavoidable formation of boron-oxo and TM-oxides or (oxy) hydroxides on the surface. Also, an oxide-rich surface layer could be occurred during the EWS process in situ besides structural engineering. According to Li et al. the transformation of $Ni(OH)_2$ into catalytically active NiOOH on the boronized nickel plate during the OER process before stabilization. Formation of borates leads to optimization of electronic structure and improvement of the electron density near metal atoms in the OER process. So, even the pathway is the same, the reaction rate is accelerated. Mostly, surface oxidation provides better OER activity, but reduces HER activity. The studies are generally based on either the negative effects of the oxide layer on TMBs in terms of HER, or by proving the alkaline electrolytes TM- hydroxides also can facilitate HER activity [15].

1.7 The Challenges of MDBs in EWS

With the current literature review, designing and synthesizing the best electrocatalysts depend on lots of features and parameters which should be tailored according to the optimum conditions. In summary, the desired properties are to obtain higher active sites, better stability in various mediums, and utilize as bifunctional electrocatalysts for HER and OER by benefiting from crystal structure dependence, doping/ changing the doping ratio, loading on the support, etc. [15].

The important thing is here to find a balance between experimental studies and commercial applications. For example, when the amount of electrocatalysts on the electrode surface increases from 1 mg/cm^2 to 10mg/cm^2, the number of active sites sometimes increases, also by leading to a lower overpotential requirement (e.g., <200 mV) for that application [17]. However, loading catalysts with a high amount shouldn't be applied in commercial applications due to additional costs. Since upscaled electrolyzers use mostly 0.25 mg/cm^2 of electrocatalyst loading, experimental studies should be done under similar loadings like 0.1-0.5 mg/cm^2 generally [1].

Another important limitation is tailoring the surface oxidation for the OER performance. Besides the fact that a thin layer of oxide/hydroxide layer as a core of electrocatalyst provides better OER activity, it also could decrease the conductivity and reduces the active sites for HER [42].

Last but not least, the stability feature of electrocatalysts, especially HER, is the most crucial one during the commercialization progress due to the bubble evolution while EWS. The prominent consideration for an ideal catalyst in terms of stability is maintaining the high catalytic activity for long times in both acidic and alkaline EWS systems. The lacking point of TMBs is the low resistance to acidic environments. Currently, the popular commercial investigation is the adding Nafion (perfluorinated alkyl sulfonate iomer solution) as a binder to stick the electrocatalyst to the electrode surface. Thanks to the unique structure of Nafion, stability, electron, and hydrogen transfer could be assisted for both OER and HER in acidic electrolytes [37].

Chapter 2: **Synthesis and Characterization of Tungsten Diborides**

2.1 Synthesis of Electrocatalysts

Tungsten powder (W, 99.9% metal basis) and boron oxide powder (B_2O_3, 99% metal basis) were purchased from Alfa Aeasar. Nickel (Ni, 99.99% trace metals basis), cobalt (Co, 99.99% trace metals basis), activated charcoal powder (C, pure), sodium chloride (NaCl, 99 %), and potassium chloride (KCl, 99 %) were purchased from Sigma Aldrich. Amorphous nano boron powder (B, 98.5%) was purchased from Pavtec.

2.1.1 Molten Salt-Assisted Synthesis

Tungsten diboride electrocatalysts were synthesized using the molten-salt technique in the presence of binary NaCl–KCl eutectic molten salts with a molar ratio equal to unity ($T_m \approx 657$ °C) [43]. In a typical synthesis procedure and based on the molten-salt reduction reaction given in Equation. (3), stoichiometric quantities of W and B were used as reactants.

$$W_{(s)} + 2\ B_{(s)} \rightarrow WB_{2(s)} \quad (3)$$

Concerning the substituted samples, a similar reaction (Equation. (4)) was followed for the substitution of W with elemental Ni and Co at various atomic percentages (x = 0.1, 0.2, and 0.3).

$$(1\text{-}x)\ W_{(s)} + x\ TM + 2\ B_{(s)} \rightarrow W_{1\text{-}x}TM_xB_{2\ (s)} \quad (4)$$

The reactants and salts with a weight ratio of 1:3 was weighed and transferred into a hardened stainless-steel vial under a protective Ar environment inside a glovebox (MBraun Labmaster Pro DP, O_2 and H_2O level below 0.1 ppm). Prior to the thermal treatment, the powder mixture was milled by a high-energy ball milling (Spex^{TM} 8000D Mixer/Mill) for 90 min at 1400 rpm for the mechanical activation of the precursors and to obtain a completely homogeneous mixture. The milling process was carried out with six steel balls, two of which were 1/2" in diameter and four of which were 1/4" in diameter. The resulting powder from milling was first transferred into an alumina crucible and then placed in a quartz glass tube to undergo heat treatment in a vertical sealed furnace at 1373 K for 180 min with a 10 K/min heating rate under constant Ar flow. The sample batch was naturally cooled down to room temperature. The resultant was collected and treated with deionized (DI) water at 373 K to remove salts. The product was then rinsed

several times with DI water and absolute ethanol. Finally, the vacuum drying was performed at 353 K for 120 min to eliminate any residual water and ethanol. It should be noted that to avoid confusion, materials that were synthesized by the molten-salt technique were labeled as $W_{(1-x)}TM_{(x)}B_2$/ms.

2.1.2 Carbothermal Reduction Synthesis

For the carbothermal reduction, the previous work of our group was taken as a reference [32]. WO_3, B_2O_3, and activated carbon powder were used as the main ingredients to manufacture the virgin WB_2. Identical to previous section, the substitution reactions proceeded with various atomic percentages of Ni and Co (x = 0, 0.1, 0.2, and 0.3). For both purposes, the following reaction was used:

$$(1\text{-}x)\ WO_{3\,(s)} + x\ TM_{\,(s)} + B_2O_{3\,(s)} + (6\text{-}3x)\ C_{\,(s)} \rightarrow W_{1-x}TM_xB_{2\,(s)} + (6\text{-}3x)\ CO_{\,(g)} \quad (5)$$

All the preparation, weighing, and transferring of reagents into stainless steel were performed in an Ar-filled glovebox like the previous synthesis techniques. The powder precursor was mechanically activated for 180 min at 1200 rpm. The resultant was transferred into a graphite crucible and heat-treated at 1723 K for 360 min. All the samples were collected in powder form and stored in an argon atmosphere. It is worth noting that catalysts manufactured by the carbothermal reduction method were marked as $W_{(1-x)}TM_{(x)}B_2$/ct.

2.2 Characterization of Electrocatalysts

2.2.1 Chemical Characterization

X-Ray Powder Diffraction (XRD)

Figure 8 shows the XRD patterns of layered $W_{(1-x)}TM_{(x)}B_2$ by comparing two synthesis methods at different substitution ratios along with the schematic crystal structure of pristine AlB_2 and WB_2. For the unsubstituted WB_2/ms, a trace amount of WB was identified at 42.3^{o,} meaning that the formation of WB which has low formation energy couldn't be avoided under these synthesis conditions [44]. By looking at the substituted $W_{(1-x)}TM_{(x)}B_2$/ms, secondary phases were detected as cobalt boride and nickel boride (CoB, NiB, and WB_4, respectively). Among the XRD patterns of $W_{(1-x)}TM_{(x)}B_2$/ms catalysts, as the substitutional *TM* ratio goes up, a higher amount of boron-containing

secondary phases were encountered, and also the intensities of these peaks would become more distinguishable. (see **Figure 9**). Between the $W_{(1-x)}TM_{(x)}B_2$/ms samples, $W_{0.7}Co_{0.3}B_2$/ms has the most impurity phases in its structure. By examining the $W_{(1-x)}Co_{(x)}B_2$/ms (at x = 0.1 and 0.2) and $W_{0.9}Ni_{0.1}B_2$/ms, a little amount of WB was visible which can be due to the formation of CoB and NiB impurities, which results in B deficiency. Unfortunately, there were unidentified and relatively high-intensity peaks at 49° and 51° in $W_{0.7}Co_{0.3}B_2$/ms and 47° in $W_{0.8}Ni_{0.2}B_2$/ms.

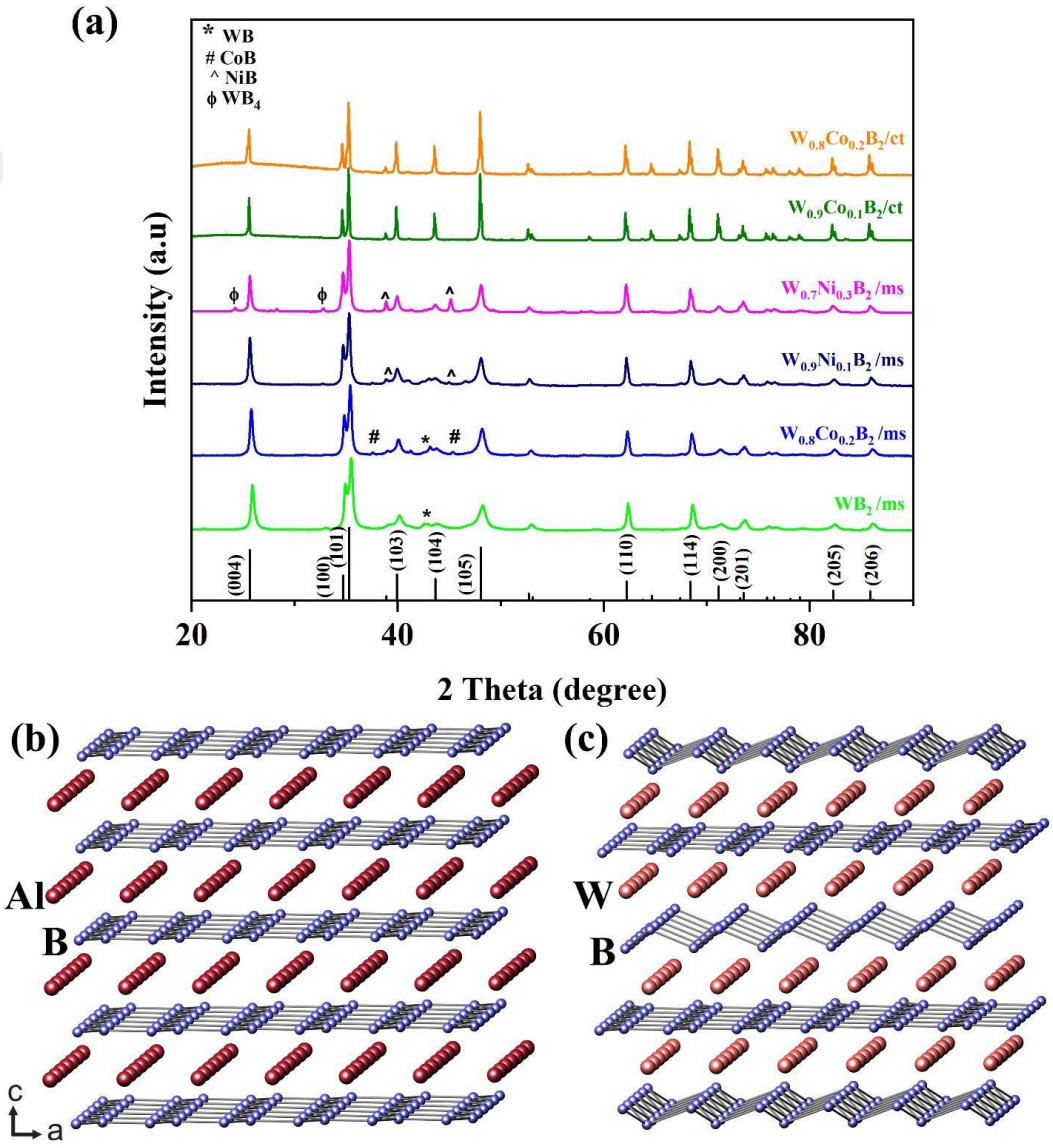

Figure 8. a) XRD patterns of parent and metal-substituted WB_2 synthesized by molten-salt (ms) and carbothermal (ct) methods, b) crystal structure of AlB_2 type with flat boron layers, and c) WB_2-type with both flat and puckered boron layers separated by the layers of metal atoms.

For carbothermal reduction, well crystalline phases of $W_{(1-x)}TM_{(x)}B_2$/ct were successfully obtained with almost 100 % purity (**Figure 8a and Figure 9**). The catalysts synthesized by molten salt differ from carbothermal reduction ones in terms of peak intensity and broadening, implying that the XRD peaks of $W_{(1-x)}TM_{(x)}B_2$/ms catalysts are broader in contrast to those of $W_{(1-x)}TM_{(x)}B_2$/ct. As a result, $W_{(1-x)}TM_{(x)}B_2$/ms samples are more nano-sized compared to the $W_{(1-x)}TM_{(x)}B_2$/ct ones [45].

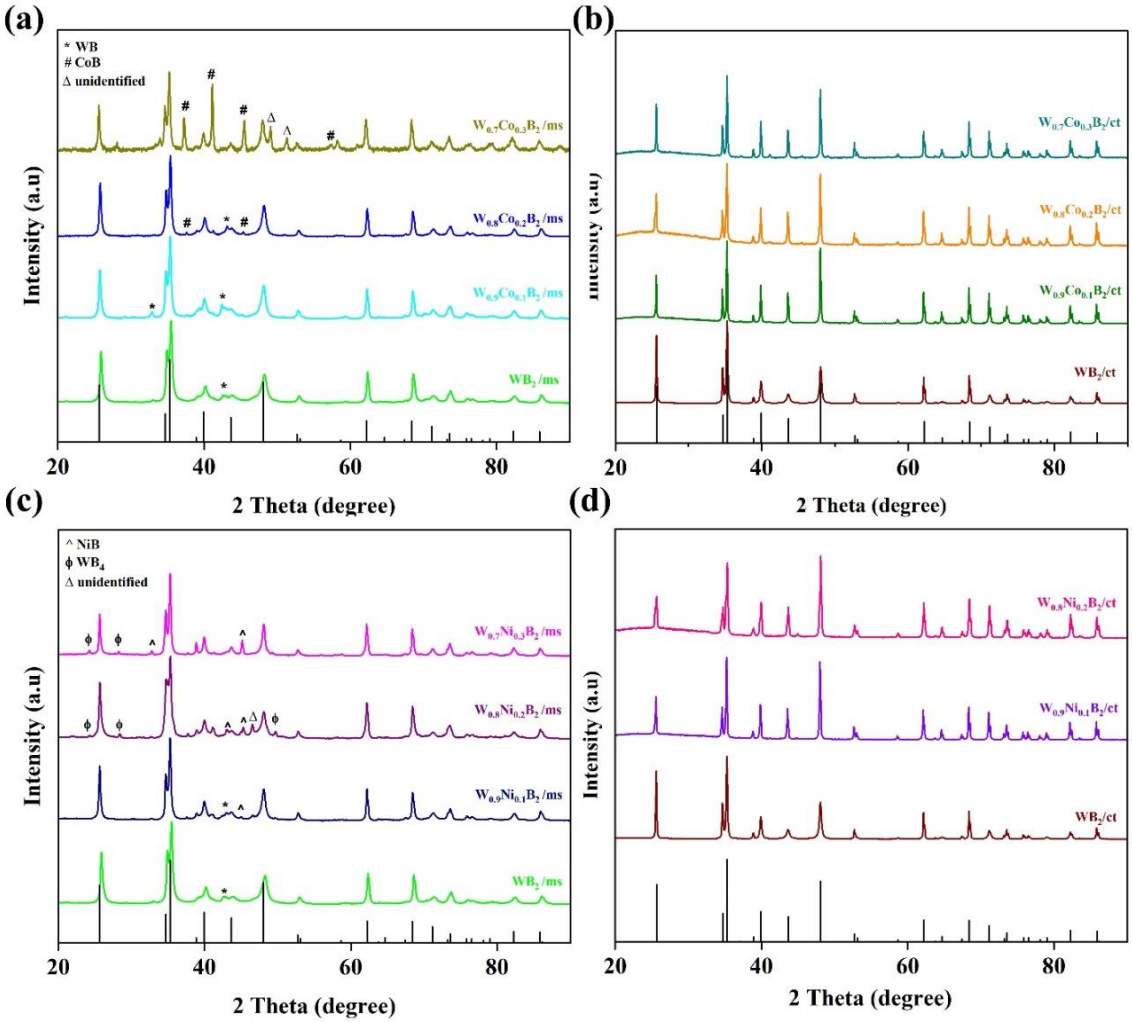

Figure 9. XRD patterns of a) $W_{1-x}Co_xB_2$ synthesized by molten salt (ms), b) $W_{1-x}Co_xB_2$ synthesized by carbothermal reduction (ct), c) $W_{1-x}Ni_xB_2$/ms, and d) $W_{1-x}Ni_xB_2$/ct.

Scanning Electron Microscopy (SEM)

As shown in **Figure 10**, SEM images of six different samples were compared to observe microstructural changes in morphology and size of particles by altering the synthesis method and substituting TMs. The particle sizes of $W_{(1-x)}TM_{(x)}B_2$/ms samples are in the range of 400-600 nm or smaller and have sponge-like morphology at the surfaces.

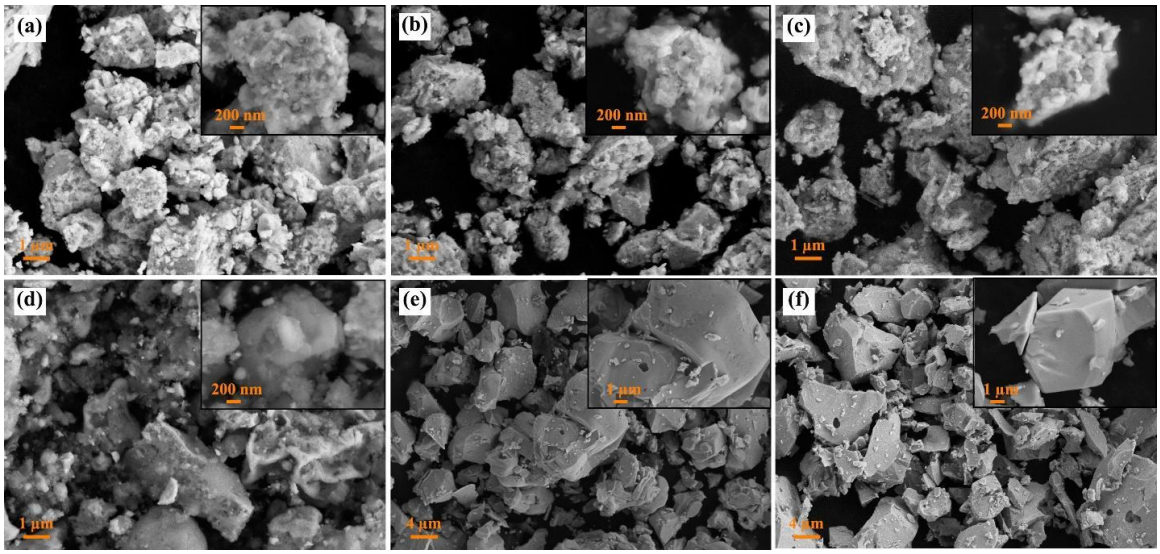

Figure 10. SEM images of a) WB_2/ms, b) $W_{0.8}Co_{0.2}B_2$/ms, c) $W_{0.9}Ni_{0.1}B_2$/ms, d) $W_{0.7}Ni_{0.3}B_2$/ms, e) $W_{0.9}Co_{0.1}B_2$/ct, and f) $W_{0.8}Co_{0.2}B_2$/ct.

Observations from **Figure 10 and Figure 11** indicate that the particle size and shape aren't affected significantly by the substitution amount of *TM*. It should be noted this indicates homogeneity in terms of particle size and shape for both Co and Ni substitutions content in the molten-salt technique.

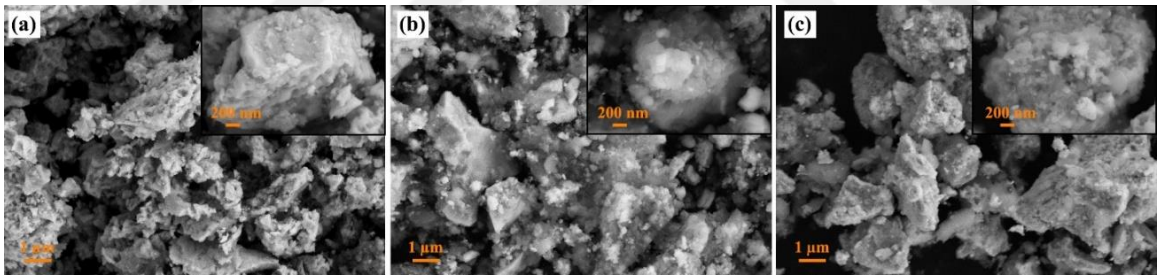

Figure 11. SEM images of a) $W_{0.9}Co_{0.1}B_2$/ms, b) $W_{0.7}Co_{0.3}B_2$/ms, and $W_{0.8}Ni_{0.2}B_2$/ms.

However, the morphology and sizes of powders synthesized by carbothermal reduction differ as shown in **Figure 10,** and **Figure 12.** Pristine WB_2/ct has a nearly spherical shape and a particle size of roughly 400 nm regarding non-aggregated ones, while $W_{0.9}Co_{0.1}B_2$/ct and $W_{0.8}Co_{0.2}B_2$/ct have particles with fused-layer-like and/or polyhedral structures and a size of about 1-10 micrometer. As presented in **Figure 10 and Figure 12**, inhomogeneity in particle size and shape has been observed as the substitution concentration increases for the Ni- and Co-substituted WB_2/ct samples. From **Figure 12**, virgin WB_2/ct is the most homogenous one among the $W_{(1-x)}TM_{(x)}B_2$/ct catalysts in terms of particle size and shape. To compare the extent of distribution of elements within the

as-obtained materials, EDS elemental mappings were employed at both low and high magnifications (**Figure 13**). The results confirmed the uniform distribution of W and B for both unsubstituted WB_2/ct and $W_{0.8}Co_{0.2}B_2$/ct samples. Moreover, EDS elemental mapping revealed oxygen as proof of surface oxidation, which XRD cannot detect.

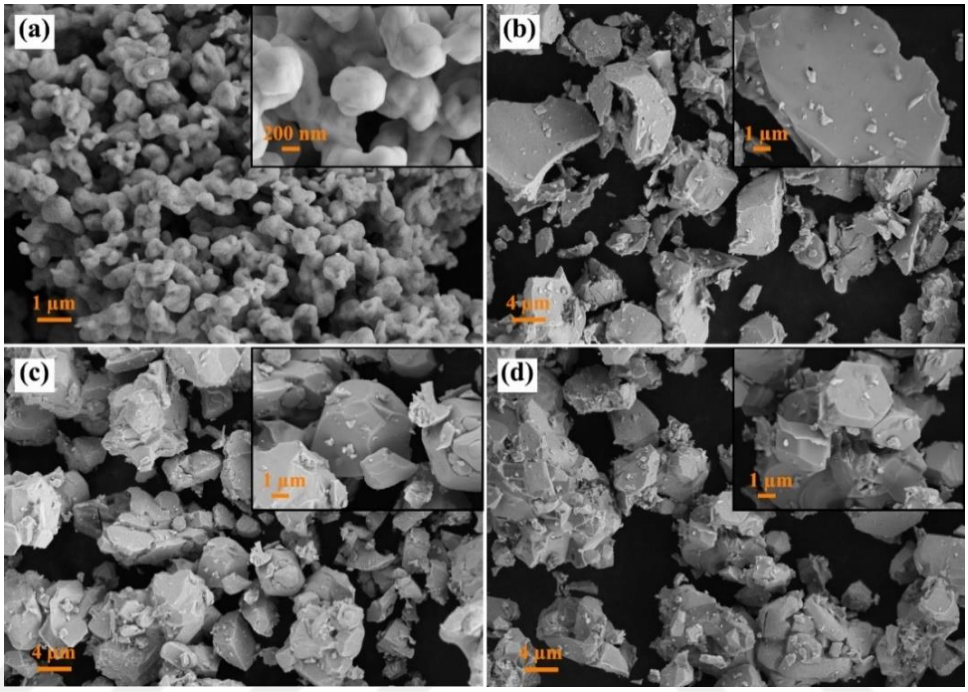

Figure 12. SEM images of a) WB_2/ct, b) $W_{0.7}Co_{0.3}B_2$/ct, c) $W_{0.9}Ni_{0.1}B_2$/ct, and d) $W_{0.8}Ni_{0.2}B_2$/ct.

The microstructures and related EDS elemental mappings of WB_2/ms and $W_{0.8}Co_{0.2}B_2$/ms at both high and low magnifications (**Figure 15**) are presented in **Figure 14**. The uniform distribution of each element in the powders as well as their grains can be seen.

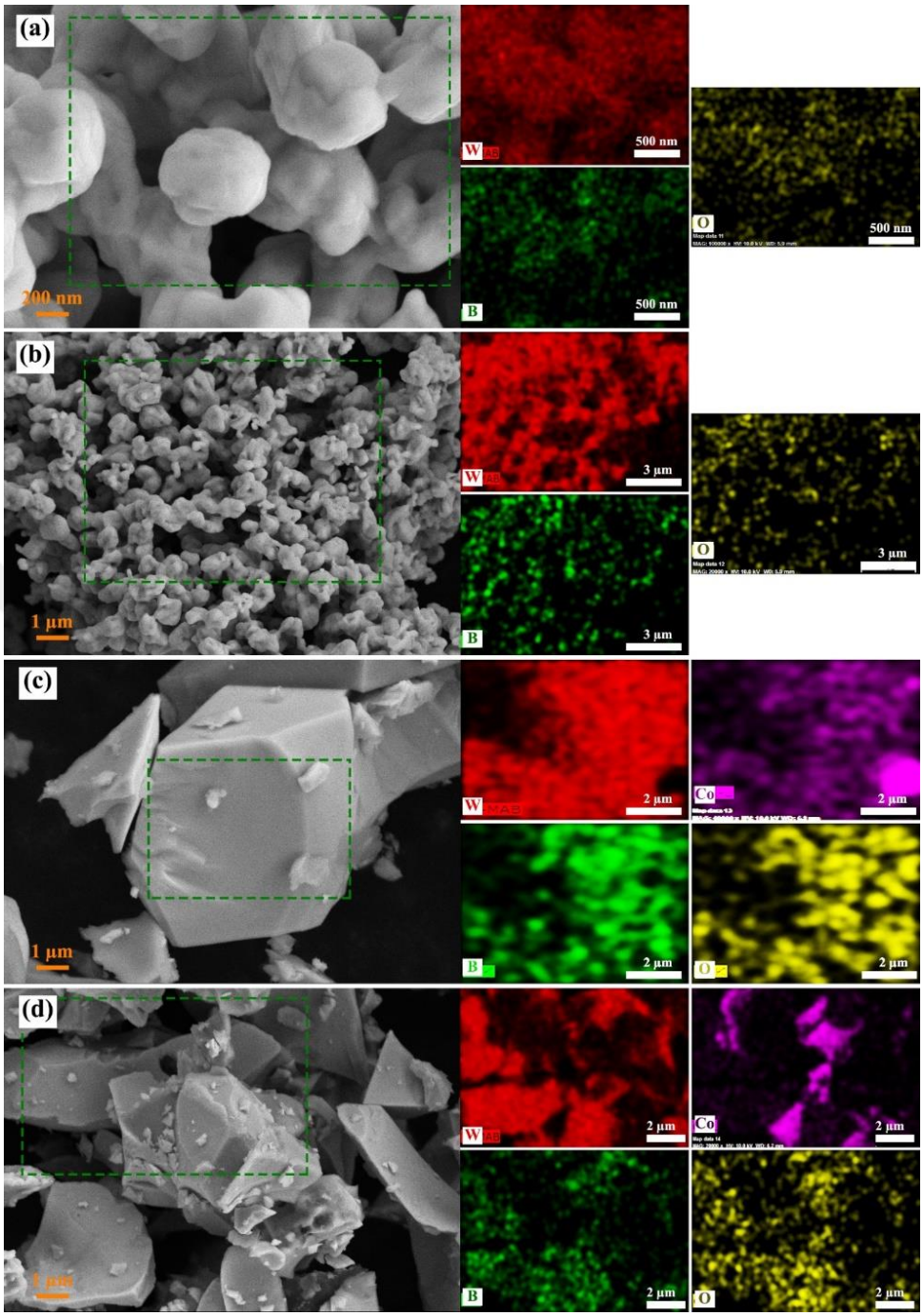

Figure 13. High magnification SEM images of a) WB_2/ct, and c) $W_{0.8}Co_{0.2}B_2$/ct, and low magnification SEM images of b) WB_2/ct, and d) $W_{0.8}Co_{0.2}B_2$/ct with related EDS mapping next to.

Unlike $W_{0.8}Co_{0.2}B_2$/ct, the Co element was nicely distributed all over the surface of the $W_{0.8}Co_{0.2}B_2$/ms catalyst without localizing a particular place. Additionally, some oxygen contamination was observed due to surface oxidation similar to EDS mappings discussed above (**Figure 13**).

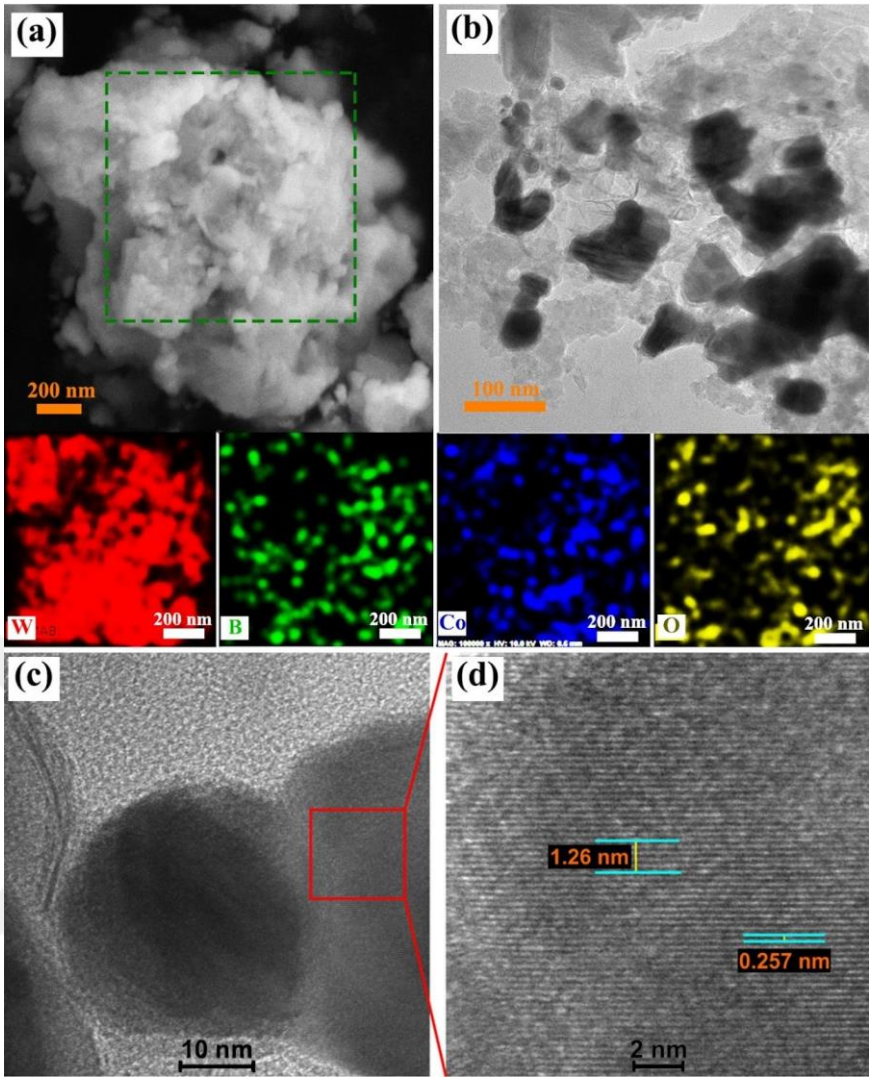

Figure 14. Characterization of $W_{0.8}Co_{0.2}B_2$/ms: a) High magnification SEM image of $W_{0.8}Co_{0.2}B_2$/ms with related EDS elemental mapping below b) TEM image of $W_{0.8}Co_{0.2}B_2$/ms, c) and d) HRTEM images of $W_{0.8}Co_{0.2}B_2$/ms

The high-resolution morphology and crystalline structure of $W_{0.8}Co_{0.2}B_2$/ms were further examined by HR-TEM (**Figure 14**), from which nanosized sub-grains below 20 nm can be manifested. The lattice fringes of $W_{0.8}Co_{0.2}B_2$/ms with 0.257 nm lattice spacing can be visualized in **Figure 14** which corresponds to the (100) or (101) planes of hexagonal structure crystallizing in the space group $P6_3/mmc$ [46].

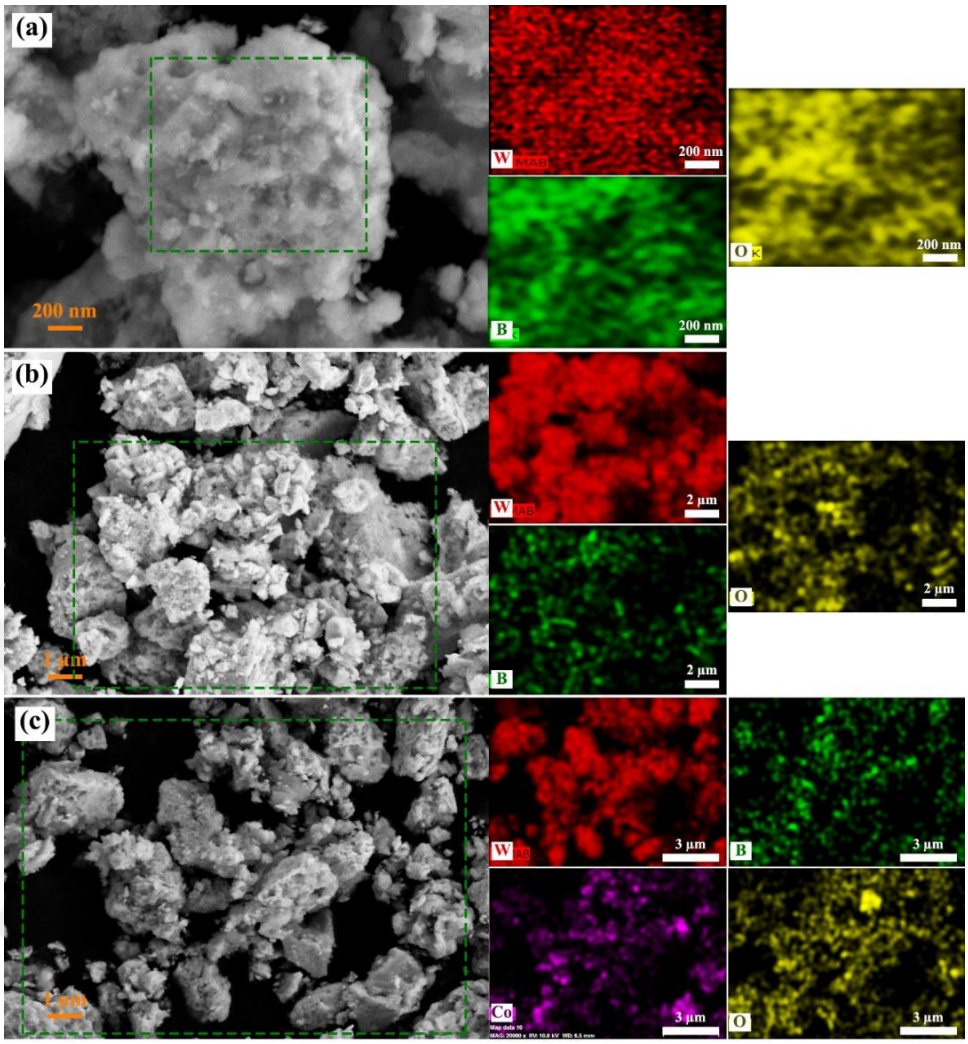

Figure 15. a) and b) High and low magnification SEM images of WB_2/ms, and c) Low magnification SEM images of $W_{0.8}Co_{0.2}B_2$/ms with related EDS mapping next to.

X-ray Photoelectron Spectroscopy (XPS)

To evaluate the electronic states and the surface chemical composition of as-prepared catalysts, XPS analysis was implemented. The relevant high-resolution deconvoluted XPS spectrum of W 4f, B 1s, Co 2p, and O 1s are depicted in **Figure 16** and **Figure 17**. From the XPS spectrum of $W_{0.8}Co_{0.2}B_2$/ms shown in **Figure 16**, the W 4f spectrum can be deconvoluted into two doublets located at 31.28, 33.48, 35.38 and 37.58 eV, which were assigned to W $4f_{7/2}$, W $4f_{5/2}$, W $4f_{7/2}$, and W $4f_{5/2}$, separately. Confirmed by the literature [47], [48], these two doublets indicate two different oxidation states of W^{2+} and W^{6+} which may correspond to the W-B bond of WB_2 and W-O bond of WO_3 respectively. Meanwhile, the B 1s spectrum (**Figure 16**) reveals that there are three species of boron on the surface that are assigned to B in WB_2 (187.58 eV), boron suboxide

(190.28 eV), and B^{3+} (192.08 eV). It should be highlighted that the B^{3+} peak at higher binding energy is correlated with B–O binding on the surface, which originates from metaborate (BO_2^-) species due to oxidation of boron on the surface [49]. The same study also stated that metaborate species on the surface can facilitate the reaction kinetics on the surface by adsorbing OH^- species. Likewise, **Figure 16c** manifests Co 2p spectra for the $W_{0.8}Co_{0.2}B_2$/ms sample. Based on the results, three doublets can be deconvoluted from the Co 2p spectrum that the first doublet positioned at 777.88 eV (Co $2p_{3/2}$) and 792.68 eV (Co $2p_{1/2}$) are related to Co-B binding, while the second doublet positioned at 781.48 eV (Co $2p_{3/2}$) and 797.18 eV (Co $2p_{1/2}$) are referred to Co^{2+} oxidation state, indicating the $CoO/Co(OH)_2$ [50]. Eventually, the third doublet at 786.78 eV and 802.48 eV are ascribed to the satellite peaks.

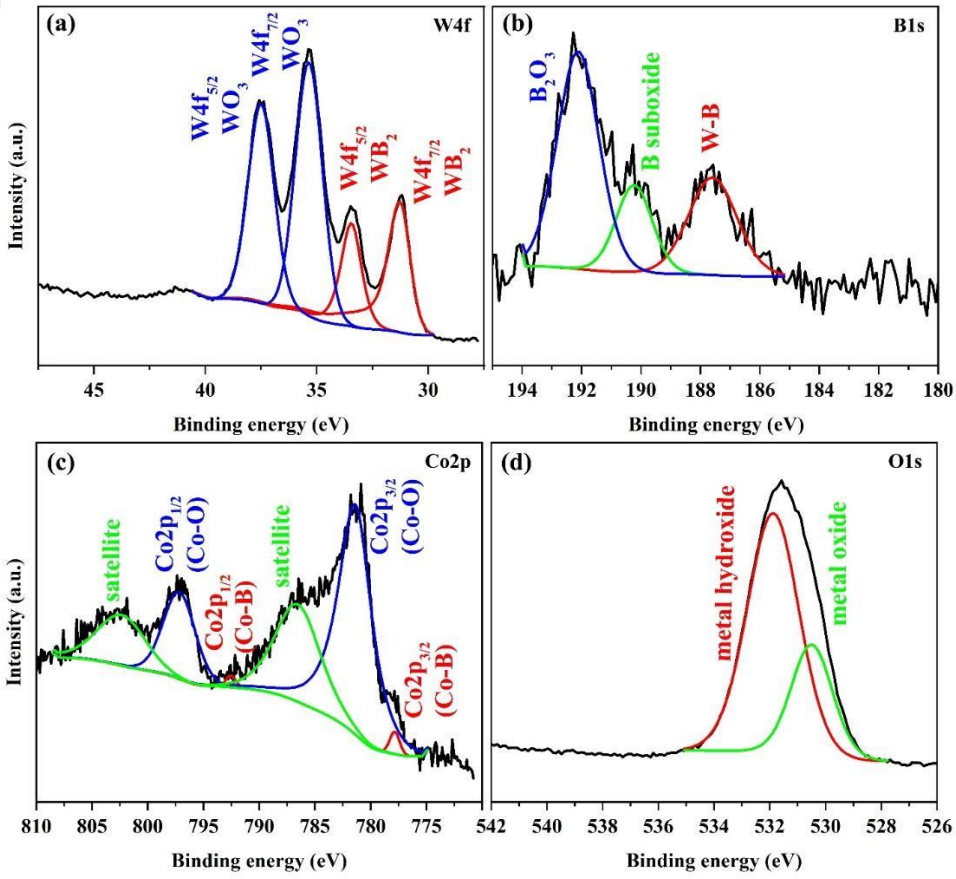

Figure 16. High-resolution XPS spectra of a) W 4f, b) B 1s, c) Co 2p, and d) O 1s for $W_{0.8}Co_{0.2}B_2$/ms.

To gain deeper insight into the oxidation states of the catalyst surface, the O 1s spectrum was also analyzed. As shown in **Figure 16d**, it is obvious that the O 1s spectrum can be deconvoluted into two O species centered at 530.48 and 531.88 eV, with which

the first one is ascribed to metal-oxygen bonds and the last is referred to adsorbed water or hydroxyl groups on the surface [51]. It should be noted that the trend discussed above is nearly the same concerning the Co substitution for x = 0.1 and 0.3 (see **Figure 17**).

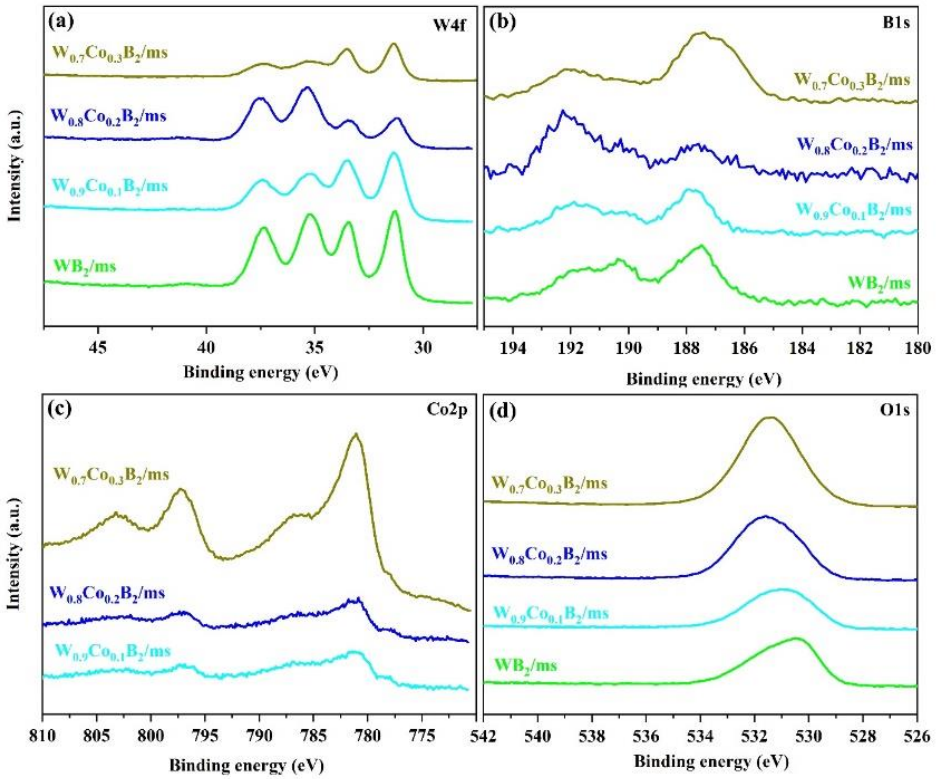

Figure 17. High-resolution XPS spectrum of a) W 4f, b) B 1s, c) Co 2p, and d) O 1s for parent and Co substituted WB_2 synthesized by the molten salt method.

Besides, **Figure 18** and **Figure 19** also reveal the XPS spectra of W 4f, B 1s, Ni 2p, and O 1s for the Ni-substituted catalysts. Based upon the findings, it is obvious that W 4f, B 1s, and O 1s exhibited the same trend as observed for Co-substituted samples.

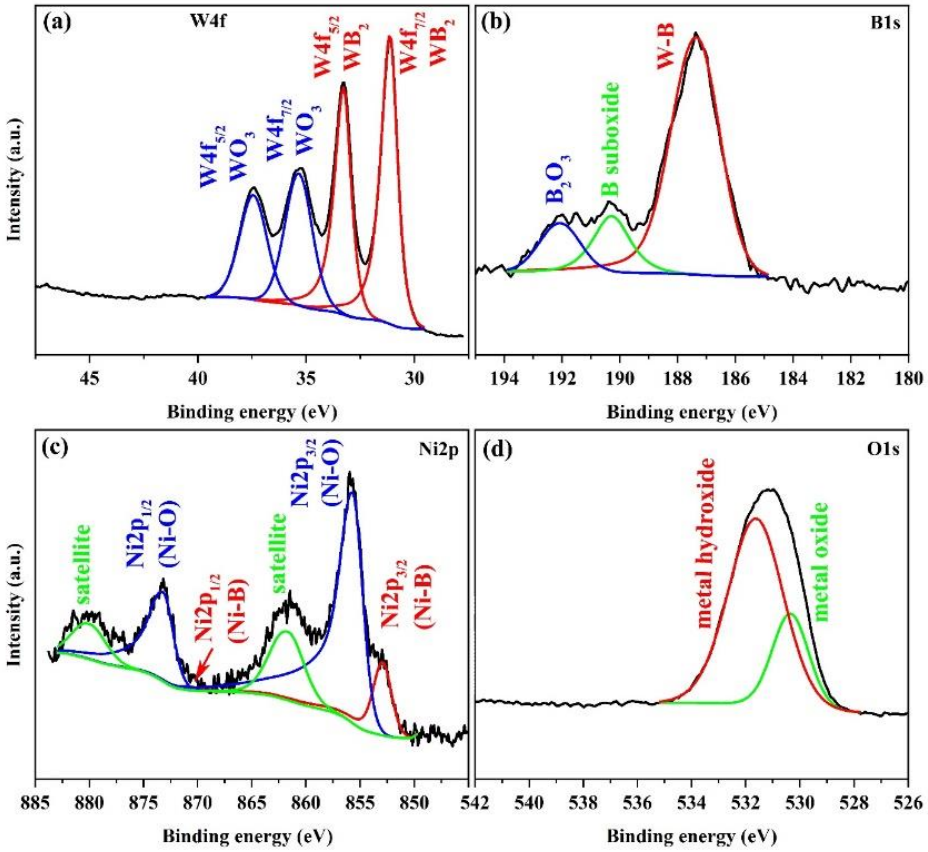

Figure 18. High-resolution XPS spectrum of a) W 4f, b) B 1s, c) Ni 2p, and d) O 1s for $W_{0.8}Ni_{0.2}B_2$/ms.

From **Figure 19c,** the Ni 2p core-level spectrum consists of three doublets including 852.98 eV (Ni $2p_{3/2}$) and 870.78 eV (Ni $2p_{1/2}$) related to Ni-B binding, 855.78 eV (Ni $2p_{3/2}$) and 873.28 eV (Ni $2p_{1/2}$) are referred to Ni^{2+}— indicating the existence of $NiO/Ni(OH)_2$ on the surface, and finally, 861.88 eV and 880.28 eV correlated with satellite peaks [32].

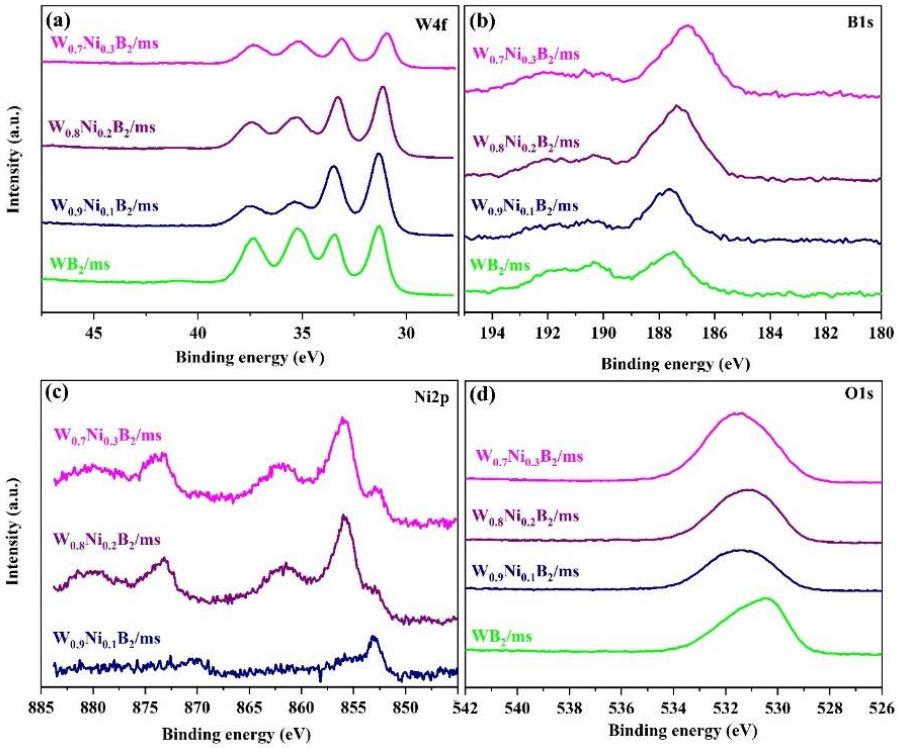

Figure 19. High-resolution XPS spectrum of a) W 4f, b) B 1s, c) Ni 2p, and d) O 1s for parent and Ni substituted WB_2 synthesized by the molten salt method.

2.2.2 Electrochemical Characterization of Electrocatalysts

To evaluate the electrochemical behavior of as-synthesized electrocatalysts, the linear sweep voltammetry (LSV) measurements were performed using a three-electrode configuration on an Autolab Potentiostat Galvanostat in which a standard reversible hydrogen electrode (RHE; HydroFlex) and Platinum spring were used as a reference and counter electrode, respectively, under 1 M KOH medium. The LSV curves were recorded at 5 mV s^{-1} sweep rate and 1.0 − 1.8 V and 0 − 1 V potential windows for OER and HER, respectively. Then, 10 mA cm^{-2} of current density was chosen as the critical point to determine the overpotential, thereby catalytic activity. The glassy carbon (GC) electrode was the working electrode with a diameter of 3 mm. For each measurement, a polishing step was applied to the GC electrode with an alumina slurry (0.5 µm) before each run. Finally, it was treated with first DI water and then ethanol for 15 min to clean the remaining alumina slurry. The catalyst ink was prepared by mixing 380 µL pure ethanol and 100 µL DI water. 2 mg of catalyst was added to the solution and placed into an ultrasonic bath for 20 min. Then, 5 µL of 5 wt. % Nafion solution was taken and added to the prepared solution to mix for 20 min. 10 µL of homogeneous ink was dropped on

the pre-cleaned GC surface and distributed homogenously. Lastly, the catalyst-coated GC electrode was kept at 80 °C for 120 min under the air atmosphere. The 10 % Pt/C and RuO_2 reference electrodes were prepared with the same technique.

The chronopotentiometry was utilized to examine the long-term durability of electrodes at 10 mA cm^{-2} for 12 h. LSV towards OER and HER were conducted before and after 1000 cycles with a 5 mV s^{-1} scan rate. Additionally, a frequency range between 100 kHz and 0.1 Hz was applied for the electrochemical impedance spectroscopy (EIS) measurements with 10 mV of a sinusoidal voltage.

The double-layer capacitance parameter (C_{dl}), which provides the electrochemically active surface area (ECSA), was obtained from cycling voltammetry (CV) measurements in the non-Faradaic region. CV experiments were conducted at varying scan rates (0.02, 0.04, 0.08, 0.16, 0.32 and 0.64 V s^{-1}) across a potential region of 0.25–0.35 V (vs RHE). The reason was to take the potential window as 0.1 V, which was located on the system's open circuit potential (OCP) (0.35 V). The working electrode was kept at the potential vertex for 10 s before the next sweep.

Oxygen Evolution Behavior

As evidenced by previous literature, tungsten borides have been considered as electrochemical water splitting electrocatalysts for hydrogen evolution [52]. To get a perspective on the bifunctional property of WB_2 electrocatalysts synthesized via both methods, the oxygen evolution reaction (OER) behavior of parent and metal-substituted WB_2 were scrutinized under 1 M KOH electrolyte, by loading 0.5 mg/cm^2 catalyst powder on the GC electrode. The outcomes are documented in **Figure 20a** and **Figure 21**. The OER behavior of RuO_2 as a reference material was also evaluated for comparison. Not to mention that to show the negligible impact of GC on the behavior of electrocatalysts, the OER activity of GC has been likewise included. Observation of **Figure 20a** indicates that WB_2/ms demands an inferior OER activity. Analogous to WB_2/ms, the bare WB_2/ct was also signified mediocre OER performance with a potential of 1.71 V (vs RHE) to afford a current density of 10 mA cm^{-2}. In this regard, an overpotential of 480 mv versus their equilibrium value of 1.23 V (vs RHE) can be calculated which is practically high for OER thermodynamic process. It is widely believed that doping/substitution with a heteroatom is an effective way to alleviate the overpotential needed for the OER process [53]. In this

regard, Co and Ni substitutions were conducted to experimentally regulate the electronic structure of the surface.

From **Figure 20a** and **Figure 21**, it is obvious that decorating the parent structure with Ni and Co could enhance the OER performance of WB_2 but in a different trend. For the samples synthesized by the molten-salt technique, Co substitution with the concentration of $x = 0.2$ ($W_{0.8}Co_{0.2}B_2$/ms) revealed an OER activity with an overpotential of 340 mV, the closest value to that of RuO_2 (an overpotential of 290 mV). This result is comparable to previously reported TMBs including Co-Mo-B (an overpotential of 320 mV) [54] and Co_2B (an overpotential of 330 mV) [55]. On the contrary, for the samples obtained by the carbothermal reduction method, $W_{0.9}Co_{0.1}B_2$/ct revealed the best OER performance among the other ones with an overpotential of 370 mV, which is still high compared to that of $W_{0.8}Co_{0.2}B_2$/ms sample. For both methods, a further increase in the concentration deteriorates the performance in a way that the overpotential required for OER increased to 360 and 390 mV for the respective $W_{0.7}Co_{0.3}B_2$/ms and $W_{0.8}Co_{0.2}B_2$/ct electrocatalysts (refer to **Table 1**). It must be pointed out that Ni-substituted WB_2 was a less active catalyst toward OER compared to that of Co-substituted. In this sense, $W_{0.7}Ni_{0.3}B_2$/ms exhibited an overpotential of 400 mV, the best overpotential on top of all Ni-substituted samples. To address this concern, it should be overemphasized that electrocatalytic performance is a function of multiple factors including the morphology and particle size, the electronic structure, and the surface-active sites. It was found that elemental substitution serves as a key to controlling the electronic structure, surface active sites, and even morphology [56].

OER as a half-reaction of water splitting encompasses a complicated process mechanism. It is well known that the OER process suffers from its sluggish kinetics compared to the cathodic half-reaction. The OER process moves forward through a four-electron transfer pathway in the alkaline medium as follows:

$$4OH^- \rightarrow O_2\,(g) + 2H_2O\,(l) + 4e^- \quad (6)$$

This reaction can be expressed in four-electron steps:

$$OH^- + M \rightarrow MOH + e^- \quad (7)$$

$$MOH + OH^- \rightarrow MO + H_2O + e^- \quad (8)$$

$$MO + OH^- \rightarrow MOOH + e^- \quad (9)$$

$$MOOH + OH^- \rightarrow M + O_2 + H_2O + e^- \quad (10)$$

where MOH, MO, and MOOH are three intermediates' products for a four-electron transfer pathway which M is referred to as the active site. In a general sense, metal borides have been classified as high-performing OER electrocatalysts. In many cases, boride could facilitate the oxidation of metal atoms by distorting native atomic geometry during the electron transfer process. As a consequence, the adsorption process of hydroxyl groups could readily be expeditated in metal boride's structure. In the sense of Co substitution, as evidenced by previous literature, CoOOH species can act as real active sites on the surface, and boron atoms the oxidation of Co could be accelerated by boron atoms [55] resulting in the promotion of OER activities in Co substituted samples. When it comes to different synthesis methods, as no surprise, molten salt provides a sponge-like structure **(Figure 10)** with a more surface-active area (explained by ECSA experiments discussed later), indicating decent OER activity. What is more, it is shown that metal substitution can regulate electronic structure through their *d*-band center [57]. In the light of these results, the *d*-band center can predict the absorption of oxygen-containing intermediates such as OH^*, $OOH^*$and H^* on the catalyst surface, thereby it is able to anticipate the possibility of the OER reaction. For instance, as evidenced by the DFT study [58], Fe substitution in the host material of Ni_2P could enhance the density of states (DOS) near the Fermi level resulting in an increase in the energy level of the *d*-band of the host material. Eventually, this increase balances the adsorption and desorption of the intermediates of OH^*, $OOH^*$and H^* boosting the electrocatalytic OER performance. Not to mention that, as discussed in our previous works [32], [59], there is a certain extent of metal incorporation into the host material (in the case of present work x = 0.2 for $W_{1-x}Co_xB_2$/ms, x = 0.1 $W_{1-x}Co_xB_2$/ct and x = 0.3 for $W_{1-x}Ni_xB_2$/ms), which is established via optimal value for *d*-band energy. Further enhancement in the substitution level may cause undesired bonding of M-M rather than M-B.

To dig deeper into the OER mechanism, the Tafel plots of OER reactions were plotted as the required overpotential against the current density. The slopes of these plots are used as an index to determine the OER kinetics. **Figure 20b** reveals the Tafel plots of parent and metal-substituted WB_2. From this figure, the $W_{0.8}Co_{0.2}B_2$/ms holds the lowest Tafel slope (113.6 mV dec^{-1}) close to the commercial RuO_2 (72.8 mV dec^{-1}) over all other

samples indicating a faster enlargement of the current density as a function of overpotential, thereby more facile kinetics for OER reaction. In this sense, the decent OER performance of $W_{0.8}Co_{0.2}B_2$/ms compared to the other samples can be expected. The relevant Tafel slopes for the samples included in **Figure 21** are listed in **Table 1**.

By taking into account that the commercial RuO_2 suffers from low stability under the harsh oxidizing conditions of OER, introducing an active and stable electrocatalyst is considered a demand to be fulfilled. For this purpose, a CV experiment up to 1000 cycles at a potential range of 1.2 and 1.8 V was applied on the best-performing catalyst, $W_{0.8}Co_{0.2}B_2$/ms. The OER performance before and after 1000 cycles of operation is portrayed in **Figure 20c.** Observation of the image indicates that the onset potential at 10 mA cm^{-2} has raised from 1.57 to 1.60 V (vs RHE) (only a slight deviation of 0.03 V) confirming satisfactory stability of $W_{0.8}Co_{0.2}B_2$/ms. In addition, the long-run durability of the $W_{0.8}Co_{0.2}B_2$/ms sample was measured for 12 h at the current density of 10 mA cm^{-2}. The results can be observed in **Figure 20d,** illustrating the decent OER stability of the $W_{0.8}Co_{0.2}B_2$/ms with only 22 % loss in overpotential after 12 h durability. It should be overemphasized that in the case of long-term stability, continuous coverage of the catalyst surface by evolved gas bubbles adversely affects the stability of the catalysts, and it remains almost far away from their actual stability. Therefore, the continuous increase of demanded overpotential during the long-term OER stability is explicable.

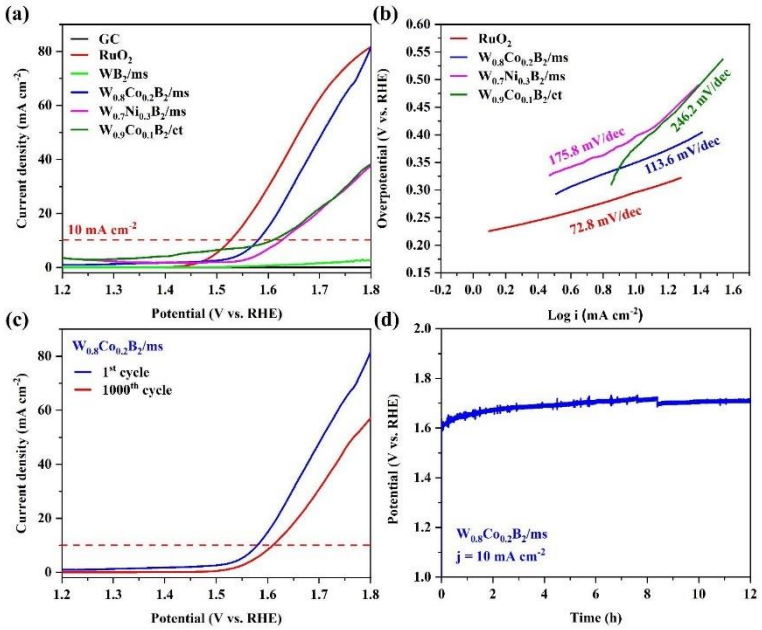

Figure 20. Electrochemical activity toward OER for the parent and metal-substituted WB_2 synthesized by molten-salt (ms) and carbothermal (ct) methods recorded in 1 M KOH at a scan rate of 5 mV s^{-1}. a) Polarization curves, b) Related Tafel plots, c) Polarization curves of best-performing $W_{0.8}Co_{0.2}B_2$/ms initially and after 1000 CV scans at 100 mV s^{-1}, and d) Chronopotentiometric curve of $W_{0.8}Co_{0.2}B_2$/ms recorded at a current density of 10 mA cm^{-2}.

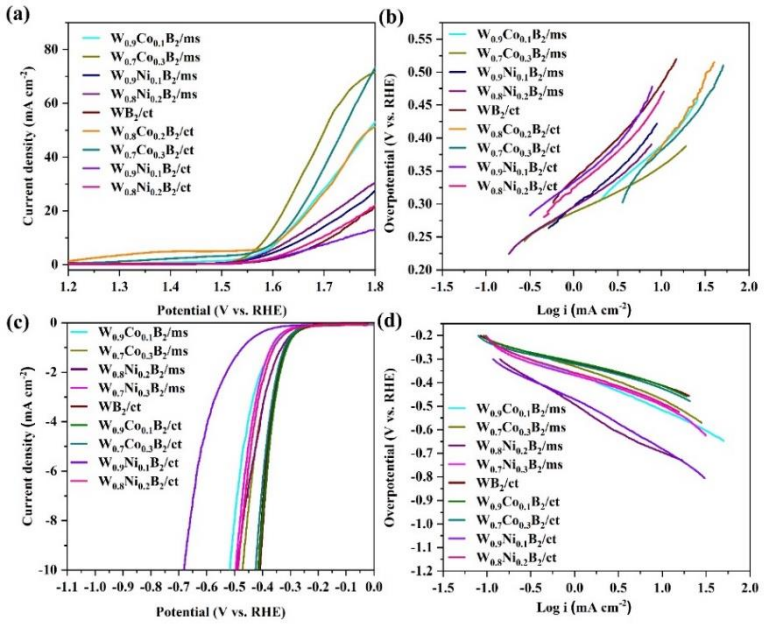

Figure 21. Electrochemical activity of parent and metal substituted WB_2 synthesized by molten salt (ms) and carbothermal (ct) methods recorded in 1 M KOH at a scan rate of 5 mV s^{-1}. (a) OER polarization curves, (b) Related OER Tafel plots, (c) HER polarization curves, and (d) Related HER Tafel plots.

Table 1. Summary of electrochemical parameters for all as-prepared samples.

Sample	OER potential (V)	OER Tafel slope (mV dec^{-1})	HER potential (V)	HER Tafel slope (mV dec^{-1})
WB_2/ms	-	-	0.671	180
$W_{0.9}Co_{0.1}B_2$/ms	1.62	118.6	0.515	153
$W_{0.8}Co_{0.2}B_2$/ms	**1.57**	**113.6**	**0.363**	**94.2**
$W_{0.7}Co_{0.3}B_2$/ms	1.59	171.6	0.471	155.4
$W_{0.9}Ni_{0.1}B_2$/ms	1.66	122.9	0.427	108.1
$W_{0.8}Ni_{0.2}B_2$/ms	1.64	193.7	0.490	208.7
$W_{0.7}Ni_{0.3}B_2$/ms	1.63	175.5	0.495	140.5
WB_2/ct	1.71	146.6	0.410	97.5
$W_{0.9}Co_{0.1}B_2$/ct	1.60	246.2	0.412	98.5
$W_{0.8}Co_{0.2}B_2$/ct	1.62	195.7	0.373	103.1
$W_{0.7}Co_{0.3}B_2$/ct	1.62	159.7	0.425	101.1
$W_{0.9}Ni_{0.1}B_2$/ct	1.74	141.8	0.681	200.7
$W_{0.8}Ni_{0.2}B_2$/ct	1.70	129.9	0.488	130.1

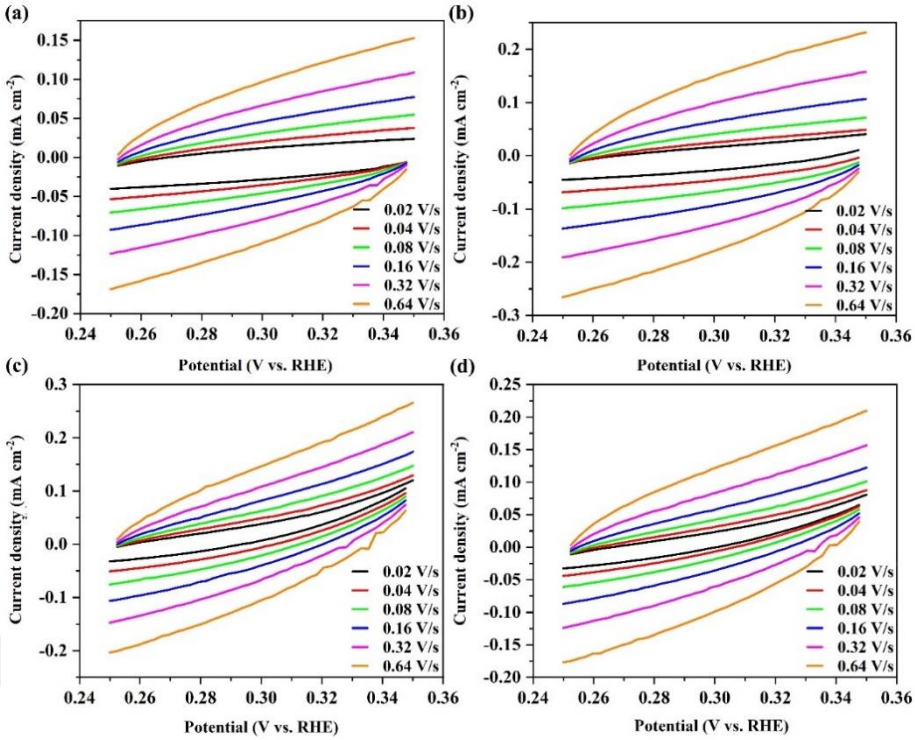

Figure 22. Cyclic voltammograms of a) WB_2/ms, b) $W_{0.8}Co_{0.2}B_2$/ms, c) $W_{0.7}Ni_{0.3}B_2$/ms and d) $W_{0.8}Co_{0.2}B_2$/ct at various scan rates.

Hydrogen Evolution Behavior

Analogous to oxygen evolution, the same scenario was repeated for the hydrogen evolution. Thus, in the HER case, 0.5 mg cm^{-2} of catalyst was loaded on the GC electrode and a negative potential window was conducted in 1 M KOH. **Figure 23a** depicts the relevant LSV curves. For the sake of comparison, the results of commercial 10 % Pt/C as a benchmark HER catalyst and GC as an inert substrate have been introduced in the curves. A glance at these graphs discloses that the parent WB_2 is not very active in HER, showing an overpotential of 671 mV at 10 mA cm^{-2}, significantly far from the commercial Pt/C material (with an overpotential of 198 mV). On the contrary, metal substitution causes a dramatic alteration in the activity of the WB_2. In this regard, the $W_{0.8}Co_{0.2}B_2$/ms sample with an overpotential of 363 mV is the closest value to that of Pt/C that we could reach in this work. In addition, $W_{0.8}Co_{0.2}B_2$/ct with an overpotential of 373 mV manifested the best HER performance amidst the catalysts synthesized via the carbothermal method and was quite identical to that of $W_{0.8}Co_{0.2}B_2$/ms. It must be noted that Ni-substituted WB_2 manufactured by both methods exhibited far lower HER performance compared to Co-substituted one as $W_{0.9}Ni_{0.1}B_2$/ms reached 427 mV overpotential at 10 mA cm^{-2}. It was reported that Co-based borides are known as powerful

electrocatalysts for hydrogen evolution which is in line with our case. For this study, $W_{0.8}Co_{0.2}B_2$/ct can be compared with Co_2B-500 with an overpotential of 328 mV [16]. Besides, identical to OER, a further increase in the substitution concentration undermines the performance of hydrogen evolution (see **Table 1**).

For the HER, the ideal value for the adsorption Gibbs free energy (ΔG_{H^*}) of atomic hydrogen to the available active site should be close to zero. Concerning the high-performing Pt-based materials, $\Delta G_{H^*} \approx 0$ [4]. When it comes to borides; in fact, they possess distinguished electronic structures which can adjust the surface adsorption energy. Therefore, identical to the OER, the HER performance of metal diborides is also connected with the d-band center of metals [60], [61]. Hence, it can be mentioned that the electronic structure—d-band center—not only can be altered by Co substitution but also can be influenced by the substitution concentration [62], [63].

For the case of HER, the Tafel slope is a fundamental parameter to appraise the rate-determining step through the HER and in turn ascertain the HER reaction kinetics. For this, the related Tafel plots are shown in **Figure 23b**, exhibiting a direct relationship between current density and overpotential. Concerning earlier reports [64], two general routes can be envisaged for the evolution of hydrogen (adsorption and desorption) under alkaline media—either it should conform to Volmer (adsorption step)–Heyrovsky mechanism (Equations 11 and 12) or the Volmer-Tafel mechanism (Equations 13 and 14):

Volmer step:

$$H_2O + e^- \rightarrow OH^- + H^* \quad (11)$$

Heyrovsky step:

$$H_2O + e^- + H^* \rightarrow OH^- + H_2 \quad (12)$$

Volmer step:

$$H_2O + e^- \rightarrow OH^- + H^* \quad (13)$$

Tafel step:

$$H^* + H^* \rightarrow H_2 \quad (14)$$

where H^* is the adsorbed hydrogen on the surface of the catalyst under basic solutions. Within alkaline conditions, hydrogen binds to the catalyst via the Volmer adsorption, followed by the desorption process through the Heyrovsky step (so-called electrochemical desorption step) or Tafel step (known as the chemical desorption step). The estimated values in terms of Tafel slope for the Volmer, Heyrovsky, and Tafel steps are as follows ~120 mV dec^{-1}, ~40 mV dec^{-1}, and ~30 mV dec^{-1}, respectively [14], [65].

In the case of current work, the results verified that the $W_{0.8}Co_{0.2}B_2$/ms has the lowest Tafel slope (93.2 mV dec^{-1}), even smaller than $W_{0.8}Co_{0.2}B_2$/ct (103.6 mV dec^{-1}) and very close to the commercial Pt/C (85.2 mV dec^{-1}) indicating a faster growth of current density as a function of overpotential, thereby more facile kinetics for HER reaction. On the flip side, parent WB_2 and $W_{0.9}Ni_{0.1}B_2$/ms samples hold Tafel slopes of 108.1 and 180.3 mV dec^{-1} signifying slow kinetics and less HER activity. Based on these results and equations (11) – (14), it has been evinced that the dominating path for hydrogen adsorption in the samples is through the Volmer mechanism. The related Tafel slopes of the different substituted concentrations (reported in **Figure 21d)** are also listed in **Table 1**.

To assess the HER stability, the best-performing sample, $W_{0.8}Co_{0.2}B_2$/ms, was undergone a CV experiment up to 1000 cycles within a potential range of 0 and -1 V. The HER performance before and after 1000 cycles of operation is demonstrated in **Figure 23c**. The outcomes unraveled the superior durability of $W_{0.8}Co_{0.2}B_2$/ms with a drop from 363 to 354 mV in the overpotential values after 1000 sweeps. The same trend was also observed in our previous experimental studies [32], [59] in that a decline in HER overpotential originates from the electrocatalyst surface which is covered by adsorbed hydrogen throughout the stability sweeps. Meanwhile, the long-run durability of the best-performing HER catalyst, $W_{0.8}Co_{0.2}B_2$/ms, was measured for 12 h at the current density of 10 mA cm^{-2} and the outcome can be seen in **Figure 23d**. From the figure, $W_{0.8}Co_{0.2}B_2$/ms reveals superb durability with only 12% loss in overpotential after 12 h.

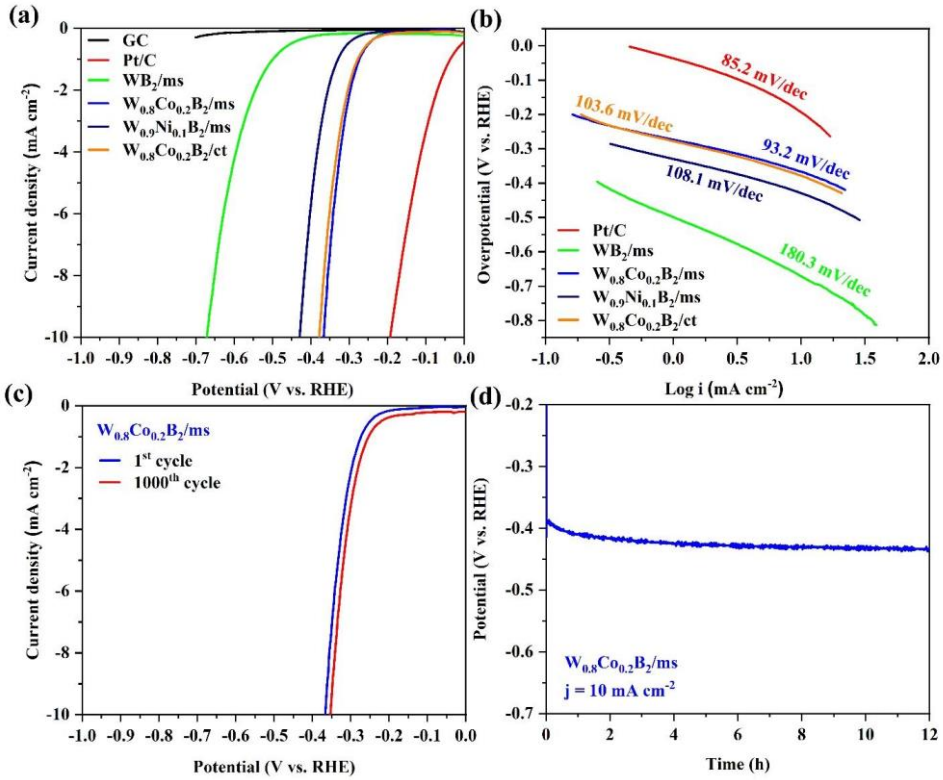

Figure 23. Electrochemical activity toward HER for the parent and metal-substituted WB_2 synthesized by molten-salt (ms) and carbothermal (ct) methods recorded in 1 M KOH at a scan rate of 5 mV s^{-1}. (a) Polarization curves, (b) Related Tafel plots, (c) Polarization curves of best-performing $W_{0.8}Co_{0.2}B_2$/ms initially and after 1000 CV scans at 100 mV $s^{-1,}$ and (d) Chronopotentiometric curve of $W_{0.8}Co_{0.2}B_2$/ms recorded at a current density of 10 mA cm^{-2}.

By taking into account the consequences of electrochemical evaluation, it seems that the relevant results are firmly correlated to the TM and the morphology of catalysts. To further broaden our knowledge on these effects, the electrochemically active surface area (ECSA) was conducted by exploiting electrochemical double-layer capacitance (C_{dl}). The ECSA was evaluated based on the report of McCrory *et al.* [48], in which the CV at multiple scan rates was performed in a non-Faradaic potential region. This region is determined in a 0.1 V window centered at the open-circuit potential (OCP). The resulting CV curves are shown in **Figure 22**. The ECSA was measured through the C_{dl} as follows:

$$i_c = \nu C_{dl}$$

where i_c and ν are double layer current at OCP (center of potential window) and scan rate. Thereby, plotting i_c against ν brings in a slope of C_{dl}. **Figure 24a** reveals the ECSA plots and relevant calculated C_{dl} for parent WB_2/ms, $W_{0.8}Co_{0.2}B_2$/ms, $W_{0.7}Ni_{0.3}B_2$/ms

synthesized by the molten salt, and for the sake of comparison $W_{0.8}Co_{0.2}B_2$/ct synthesized by the carbothermal method. When looking at the calculated C_{dl} values, the C_{dl} value for parent WB_2/ms is 0.128 mF cm^{-2} which is lower than the $W_{0.8}Co_{0.2}B_2$/ms (0.247 mF cm^{-2}) and $W_{0.7}Ni_{0.3}B_2$/ms (0.178 mF cm^{-2}). So, it is obvious that the substituted WB_2 catalysts have exhibited a higher surface-active area than the parent ones. As also firmly validated by our previous works [32], [65]the nature of the alloying constituent along with particle size can strictly affect the ECSA. It is proved that in the PtM/C catalysts, the composition can affect the degree of the agglomeration. What is more, when the metallic nanoparticles cover with oxide/hydroxide components, the portion of nanoparticles could be insulated by the oxides, resulting in a decline in the active sites [66]. When looking at the metal substituted WB_2, the EDS analysis of oxygen content (**Table 2**) shows that the substitution of parent structure diminished the oxygen content in the particle. As parent WB_2/ms has a higher portion of O/W (0.92) compared to $W_{0.8}Co_{0.2}B_2$/ms, and $W_{0.7}Ni_{0.3}B_2$/ms (with an O/W portion of 0.44 and 0.22, respectively), it then undergoes a higher degree of insulation caused by oxide/hydroxide compounds and brings about inferior ECSA. When it comes to $W_{0.8}Co_{0.2}B_2$/ct, despite the low portion of O/W, it still holds an inferior C_{dl} value of 0.153 mF cm^{-2} compared to $W_{0.8}Co_{0.2}B_2$/ms probably due to coarse and rough morphology with an irregular shape of the carbothermal synthesized powders.

Table 2. The O/W ratios from EDS analysis of parent and substituted WB_2 powders.

Sample (at.%)	**W**	**O**	**O/W**
WB_2/ms	51.94	47.86	0.92
$W_{0.8}Co_{0.2}B_2$/ms	69.52	30.49	0.44
$W_{0.7}Ni_{0.3}B_2$/ms	81.82	18.18	0.22
$W_{0.8}Co_{0.2}B_2$/ct	71.58	28.58	0.39

To get a deeper understanding of the electrochemical behavior of the catalysts in alkaline solution, the electrochemical impedance spectroscopy (EIS) measurements were conducted. **Figure 24b** demonstrates the related Nyquist plots along with the equivalent circuit. Meanwhile, the fitting data by ZView software are tabulated in **Table 3**. From **Figure 24b**, the resistance trend maintains nearly the same for all samples. The equivalent

circuit is made up of electrolyte resistance between the working and reference electrode (R_e) along with the impedance of the interfacial reaction describing a constant-phase element (CPE) and a series combination of Faraday resistance (R_{ct}) and Warburg impedance (W) due to diffusion which is the controlling step on the interface. According to the fitted values presented in **Table 3**, the parent WB_2/ms suffers from high Warburg diffusion resistance (4254 Ω). On the contrary, the incorporation of Co and Ni into the parent structure significantly reduced diffusion resistance. Still, Ni-incorporated samples suffer from high Faraday resistance which eventually led to their unsatisfactory catalytic behavior against the Co-incorporated sample. The $W_{0.8}Co_{0.2}B_2$/ms, however, enjoys both lower Faraday and diffusion resistances (40 and 803.9 Ω, individually). What is significant here is that Co-incorporated materials synthesized by the carbothermal method showed high Faraday and diffusion resistances probably due to their rough topography which slows down the diffusion rate on the interfacial surfaces.

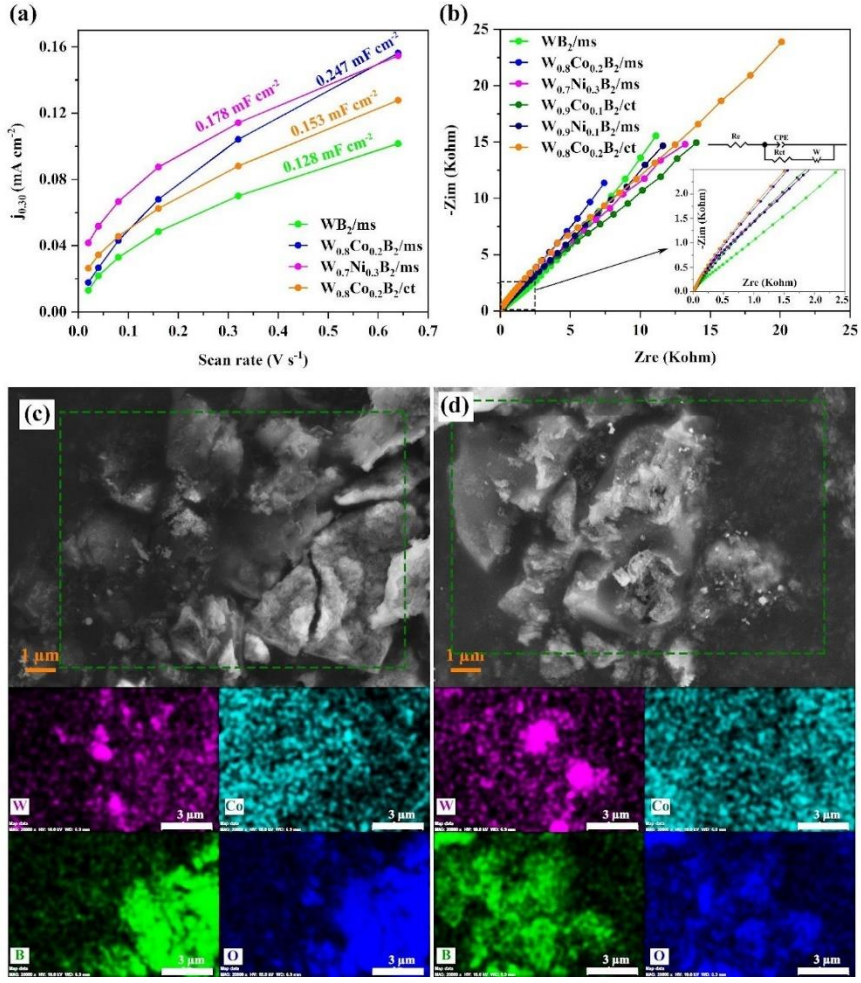

Figure 24. a) Capacitive currents from CV measurements plotted as a function of scan rate of parent and metal substituted WB_2 synthesized by molten salt (ms) and carbothermal (ct) methods, b) Nyquist representation of EIS data collected at 0 V and equivalent circuit, SEM images and related EDS elemental mapping analyses showing electrode surface morphology and structural elements of best-performing $W_{0.8}Co_{0.2}B_2$/ms after 12 h c) OER stability, and d) HER stability.

Table 3. Fitted values of the equivalent circuit elements for the samples.

Sample	R_e (Ω)	CPE-T ($mFsp^{-1}$)	CPE-P	R_{ct} (Ω)	W-R (Ω)
WB_2/ms	10.32	7.3×10^{-6}	0.88	100	4254
$W_{0.8}Co_{0.2}B_2$/ms	**11.34**	**8.4×10^{-5}**	**0.73**	**40**	**803.9**
$W_{0.9}Ni_{0.1}B_2$/ms	10.34	1.7×10^{-5}	0.82	2189	401.8
$W_{0.7}Ni_{0.3}B_2$/ms	10.05	3.4×10^{-5}	0.71	9520	204.4
$W_{0.9}Co_{0.1}B_2$/ct	9.56	1.8×10^{-5}	0.69	5249	937.2
$W_{0.8}Co_{0.2}B_2$/ct	10.78	1.4×10^{-6}	0.78	3942	5012

The morphological and compositional alterations were studied on the best-performing material after stability and electrochemical evaluations. The results of SEM and EDS analyses are visualized in **Figure 24c,d** and **Figure 25**. From **Figure 24c,d**, it can be claimed that the surface of $W_{0.8}Co_{0.2}B_2$/ms did not go under a noticeable deterioration after 12 h OER and HER stabilities, indicating its robust tolerance under basic media. Moreover, the related EDS elemental mappings validated the homogeneous distribution of Co even after 12 h. The same observations were made after one OER/HER with no morphological and compositional degradation (see **Figure 25**). It should be mentioned that there is an immense increase in the surface oxygen content after 12 h stability for both OER and HER, verifying the formation of a huge portion of oxidized species during the stability (**Table 4**). In this context, as we previously discussed in detail [26], during continuous OER/HER measurements, the Co-O bonds were to a great extent replaced by the Co-B bonds on the electrode surface.

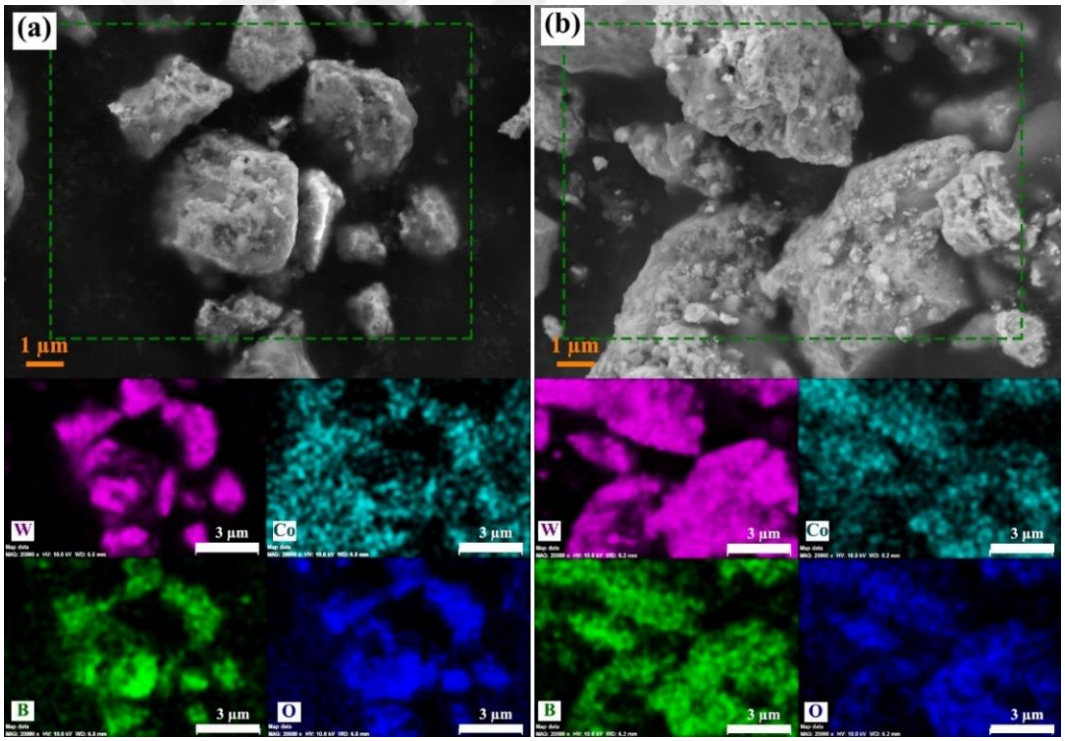

Figure 25. SEM images and related EDS elemental mapping analyses showing electrode surface morphology and structural elements of best-performing $W_{0.8}Co_{0.2}B_2$/ms after a) OER, and b) HER experiment.

Table 4. The O/W ratios from EDS analysis of best-performing $W_{0.8}Co_{0.2}B_2$/ms electrode.

EDS analysis	Sample (at.%)	W	O	O/W
After OER	$W_{0.8}Co_{0.2}B_2$/ms	10.49	89.51	8.5
After HER	$W_{0.8}Co_{0.2}B_2$/ms	18.51	81.49	4.40
After 12 h OER	$W_{0.8}Co_{0.2}B_2$/ms	0.27	99.73	369.37
After 12 h HER	$W_{0.8}Co_{0.2}B_2$/ms	0.37	99.63	269.22

Chapter 3: **Synthesis and Characterization of Molybdenum Diborides**

3.1 Synthesis of Electrocatalysts

Molybdenum oxide powder (MoO_3, 99.9% metal basis) and boron oxide powder (B_2O_3, 99% metal basis) were purchased from Alfa Aeasar. Nickel oxide (NiO, 99.99% trace metals basis), cobalt oxide (Co_2O_3, 99.99% trace metals basis), activated charcoal powder (C, pure), sodium chloride (NaCl, 99 %), and potassium chloride (KCl, 99 %) were purchased from Sigma Aldrich. Amorphous nano boron powder (B, 98.5%) was purchased from Pavtec.

3.1.1 Molten Salt-Assisted Synthesis

Similar to WB_2 electrocatalysts, MoB_2 can be synthesized by molten salt-assisted technique. In this part, instead of using metal basis reagents, oxide forms of Mo and TM (Co_2O_3 and NiO) were used. For the synthesis of pristine MoB_2, Co-substituted MoB_2 and Ni-substituted MoB_2, Eq. (15), (16), and (17) were used, respectively.

$$MoO_{3(s)} + 4\ B_{(s)} \rightarrow MoB_{2(s)} + B_2O_{3(g)} \quad (15)$$

$$(1\text{-}x)\ MoO_{3(s)} + x\ Co_2O_3 + 4\ B_{(s)} \rightarrow Mo_{1-x}TM_xB_{2(s)} + B_2O_{3(g)} \quad (16)$$

$$(1\text{-}x)\ MoO_{3(s)} + x\ NiO + 4\ B_{(s)} \rightarrow Mo_{1-x}TM_xB_{2(s)} + B_2O_{3(g)} \quad (17)$$

Identical to our earlier reports [18, 26, 28] and similar to the molten-salt technique of WB_2, all the preparation, weighing, and transferring of the precursors into the stainless-steel vial were conducted in an Ar-filled glovebox. The powder precursor was mechanically activated for 10 min at 1200 rpm. For the MoB_2 heat treatment, the sample was placed into the vertical furnace and kept at 1173 K for 60 min under constant Ar flow. The further steps were utilized completely the same with WB_2/ms. The MoB_2 electrocatalysts synthesized by molten salt were labeled as $Mo_{(1-x)}TM_{(x)}B_2$/ms.

3.1.2 Carbothermal Reduction Synthesis

Molybdenum diboride electrocatalysts with carbothermal reduction were synthesized according to the previous studies [27]. MoO_3, B_2O_3, and activated carbon powder were used as the main ingredients to manufacture the virgin MoB_2. Ni and Co (x = 0, 0.1, 0.2, and 0.3) substitutional ratios were used as the weight percentages.

$$(1\text{-}x)\ MoO_{3\,(s)} + x\ TM_{\,(s)} + B_2O_{3\,(s)} + (6\text{-}3x)\ C_{\,(s)} \rightarrow Mo_{1-x}TM_xB_{2\,(s)} + (6\text{-}3x)\ CO_{\,(g)} \quad (18)$$

All the experimental steps were conducted with the same conditions of tungsten diborides via carbothermal reduction. It is worth noting that catalysts manufactured by the carbothermal reduction method were marked as $Mo_{(1-x)}TM_{(x)}B_2$/ct.

3.2 Characterization of Electrocatalysts

3.2.1 Chemical Characterization

X-Ray Powder Diffraction (XRD)

Figure 26 presents the XRD results of $Mo_{(1-x)}TM_{(x)}B_2$ via molten salt samples to compare with theoretical diffraction peaks by substitution of Co and Ni. According to these results, MoB_2/ms and $Mo_{(0.95)}Co_{(0.05)}B_2$/ms were synthesized successfully without any impurities. However, when the Co and Ni amount increases, the crystalline structure of MoB_2 starts to decompose $Mo_2B_{4.026}$ even the elemental ratio between Mo and B is kept 2. Also, the intensities of $Mo_2B_{4.026}$ peaks were higher compared to MoB_2 ones in the higher amount Co and Ni substitutions. $Mo_{(0.95)}Ni_{(0.05)}B_2$/ms wasn't successful in terms of obtaining MoB_2 XRD peaks.

When the same amount of Co and Ni were compared, it can be easily said that the conversion of MoB_2 peaks to $Mo_2B_{4.026}$ became faster even for the 0.1 substitution. In Ni-substituted samples, there were just two different phases of Mo-B compound. However, there were unidentified and relatively high-intensity peaks at 35^o and 58^o in $Mo_{0.7}Co_{0.3}B_2$/ms, $Mo_{0.6}Co_{0.4}B_2$/ms, and $Mo_{0.5}Co_{0.5}B_2$/ms.

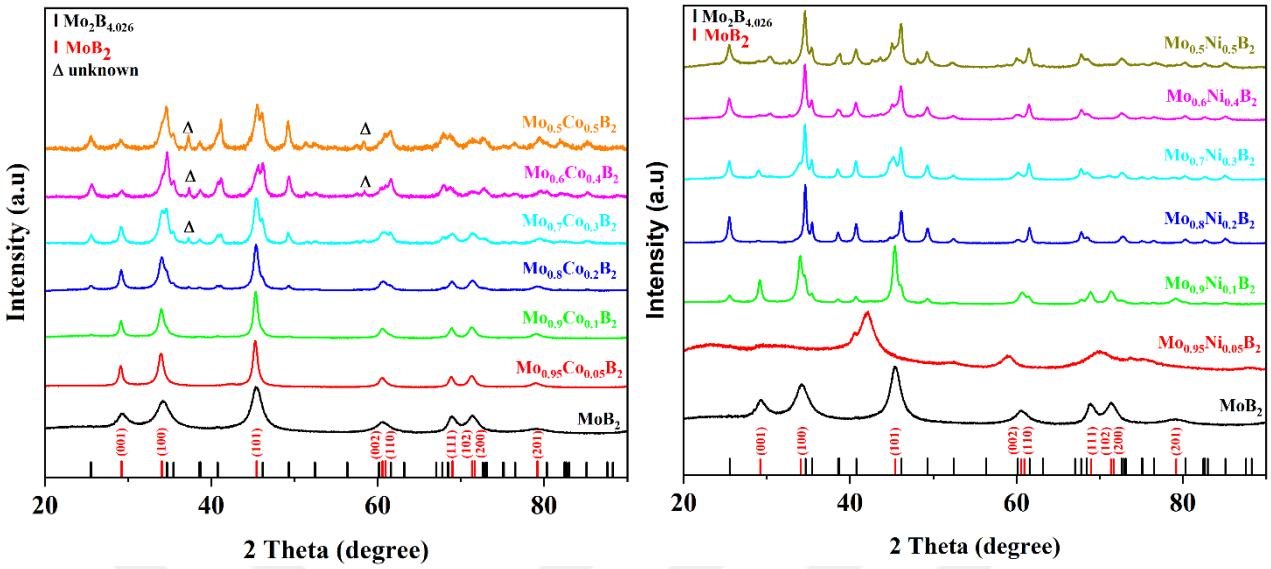

Figure 26. XRD patterns of a) $Mo_{1-x}Co_xB_2$ synthesized by molten salt (ms), and b) $Mo_{1-x}Ni_xB_2$ synthesized by by molten salt (ms).

In the carbothermal reduction case, well crystalline phases of $Mo_2B_{4.026}$ were obtained even the target phase was MoB_2 **(Figure 27)**. For the carbothermal reduction, synthesis of MoB_2 wasn't successful process in these conditions. However, the purity was almost 100 % without any secondary phases especially in Ni-substituted samples. In the Co-substituted $Mo_{(1-x)}TM_{(x)}B_2$/ct, B_4Co_2Mo peaks were encountered for the all three ratios.

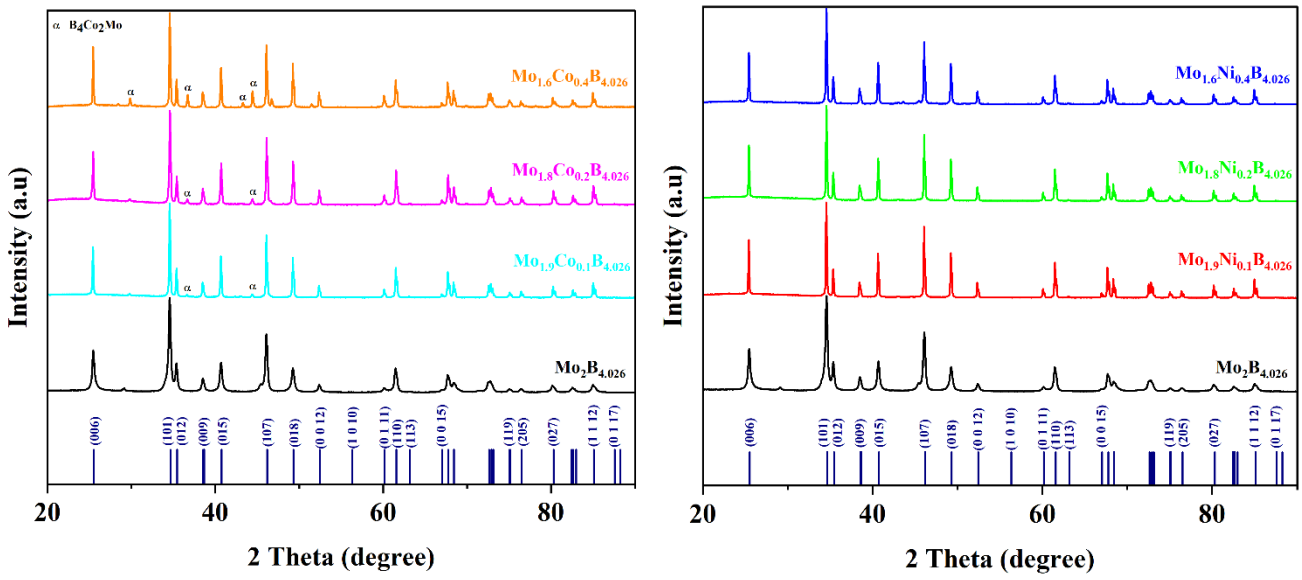

Figure 27. XRD patterns of a) $Mo_{1-x}Co_xB_2$ synthesized by molten salt (ms), and b) $Mo_{1-x}Ni_xB_2$ synthesized by by molten salt (ms).

By comparing between the molten salt and carbothermal reduction samples, it can be said that Ni was favored to produce $Mo_2B_{4.026}$ phase. The differences in crystal structures of MoB_2 and $Mo_2B_{4.026}$ were given in **Figure 28**. And there was peak broadening for the molten salt samples by supporting to the nano-sized structure of MoB_2 even with the Co and Ni substituted. Additionally, there were sharper peaks for the carbothermal reduction samples compared to molten salt ones by promoting the higher crystallinity in the structure. There was no significant change for the sharpness and broadening of peaks among samples via same synthesis method.

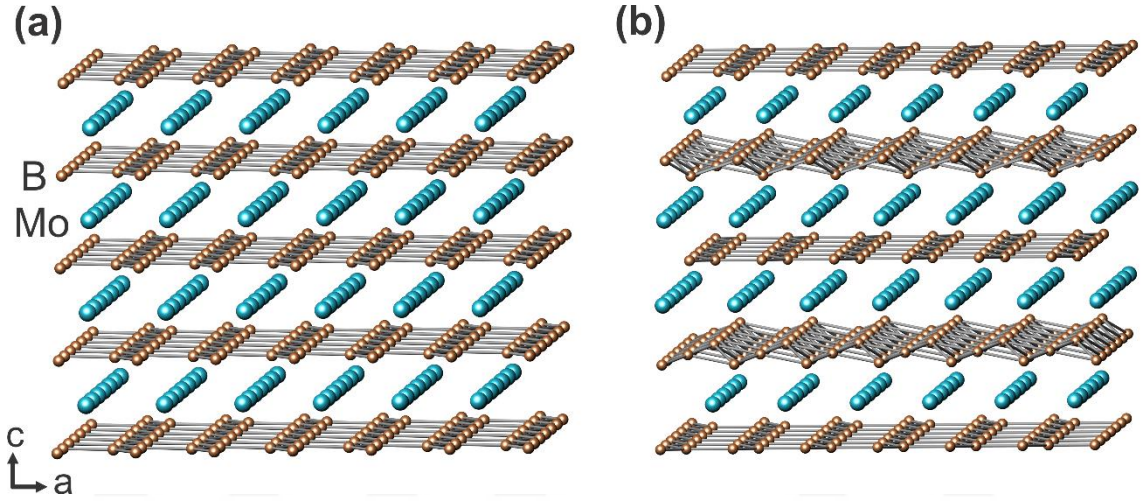

Figure 28. Crystal structures of MoB_2 and $Mo_2B_{4.026}$.

Scanning Electron Microscopy (SEM)

Figure 29 presents the MoB_2/ms at low and high magnifications at the right side. According to these images, MoB_2/ms have approximately 100 nm even less than 50 nm for smaller particles. And MoB_2/ms has generally spherical nanoparticles throughout the sample with the high connection between these nanoparticles.

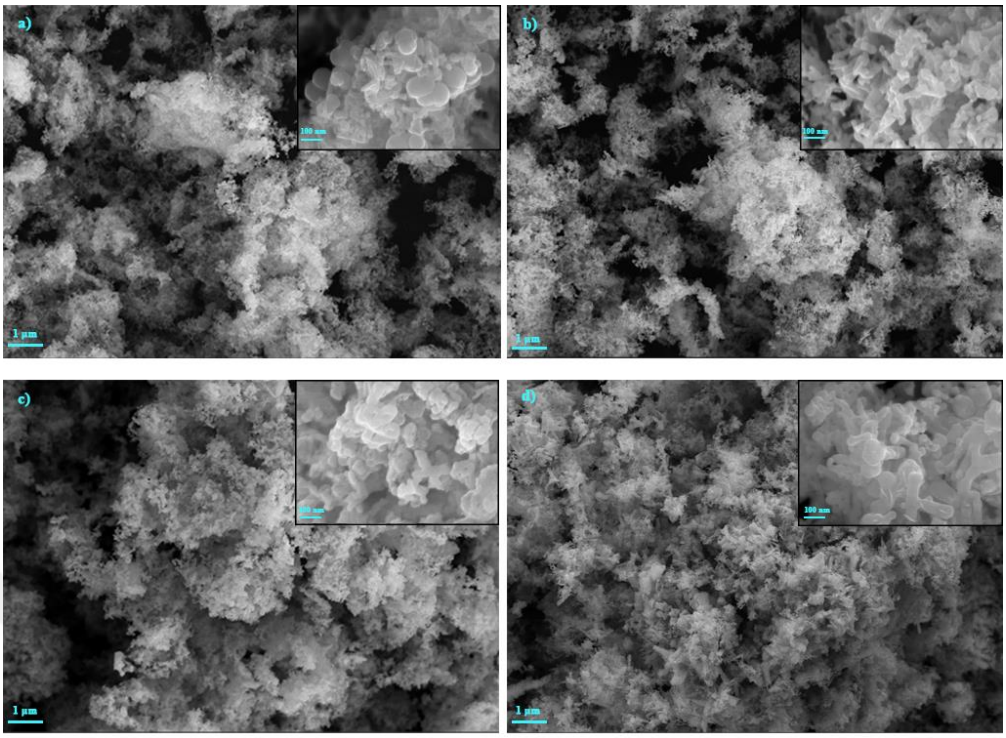

Figure 29. Low magnification SEM images of MoB_2/ms, $Mo_{0.9}Ni_{0.1}B_2$/ms, $Mo_{0.9}Co_{0.1}B_2$/ms, and $Mo_{0.8}Co_{0.2}B_2$/ms with their high magnification SEM images next to each.

For the smaller substitution ratios for example $Mo_{0.9}Ni_{0.1}B_2$/ms, $Mo_{0.9}Co_{0.1}B_2$/ms, and $Mo_{0.8}Co_{0.2}B_2$/ms at high magnifications (**Figure 29**), they have spherical nanoparticles still with the high connection similar to pristine MoB_2/ms but less.

Figure 30 and **Figure 31** show the effect of Ni and Co addition to sample by comparing with different ratios. By looking especially wide range for ratios like $Mo_{0.9}Ni_{0.1}B_2$/ms and $Mo_{0.5}Ni_{0.5}B_2$/ms or $Mo_{0.9}Co_{0.1}B_2$/ms and $Mo_{0.5}Co_{0.5}B_2$/ms, spherical particles alternated to branch shapes. However, nano-sized structure was still observed even for the $Mo_{0.5}Ni_{0.5}B_2$/ms and $Mo_{0.5}Co_{0.5}B_2$/ms.

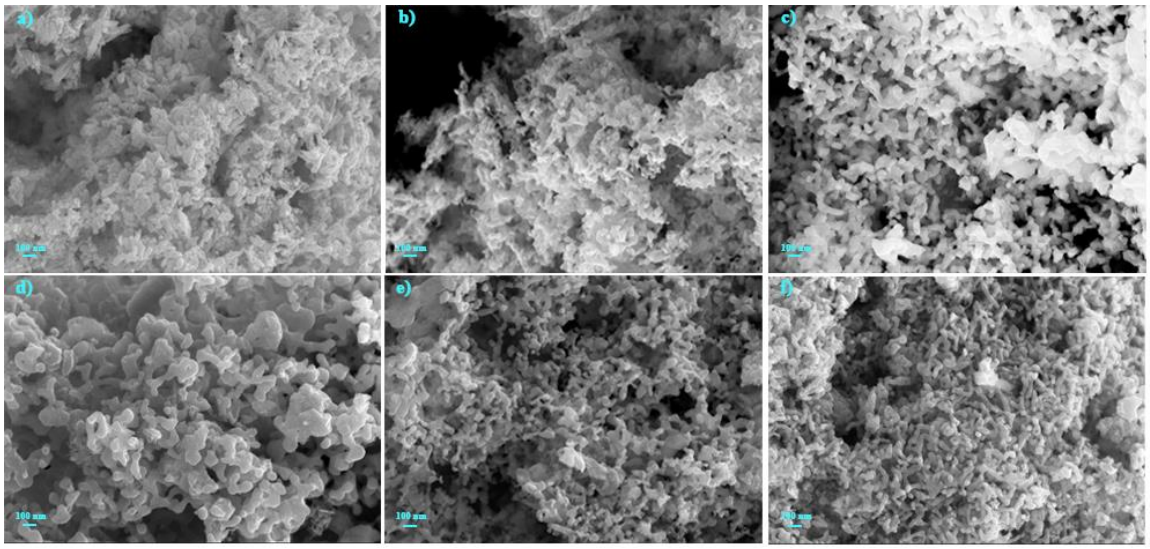

Figure 30. Low magnification SEM images of $Mo_{(1-x)}Ni_{(x)}B_2$/ms (x= 0.05, 0.1, 0.2, 0.3, 0.4, 0.5 respectively).

Low magnification EDS mappings of three different samples $Mo_{(1-x)}TM_xB_2$/ms (x= 0, Ni0.1, Co0.2) are presented in **Figure 32**. There was a thin layer of surface oxidation for all sample by showing these EDS mappings which couldn't be provided by XRD results earlier. According to **Figure 32**, each main element (Mo, B, Ni or Co) was nicely distributed all over the surface.

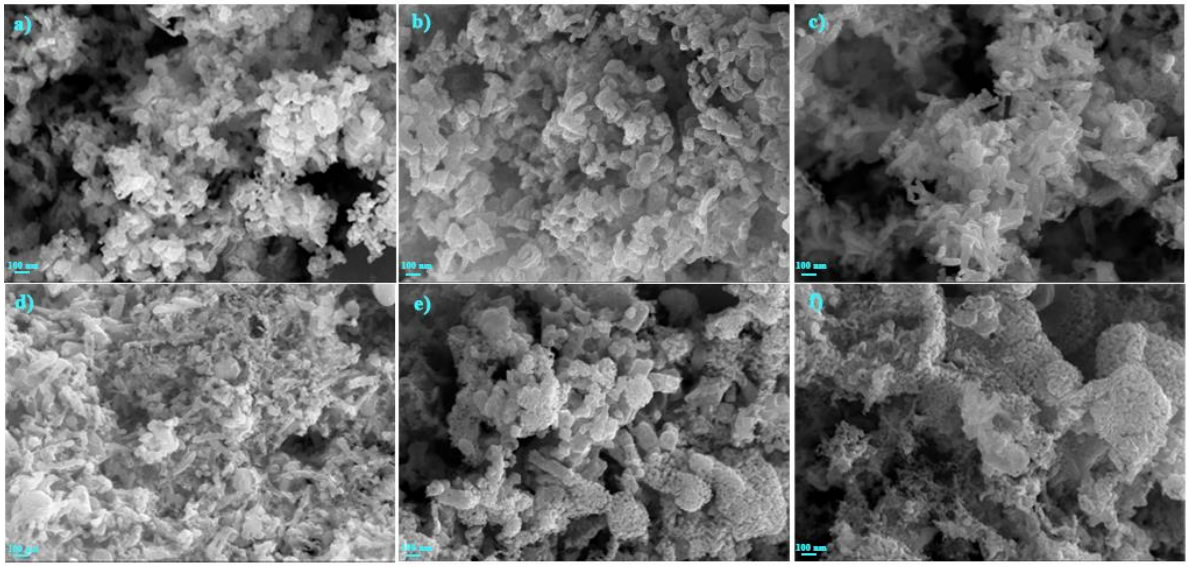

Figure 31. Low magnification SEM images of $Mo_{(1-x)}Co_{(x)}B_2$/ms (x= 0.05, 0.1, 0.2, 0.3, 0.4, 0.5 respectively).

$Mo_{(1-x)}TM_xB_2$/ct samples were analyzed similar to $Mo_{(1-x)}TM_xB_2$/ms to obtain information about their morphology and comparison between them. MoB_2/ct was shown in **Figure 33** by having branch like structure similar to high substitution ratio of $Mo_{(1-x)}TM_xB_2$/ms.

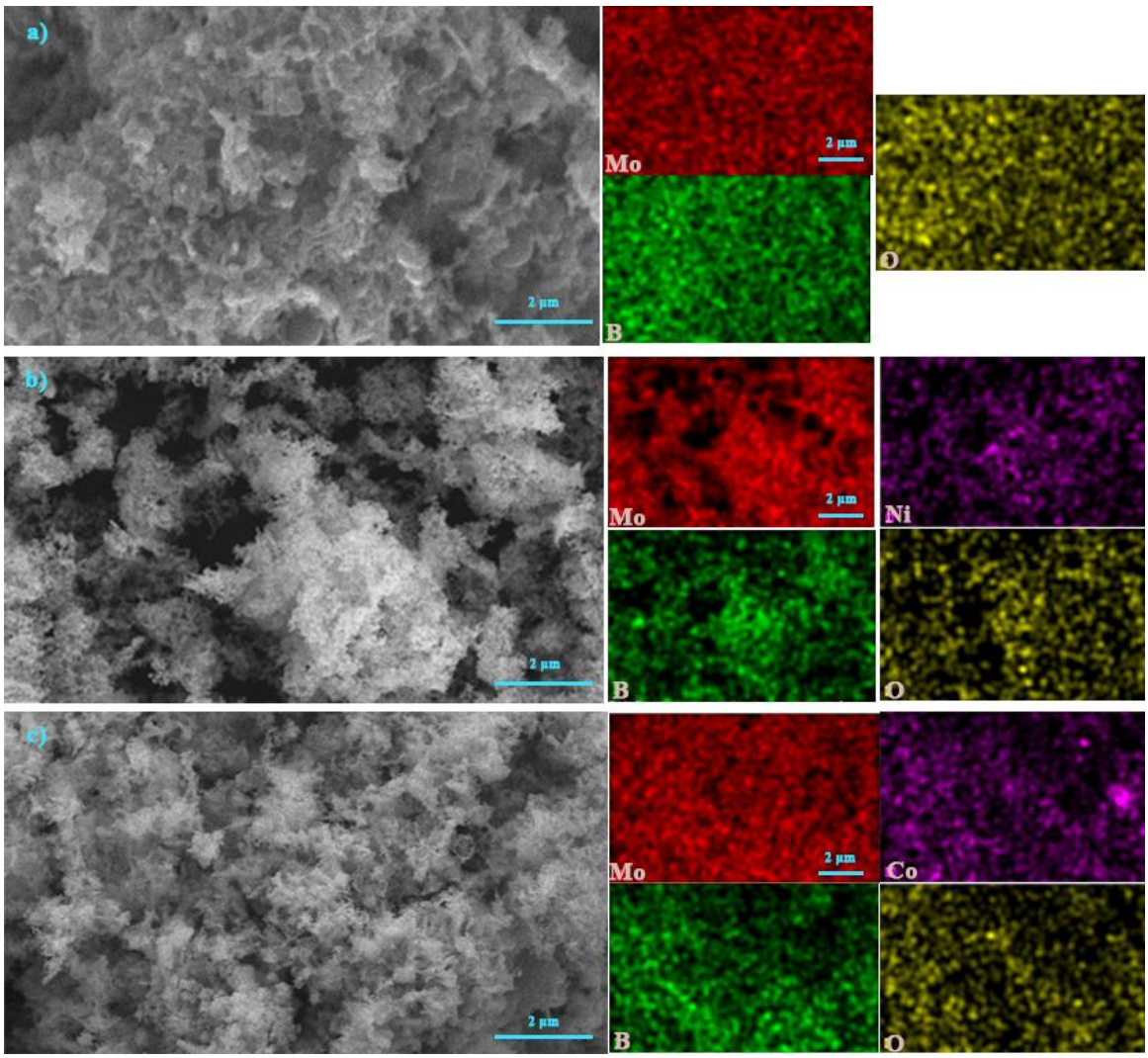

Figure 32. Low magnification SEM images of (a) MoB_2/ms, (b) $Mo_{0.9}Ni_{0.1}B_2$/ms, and (c) $Mo_{0.8}Co_{0.2}B_2$/ms with related EDS elemental mappings next to each.

There were spherical particles in some regions with less than 100 nm particle size even the amount of them is less. However, there was still a homogeneous distribution generally throughout the sample in terms of particle size and shape. High magnification EDS mapping of MoB_2/ct was shown in **Figure 33** in the left side also. According to these mappings, there was a smaller oxygen distribution at the surface compared to MoB_2/ms.

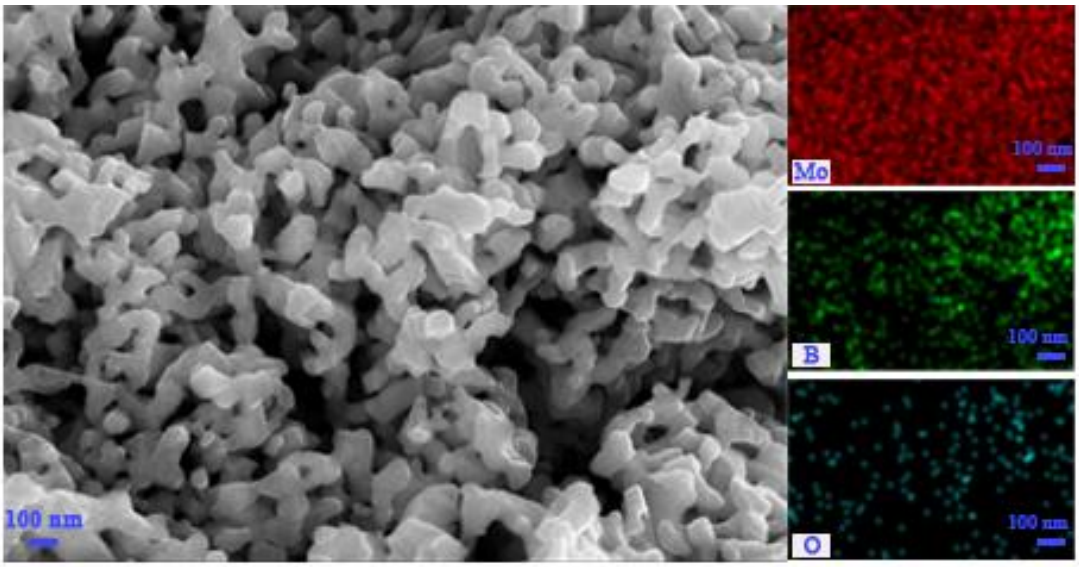

Figure 33. High magnification SEM image of MoB_2/ct and related EDS mapping next to.

When Ni was added to the MoB_2/ct, particle size of these samples increased (**Figure 34**). Also, $Mo_{(1-x)}Ni_xB_2$/ct samples lost their particle size and shape homogeneity. Cornered like particles occurred in the structure additional to the spherical ones.

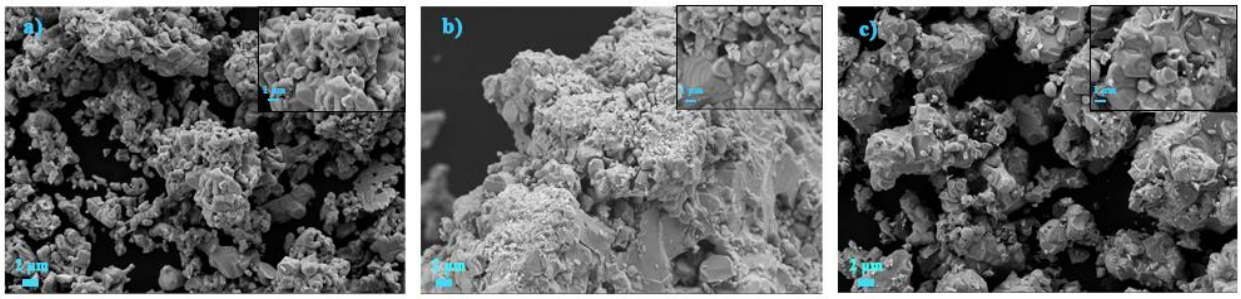

Figure 34. Low magnification SEM images of $Mo_{0.95}Ni_{0.05}B_2$/ms, $Mo_{0.9}Ni_{0.1}B_2$/ms , and $Mo_{0.8}Ni_{0.2}B_2$/ms with their high magnification SEM images next to each.

For $Mo_{(1-x)}Co_xB_2$/ct increase in the particle size was more distinguishable (**Figure 35**) than the $Mo_{(1-x)}Ni_xB_2$/ct because there were 1-2 μm particles even larger in same regions. Particles lost their spherical shape completely in this case.

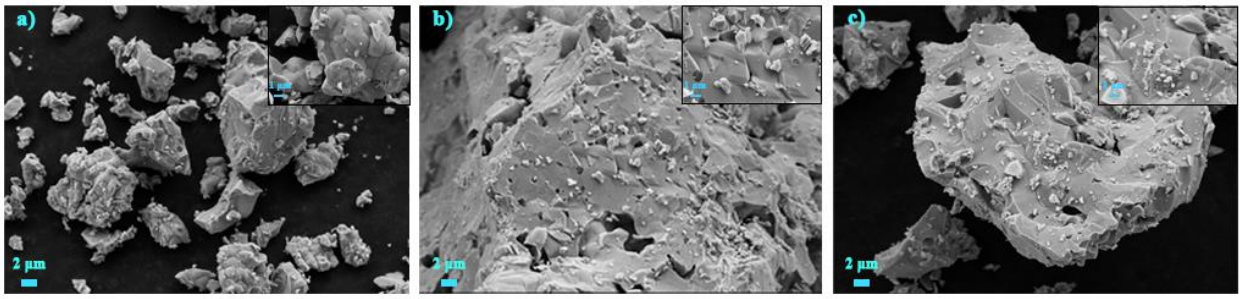

Figure 35. Low magnification SEM images of $Mo_{0.95}Co_{0.05}B_2$/ms, $Mo_{0.9}Co_{0.1}B_2$/ms, and $Mo_{0.8}Co_{0.2}B_2$/ms with their high magnification SEM images next to each.

X-ray Photoelectron Spectroscopy (XPS)

The electronic states and surface chemical composition of MoB_2 electrocatalyst were investigated via XPS analysis. XPS spectrum of Mo 3d, B 1s, Ni 2p, and O 1s were plotted in **Figure 37**. According to the deconvolution of $Mo_{0.9}Ni_{0.1}B_2$/ms **Figure 36**, there were two doublets located at 228.18, 229.18, and 232.28 eV corresponding to Mo $3d_{5/2}$ (MoB_2), Mo $3d_{5/2}$ (MoO_2), and Mo $3d_{5/2}$ (MoO_3), respectively (**Figure 36a**). From the literature, the first doublets correspond to Mo-B bond of MoB_2 (228 eV), the second doublets refer to Mo^{4+} oxidation state via Mo-O bonding of MoO_2 (229 eV), and the last doublets correspond to Mo^{6+} oxidation state via Mo-O bonding of MoO_3 [40]. There was a shift for these main peaks which could be due to the Ni substitution to the structure [30]. Additionally, the B 1s spectrum (**Figure 36b**) gives three different oxidation states by corresponding to B in metallic state at 186.9 eV and 188.38 eV, and B^{3+} at the 192.38 eV which comes from the metaborate species on the surface [49], [69]. The highest peak intensity was observed metal to boron peak in $Mo_{0.9}Ni_{0.1}B_2$/ms electrocatalyst. This could lead to a thinner boron oxide layer at the surface compared to other samples (**Figure 37**). For the Ni 2p spectrum, the first doublet at 853.18 and 870.38 by corresponding to $2p_{3/2}$ and $2p_{1/2}$ encountered with the metallic nickel to boron binding at the literature. The second doublet at 855.97 and 874.28 eV were described as satellite peaks in here. Moreover, the O 1s spectrum was also examined and two different oxidation states of O were encountered at 530.58 and 532.08 eV. The first one may correspond to bonding between metal and oxygen and the second one is ascribed to hydroxyl groups or adsorbed water on the surface [18]. The trend was the same for all Ni substituted MoB_2 in terms of Mo, O and B. However, for the Ni 2p, the situation was different (**Figure 37**). There was

an additional doublet at the 855.88 and 873.58 eV by corresponding to Ni-O bonding with an increasing peak intensity toward *x*=0.2 and 0.3 Ni concentrations [32].

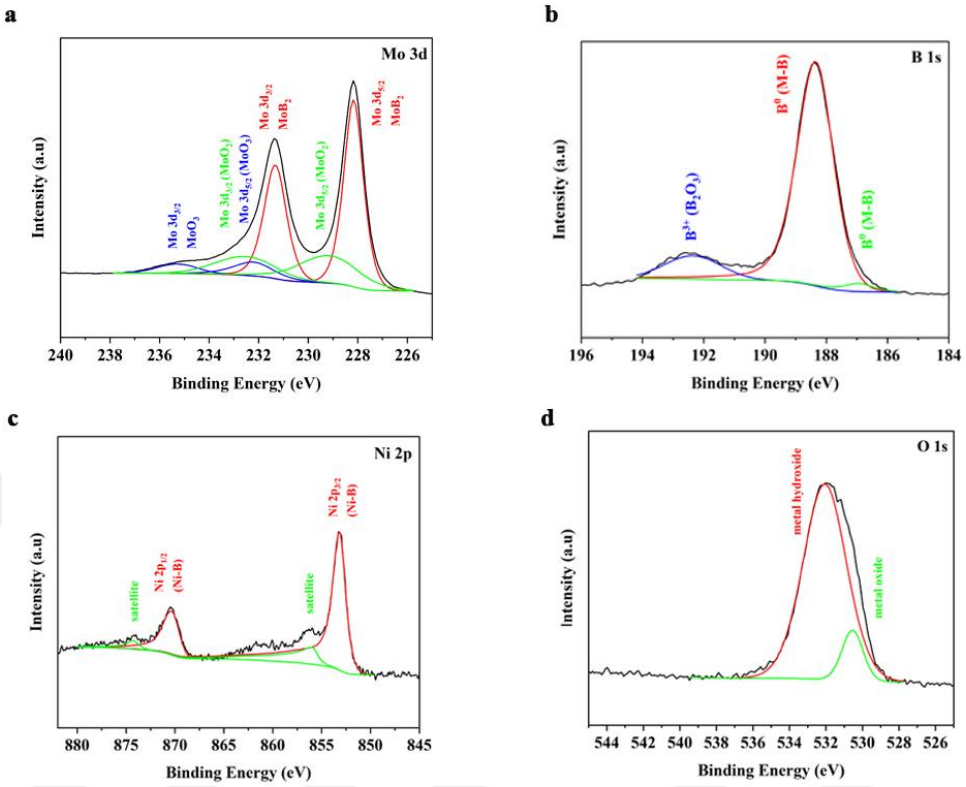

Figure 36. XPS analysis of $Mo_{0.9}Ni_{0.1}B_2$/ms electrocatalysts a) Mo 3d, b) B 1s, c) Ni 2p, and d) O 1s.

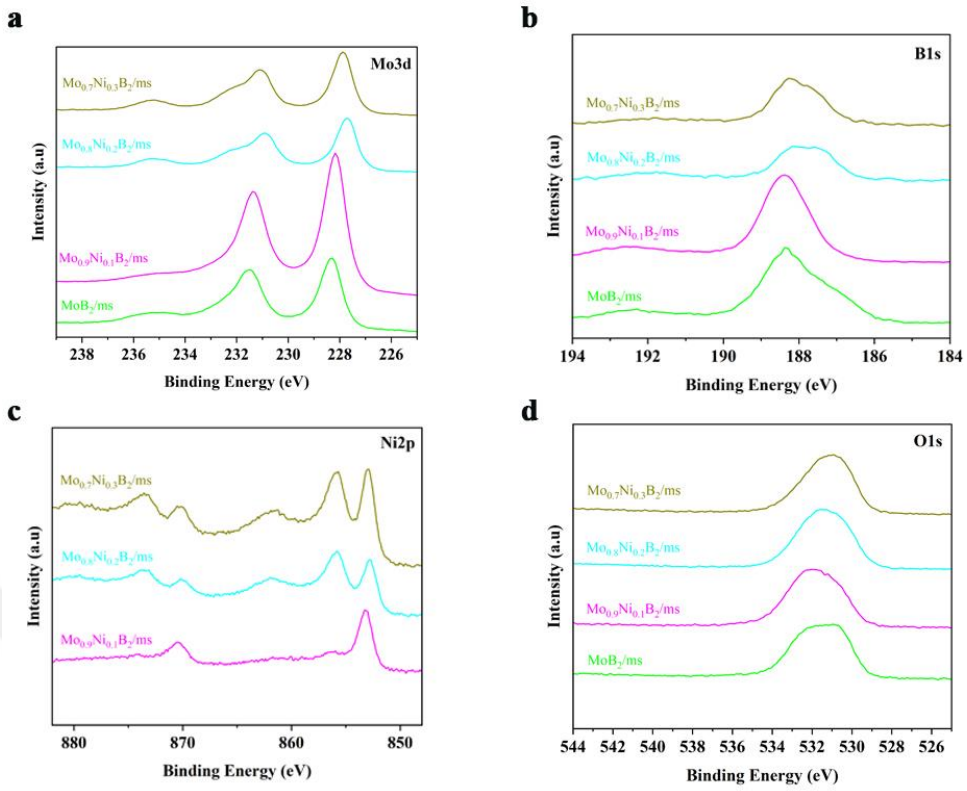

Figure 37. High-resolution XPS spectrum of a) Mo 3d, b) B 1s, c) Ni 2p, and d) O 1s for parent and Ni substituted MoB_2 synthesized by the molten salt method.

Similar to Ni-substituted MoB_2 electrocatalysts, XPS spectra of Mo 3d, B 1s, Co 2p, and O 1s for the Co-substituted catalysts **Figure 38**, and the results of Mo 3d, B 1s, O 1s ensured the same trend (**Figure 39**). There were two important doublets at 777.9 ($2p_{3/2}$), 792.78 ($2p_{1/2}$), 781.28 ($2p_{3/2}$), and 797.08 ($2p_{1/2}$) eV which corresponds to Co-B binding and oxidized cobalt [54] and there was an additional doublet at 786 and 803 eV correlated with satellite peaks.

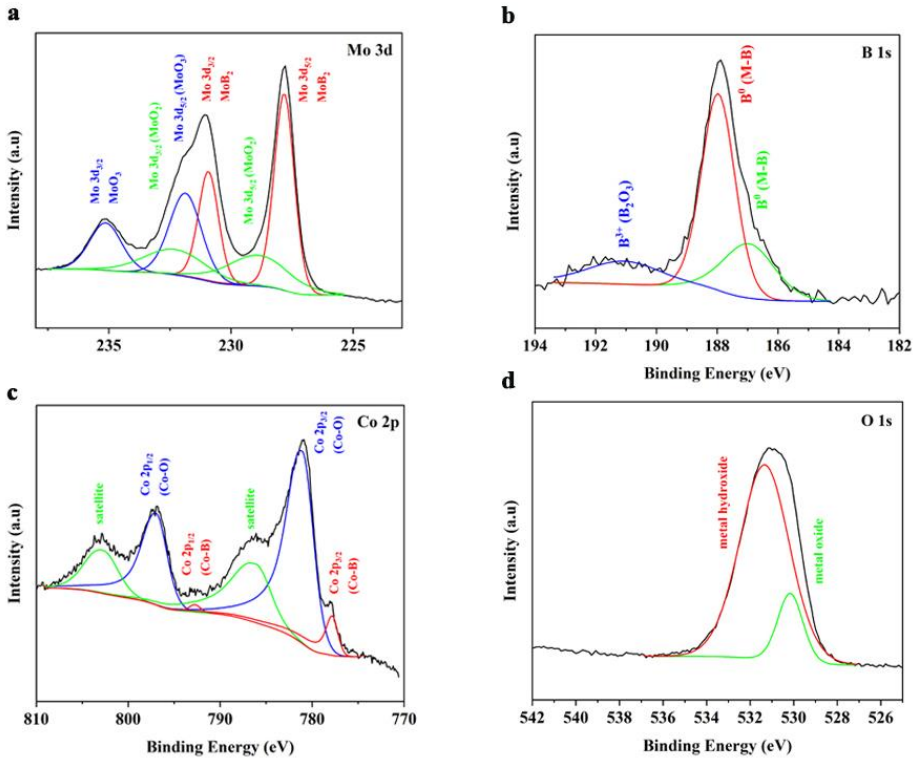

Figure 38. XPS analysis of $Mo_{0.8}Co_{0.2}B_2$/ms electrocatalysts a) Mo 3d, b) B 1s, c) Co 2p, and d) O 1s.

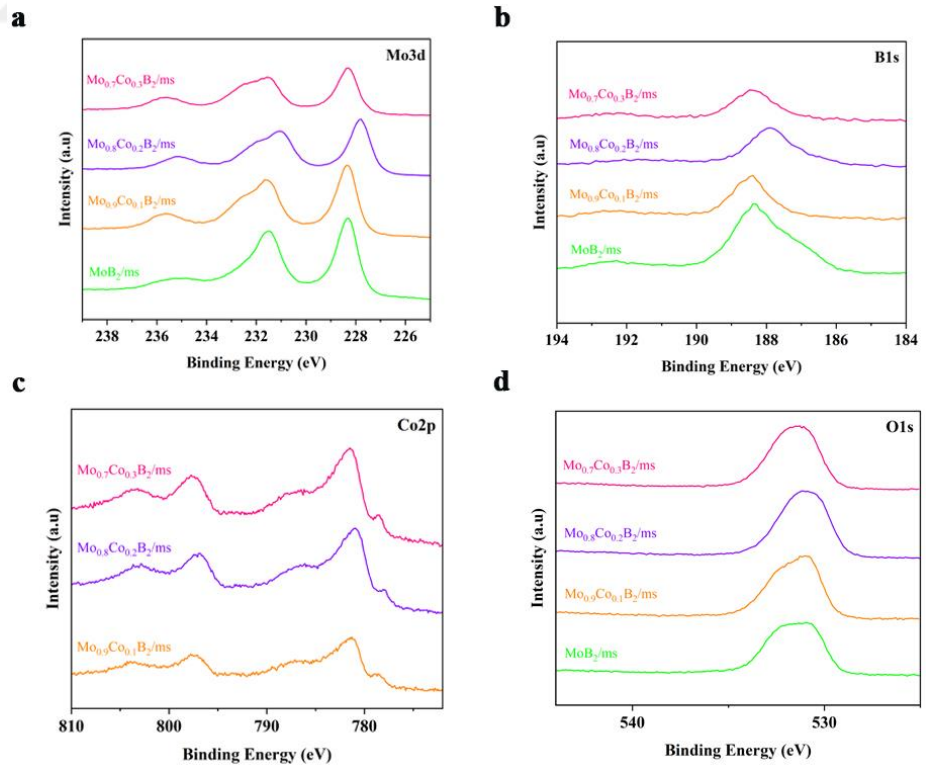

Figure 39. High-resolution XPS spectrum of a) Mo 3d, b) B 1s, c) Co 2p, and d) O 1s for parent and Co substituted MoB_2 synthesized by the molten salt method.

Transmission Electron Microscopy (TEM)

The crystalline structure of $Mo_{0.9}Ni_{0.1}B_2$/ms and $W_{0.8}Co_{0.2}B_2$/ms and their high-resolution morphology were further examined by HR-TEM (**Figure 40**), from which nanosized sub-grains below 10 nm can be manifested. The lattice fringes of $Mo_{0.9}Ni_{0.1}B_2$/ms could be represented as 0.260 nm lattice spacing while $Mo_{0.8}Co_{0.2}B_2$/ms with 0.258 nm lattice spacing can be visualized in **Figure 40(b-d)**. Since the represented lattice spacing were illustrated with higher intensity peaks for both, it can't say the direct crystalline group for our cases. But it may be fit (100) plane for $P6_3/mmm$, or (101) plane for R_3/mH [6], [69].

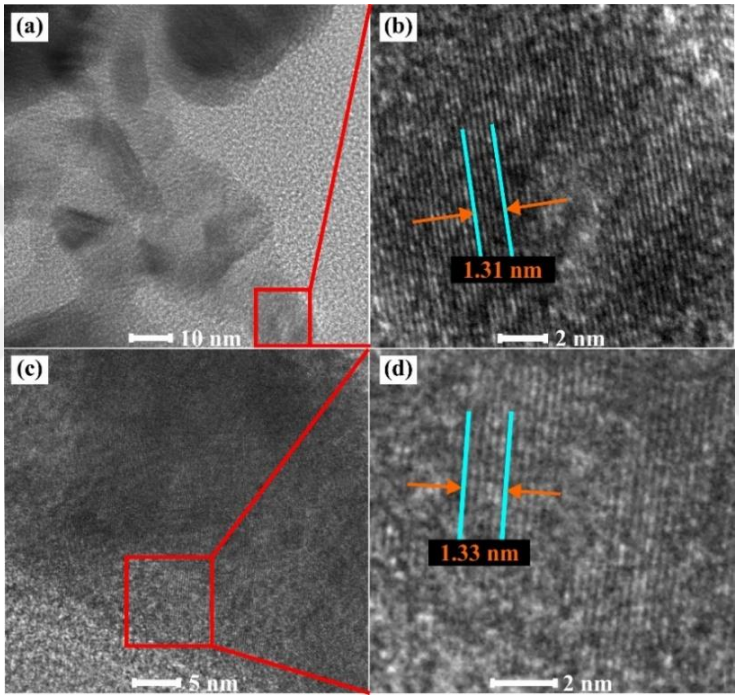

Figure 40. HRTEM images of (a) – (b) $Mo_{0.9}Ni_{0.1}B_2$, and (c) – (d) $Mo_{0.8}Co_{0.2}B_2$.

In **Figure 41**, selected area electron diffraction (SAED) showed the ring composed structure of $Mo_{0.9}Ni_{0.1}B_2$/ms and $Mo_{0.8}Co_{0.2}B_2$/ms by confirming the nanosphere shape and polycrystallinity [69].

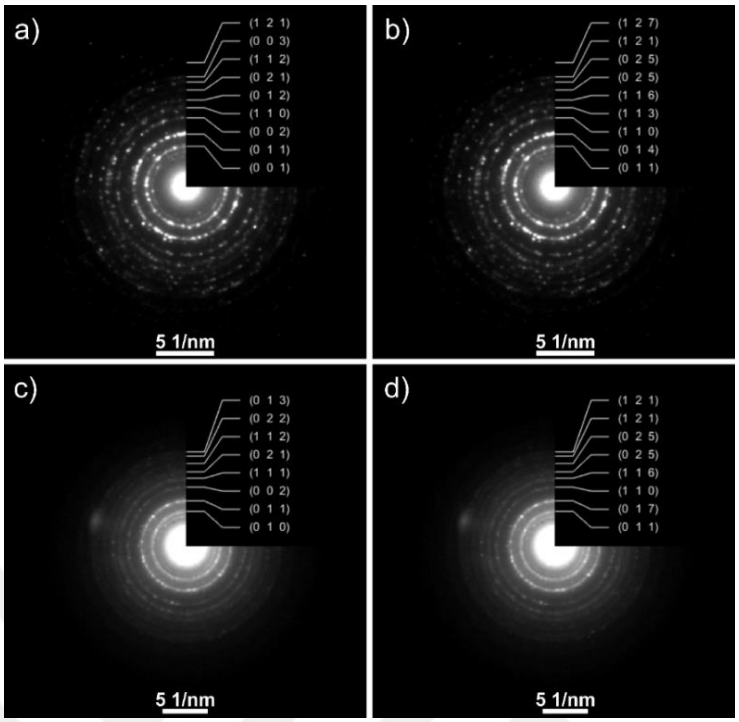

Figure 41. SAED images of (a) – (b) $Mo_{0.9}Ni_{0.1}B_2$/ms, and (c) – (d) $Mo_{0.8}Co_{0.2}B_2$/ms.

3.2.2 Electrochemical Characterization

Electrochemical measurements were conducted the same as discussed in Chapter 2.2.2. Only the potential range in the ECSA experiments was changed according to the OCP value and potential window which was 0.20 – 0.30 V (vs RHE).

Oxygen Evolution Behavior

MoB_2 electrocatalysts synthesized by two methods were investigated to obtain information about their electrochemical behavior. Firstly, OER performance of pristine and metal substituted MoB_2 were performed under 1 M KOH electrolyte medium with loading of 0.5 mg/cm^2 catalyst on the GC electrode. The results are presented in **Figure 42** by taking RuO_2 as the OER reference material to reliable comparison. The OER activity of GC has exhibited to indicate there is no impact due to GC on the performance of electrocatalysts. According to **Figure 42**, pristine MoB_2/ms couldn't afford 10 mA cm^{-2} to provide oxygen bubble formation from the electrode surface in the desired potential window which is 1 – 1.8 V. To obtain low overpotential from MoB_2 electrocatalysts, an efficient way is doping or substitution with another atom by changing the electronic structure of electrocatalysts as discussed earlier [58]. In this case, Co and Ni substitutions were put in the MoB_2 structure separately.

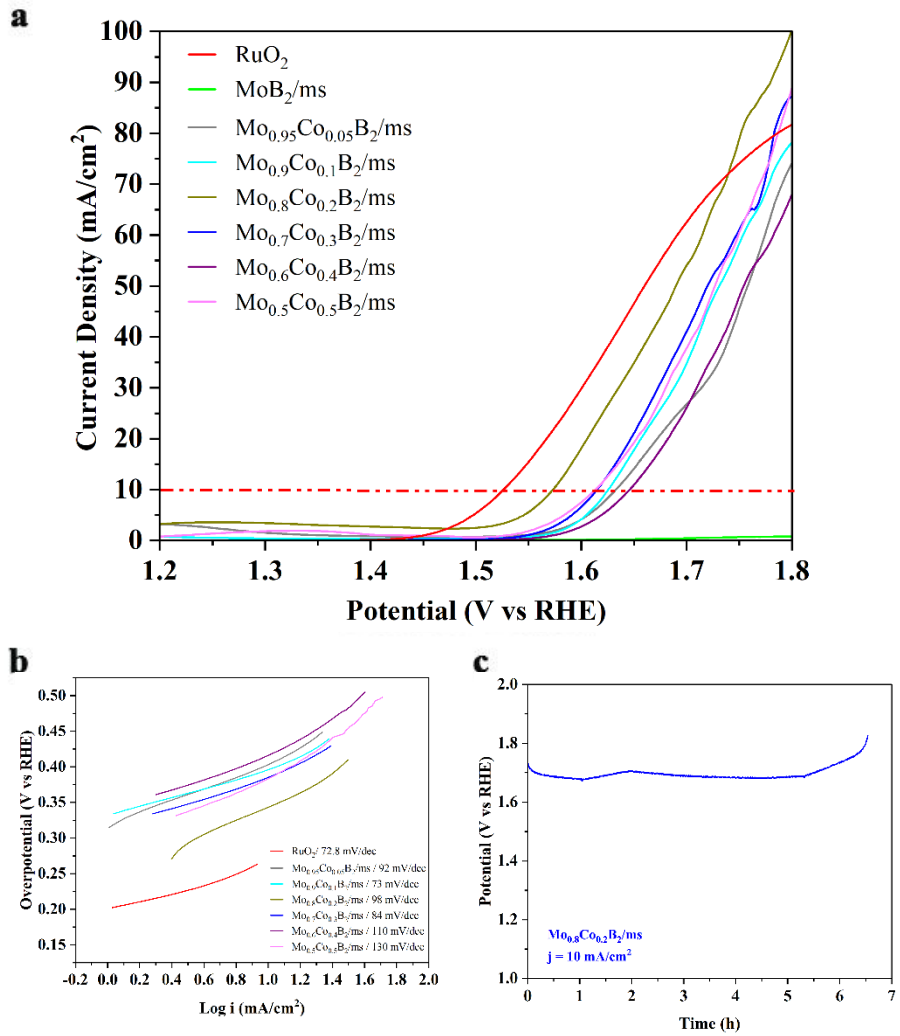

Figure 42. Electrochemical activity toward OER for the parent and metal-substituted MoB_2 synthesized by molten-salt (ms) method recorded in 1 M KOH at a scan rate of 5 mV s^{-1}. a) Polarization curves, b) Related Tafel plots, and c) Chronopotentiometric curve of $Mo_{0.8}Co_{0.2}B_2$/ms recorded at a current density of 10 mA cm^{-2}.

According to **Figure 42**, Co addition improved the OER performance pristine MoB_2 relatively well. However, the substitution of Ni into the structure didn't reach 10 mA cm^{-2}. The lowest overpotential and closest to RuO_2 (an overpotential of 290 mV) for $Mo_{(1-x)}TM_xB_2$ were obtained with x = 0.2 concentration of Co substitution with the 340 mV overpotential ($Mo_{0.8}Co_{0.2}B_2$/ms). In the literature, Gupta et al. reported a 320 mV overpotential with Co-Mo-B TMBs structure in an alkaline environment which our result is close to this value. Different Co substitution ratios were beneficial to reach 10 mA cm^{-2} ,too. Nonetheless, the required overpotentials were higher than the $Mo_{0.8}Co_{0.2}B_2$/ms which were between 380 and 410 mV. For Co substitution into samples synthesized via molten salt technique, there was an increasing trend towards $Mo_{0.8}Co_{0.2}B_2$/ms which was the best sample, then a reducing through the higher ratios.

On the other hand, the pristine MoB_2 synthesized via carbothermal reduction was closer to 10 mA cm^{-2} compared to MoB_2/ms but didn't reach to this specific value again (**Figure 43**). To get better OER performance, MoB_2/ct electrocatalyst was substituted with Co and Ni atoms. In contrast to molten salt technique, Ni-substituted $Mo_{(1-x)}TM_xB_2$ successfully formed oxygen gas bubbles approximately the same overpotential which was 430 mV. $Mo_{0.8}Co_{0.2}B_2$/ct satisfied the best OER performance between the $Mo_{(1-x)}TM_xB_2$/ct electrocatalyst by decreasing the overpotential to 370 mV. However, it was still relatively high compared to $Mo_{0.8}Co_{0.2}B_2$/ms sample. Additionally, $Mo_{0.95}Co_{0.05}B_2$/ct showed the same performance as the $Mo_{0.8}Co_{0.2}B_2$/ct in this method while $Mo_{0.9}Co_{0.1}B_2$/ct had the highest overpotential between the substituted $Mo_{(1-x)}TM_xB_2$/ct electrocatalysts. Unfortunately, these results didn't demonstrate any trend in the carbothermal reduction method.

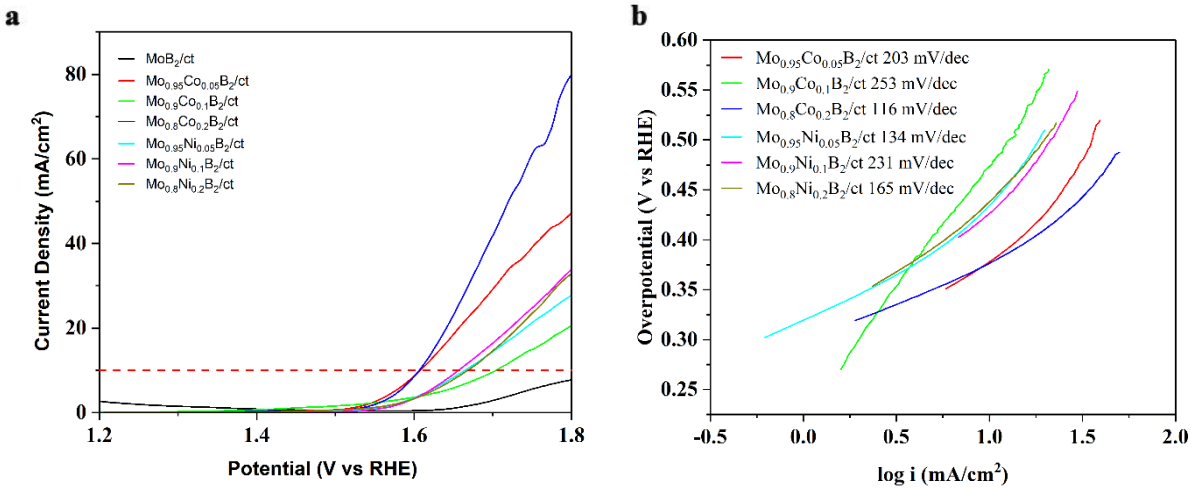

Figure 43. Electrochemical activity toward OER for the parent and metal-substituted MoB_2 synthesized by carbothermal (ct) reduction method recorded in 1 M KOH at a scan rate of 5 mV s^{-1}. a) Polarization curves, b) Related Tafel plots.

When the required overpotentials for OER were considered, Co-substituted MoB_2 were catalytically more active than the Ni-substituted MoB_2 for both synthesized techniques. In this case, the most important thing could be the crystal structure of electrocatalysts from two different methods thereby two different phase structure obtained from XRD results. According to these concerns, this information proved again that electrocatalytic performance of a sample with the same composition depends on the different factors including the crystal structure, phase morphology, particle size, thereby the surface-active sites, the electronic structure and binding with the substituted element for specific electrocatalysts [2].

As discussed earlier in the WB_2 part, boride structure may give chance easier oxidation for the metal atoms due to changing the native atomic geometry while the electron transfer is happening. So, for the first consideration in giving opportunity to better OER performance, CoOOH occurred with Co substitution could behave as active sites on the surface [55]. Also, when the metal is substituted to the pristine electrocatalyst, it could provide regulation in the electronic structure by tailoring the d-band center and prediction of intermediates with the oxygen containing on the electrode surface which is proven by DFT calculations as discussed again earlier [57]. Additional to the previous works of our group and WB_2 experimental studies, again the certain metal substitution ratio was dedicated as x = 0.2 for $Mo_{1-x}Co_xB_2$/ms and $Mo_{1-x}Co_xB_2$/ct in terms of OER performance by satisfying the optimum ratio to tailor d-band center. For the second consideration in two different phase structures, since samples via ct method have $Mo_2B_{4.026}$ crystalline structure **(Figure 27)**, they could have better binding between Ni-Mo-B elements, as in the discussed Ni-substituted MoB_2/ms XRD results (**Figure *26*)**, to gain OER catalytic activity compared to Ni-substituted $Mo_{(1-x)}TM_xB_2$. In the third factor between the comparison, discussed molten salt samples provides nano-sized structure to composition, more homogeneous morphology in terms of particle size and shape, a better (**Figure 29**), less impurity in terms of distorting the layered MoB_2 structure with Co substitution (**Figure *26***), thereby leading to higher electrochemically active surface area (discussed later) and utilizing higher OER activity.

To get information about the OER mechanism in a detail way, the Tafel plots for the OER were plotted as the required overpotential versus the current density. Since LSV curves provide analysis in terms of thermodynamic concerns, the Tafel slopes gives chance to obtain the OER kinetic. The pristine MoB_2 and metal-substituted MoB_2 via molten salt technique were given in **Figure 42.** According to this graph, $Mo_{0.8}Co_{0.2}B_2$/ms ensured the lowest Tafel slope (73 mV/dec) which approximately the same with commercial RuO_2 (72.8 mV/dec). This indicates that $Mo_{0.8}Co_{0.2}B_2$/ms has the fastest enlargement for the current density via overpotential and leads to facilitating the kinetics of OER mechanism. By comparing the LSV curves and Tafel slopes of these electrocatalyst, they have a balance between them as expected. The relevant Tafel slopes for the samples included in **Figure 21** are listed in **Table 5**.

Due to the lack of commercial RuO_2 in terms of stability and durability under the harsh conditions for the EWS, the long-run durability of the $Mo_{0.8}Co_{0.2}B_2$/ms was conducted at the current density of 10 mA cm^{-2} since it was the best electrocatalyst in terms of OER. Unfortunately, the durability could have endured until approximately 7 hours even it was tried four times to obtain 12 hours stability (**Figure 42**). The most important cause for that is the continuous coverage of the catalyst surface with the oxygen gas bubbles and leading to exfoliation and breakage of the catalyst coating from the electrode surface. Due to this exfoliation, the LSV curve after stability couldn't have done.

Hydrogen Evolution Reaction

Similar to oxygen evolution and investigation, 0.5 mg cm^{-2} of catalyst was loaded on the GC electrode to obtain information about HER performance. In this time, a negative potential window was performed under 1 M KOH medium and LSV curves of each electrocatalyst were obtained (**Figure 44**). For a reliable comparison, 10% Pt/C as a benchmark HER catalyst and GC electrode as a substrate were added to the curves. MoB_2/ms as a layered material showed 270 mV overpotential 10 mA cm^{-2} which was very close to commercial Pt/C material (198 mV overpotential) compared to pristine WB_2/ms and even $W_{0.8}Co_{0.2}B_2$/ms. To reduce this overpotential further and become closer to Pt/C, metal substitution was conducted again into the MoB_2 structure with Co and Ni atoms. By looking at the LSV curves of substituted samples (Figure EC-Y), $Mo_{0.9}Ni_{0.1}B_2$/ms electrocatalyst was the closest to Pt/C with a 220 mV overpotential by placed at the top among the HER catalysts in this work. $Mo_{0.7}Co_{0.3}B_2$/ms sample have followed the $Mo_{0.9}Ni_{0.1}B_2$/ms sample with the 260 mV of overpotential which was still lower than MoB_2/ms but without any significant change. For the other substitution amounts in the molten salt technique, overpotential values were very close to MoB_2/ms or even higher at x=0.2 concentration of Ni and Co.

For the carbothermal reduction, MoB_2/ct provided 350 mV overpotential at 10 mA cm^{-2} which was higher than the MoB_2/ms sample. The best sample for HER performance in this technique was the $Mo_{0.8}Co_{0.2}B_2$/ct with 320 mV overpotential by showing still higher values compared to molten salt method. For the other substitution ratios, the overpotential results have become even higher than the MoB_2/ct. Due to this reason, the substitution amounts were kept as x=0.2 and didn't continue higher values as MoB_2/ms

cases (see **Table 5)**. As a final addition, $Mo_{0.9}Ni_{0.1}B_2$/ct reached 10 mA cm^{-2} current density at the 410 mV which was higher than the $Mo_{0.9}Ni_{0.1}B_2$/ms (220 mV) significantly.

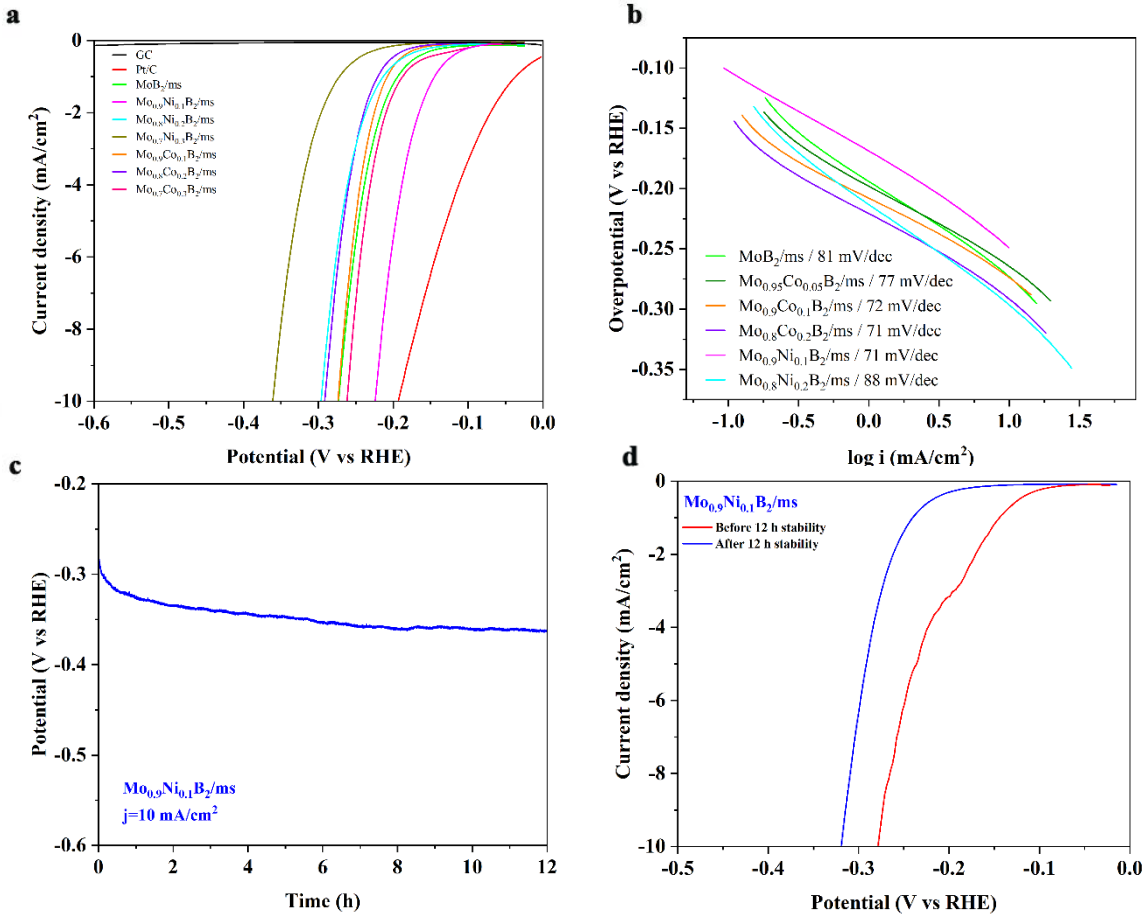

Figure 44. Electrochemical activity toward HER for the parent and metal-substituted MoB_2 synthesized by molten-salt (ms) method recorded in 1 M KOH at a scan rate of 5 mV s^{-1}. (a) Polarization curves, (b) Related Tafel plots, (c) Chronopotentiometric curve of $Mo_{0.9}Ni_{0.1}B_2$/ms recorded at a current density of 10 mA cm^{-2} and, (d) Polarization curves of best-performing $Mo_{0.9}Ni_{0.1}B_2$/ms initially and after 12 hours stability.

By considering their synthesis technique thereby crystal structure and HER performance of these samples, layered MoB_2 particles and substituted versions tends to provide better catalytic activity in terms of HER. Similar to OER performance of MoB_2 and discussion in WB_2 cases, HER catalytic activity of electrocatalyst depends on the d-band center of metals [60], [61]. In this situation, d-band center could have affected by Ni and Co substitution, their concentration, different synthesis techniques, changes in the phase morphology and modulation of electronic structure due to these differences[40], [62], [63]. $Mo_{0.9}Ni_{0.1}B_2$/ms have become comparable with the Jothi et.al. works of MoB_2 with 154 mV overpotential [69]. The most probable reason for this difference is that Jothi

et.al. was conducted their experiments under 0.5 M H_2SO_4 acidic environment while we conducted in 1 M KOH alkaline environment.

The related Tafel plots of MoB_2 were plotted in **Figure 44** as a current density versus overpotential. In this work, $Mo_{0.9}Ni_{0.1}B_2$/ms has the lowest Tafel slope which approximately identical to $Mo_{0.8}Co_{0.2}B_2$/ms and $Mo_{0.9}Co_{0.1}B_2$/ms. When the Tafel slopes of pristine MoB_2/ms and substituted MoB_2/ms samples were compared, the substitution of course changed the values but there was no significant change until the x=0.2 concentration of Ni. Additionally, nearly all the Tafel slopes in this **Figure 44** are smaller than the commercial Pt/C (85.2 mV dec^{-1}) by providing a higher growth in terms of current density versus overpotential and more favorable HER kinetics. This may indicate that the effects of substitution majorly change the intrinsic properties like their crystal structure and binding with substitution atom rather than the kinetics of reaction mechanism. The remaining polarization curves and Tafel slopes were represented in **Figure 45** by indicating higher overpotentials and higher Tafel slopes.

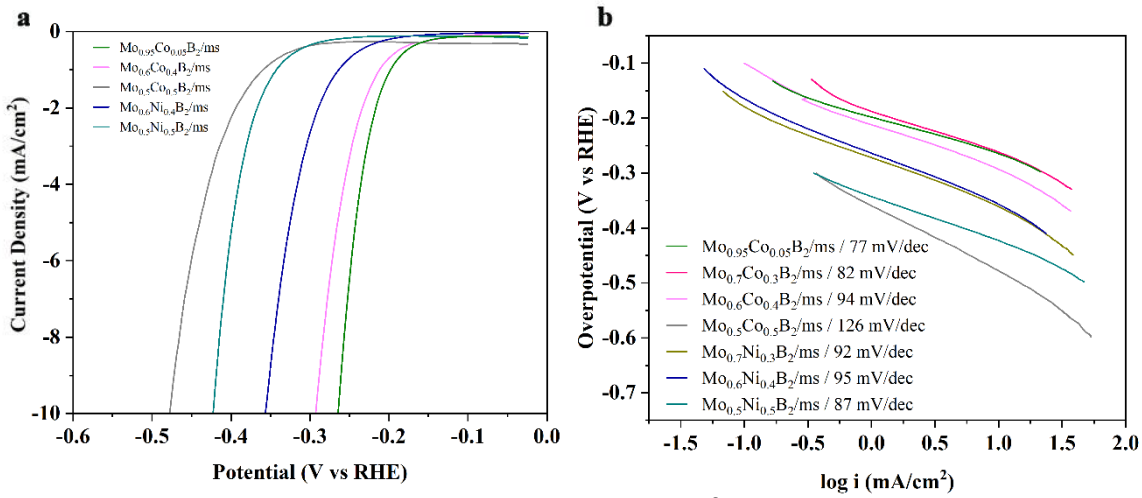

Figure 45. Electrochemical activity toward HER for the metal-substituted MoB_2 synthesized by molten-salt (ms) method recorded in 1 M KOH at a scan rate of 5 mV s^{-1}. (a) Polarization curves, (b) Related Tafel plots.

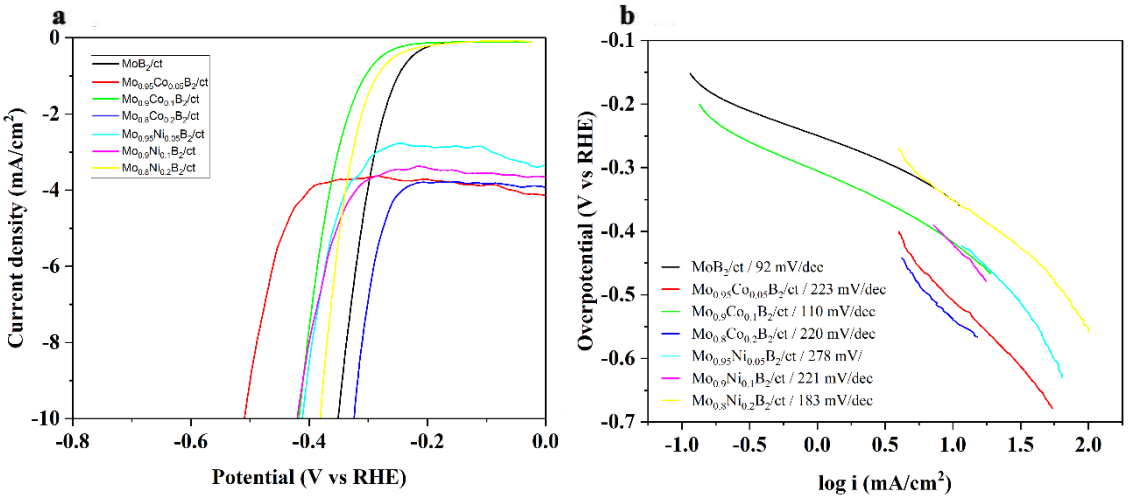

Figure 46. Electrochemical activity toward HER for the metal-substituted MoB_2 synthesized by molten-salt (ms) method recorded in 1 M KOH at a scan rate of 5 mV s^{-1}. (a) Polarization curves, (b) Related Tafel plots.

When the Tafel slopes of samples synthesized via carbothermal reduction were investigated, they have even higher than 200 mV/dec except MoB_2/ct (92 mV/dec), $Mo_{0.9}Co_{0.1}B_2$/ct (110 mV/dec), and $Mo_{0.8}Ni_{0.2}B_2$/ct (183 mV/dec). Again, this may lead to changes in the MoB_2 phase structure directly influence the kinetics of reaction mechanism as an important intrinsic property which shows less HER activity. Based on these results and equations (11) – (14), it has been evinced that the dominating path for hydrogen adsorption in the samples is through the Volmer mechanism. The related Tafel slopes of the different substituted concentrations (reported in **Figure 46)** are also listed in **Table 5**.

To examine HER stability, $Mo_{0.9}Ni_{0.1}B_2$/ms was conducted an experiment based on applying 10 mA cm^{-2} current density for 12 h (**Figure 44c**). Any exfoliation didn't encounter, and the sample kept its electrochemical property for straight forward. To obtain loss of feature, LSV experiments were performed before and after stability (**Figure 44d**). According to these results, the $Mo_{0.9}Ni_{0.1}B_2$/ms only lost 14 % of its overpotential (decreasing from 280 mV to 320 mV) which was very good compared to OER stability of $Mo_{0.8}Co_{0.2}B_2$/ms and HER stability of $W_{0.8}Co_{0.2}B_2$/ms in this work.

As an additional investigation of electrochemical evolution and features, exploiting electrochemical double-layer capacitance again was plotted to obtain electrochemically active surface areas of MoB_2 electrocatalysts and comparison of different synthesis techniques. A 0.1 V potential window was decided. **Figure 47** presents the ECSA plots

and relevant calculated C_{dl} for best samples in terms of LSV curves from OER and HER. Pristine MoB_2/ms has the lowest C_{dl} value (137 mF cm^{-2}) by looking at the molten salt-assisted electrocatalysts. When the substitution atom is entered the MoB_2/ms structure, directly influences the values such as 346 mF cm^{-2} for $Mo_{0.8}Ni_{0.2}B_2$/ms and 195 mF cm^{-2} for $Mo_{0.8}Co_{0.2}B_2$/ms. However, the most increasement in C_{dl} value was observed for $Mo_{0.9}Ni_{0.1}B_2$/ms electrocatalyst nearly four times higher (517 mF cm^{-2}). By considering all C_{dl} values that the substituted MoB_2 catalysts supply a higher surface-active area than the pristine one. Also, Ni addition contributes more activation on the surface rather than the Co substitution (**Figure 47a**). By looking at the EDS and XPS analysis of Ni substituted MoB_2 especially for the x=0.1 concentration, oxygen content in the particle was decreased by substituting the pristine structure.

Interestingly, when the electrocatalysts via carbothermal reduction were examined, pristine MoB_2/ct provided 486 mF cm^{-2} which was higher than the $Mo_{0.8}Co_{0.2}B_2$/ct (257 mF cm^{-2}) and $Mo_{0.8}Ni_{0.2}B_2$/ct (335 mF cm^{-2}) (**Figure 48a**). This reduction in the C_{dl} value could be explained via SEM analysis. From the **Figure 33, Figure 34, and Figure 35**, while MoB_2/ct has nearly nano-sized and spherical shape to contribute higher surface area, the shape and size of the Co and Ni substituted $Mo_{1-x}TM_xB_2$/ct completely changed by leading to coarse particles and rough morphology.

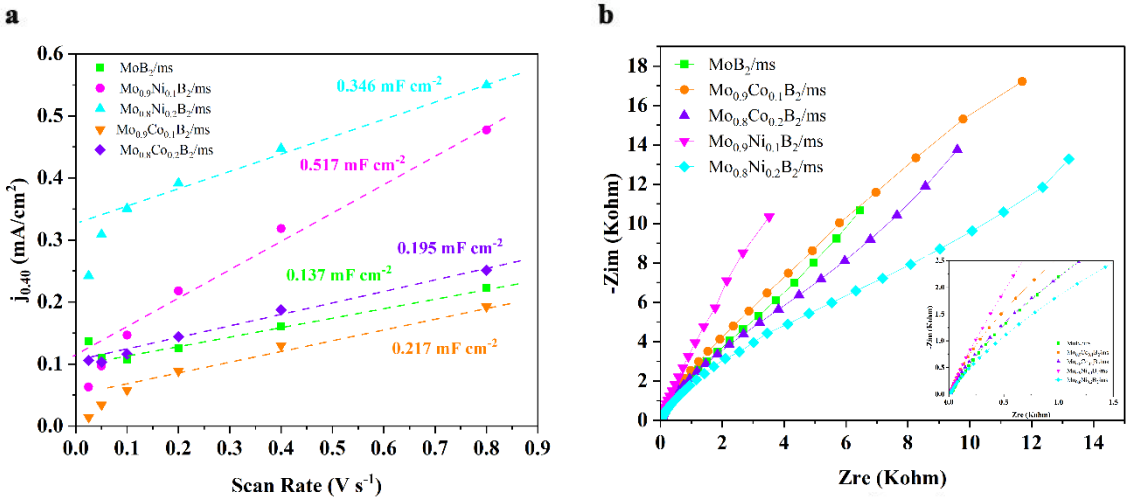

Figure 47. a) Capacitive currents from CV measurements plotted as a function of scan rate of parent and metal substituted MoB_2 synthesized by molten salt (ms) method, b) Representation of EIS data collected at 0 V.

EIS measurements were performed to understand behavior of MoB_2 electrocatalyst in this alkaline electrolyte (**Figure 47b and Figure 48b)**.

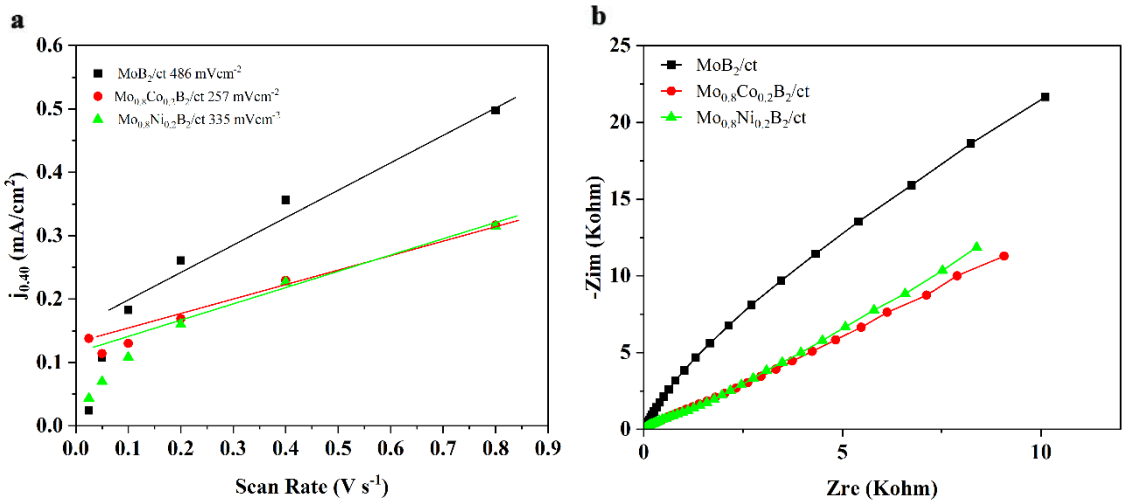

Figure 48. a) Capacitive currents from CV measurements plotted as a function of scan rate of parent and metal substituted MoB_2 synthesized by molten salt (ms) method, b) Representation of EIS data collected at 0 V.

Table 5. Summary of electrochemical parameters for all as-prepared samples

Sample	OER potential (mV)	OER Tafel slope (mV dec^{-1})	HER potential (mV)	HER Tafel slope (mV dec^{-1})
MoB_2/ms	-	-	270	81
$Mo_{0.95}Co_{0.05}B_2$/ms	400	92	265	77
$Mo_{0.9}Co_{0.1}B_2$/ms	395	73	275	72
$Mo_{0.8}Co_{0.2}B_2$/ms	**340**	**98**	290	71
$Mo_{0.7}Co_{0.3}B_2$/ms	385	84	265	82
$Mo_{0.6}Co_{0.4}B_2$/ms	415	110	290	94
$Mo_{0.5}Co_{0.5}B_2$/ms	385	130	475	126
$Mo_{0.95}Ni_{0.05}B_2$/ms	-	-	590	72
$Mo_{0.9}Ni_{0.1}B_2$/ms	**-**	**-**	**230**	**71**
$Mo_{0.8}Ni_{0.2}B_2$/ms	-	-	295	88
$Mo_{0.7}Ni_{0.3}B_2$/ms	-	-	360	92
$Mo_{0.6}Ni_{0.4}B_2$/ms	-	-	355	95
$Mo_{0.5}Ni_{0.5}B_2$/ms	-	-	425	87
MoB_2/ct	-	-	350	92
$Mo_{0.95}Co_{0.05}B_2$/ct	380	203	510	223
$Mo_{0.9}Co_{0.1}B_2$/ct	480	253	420	110
$Mo_{0.8}Co_{0.2}B_2$/ct	380	116	320	220
$Mo_{0.95}Ni_{0.05}B_2$/ct	440	134	415	278
$Mo_{0.9}Ni_{0.1}B_2$/ct	430	231	425	221
$Mo_{0.8}Ni_{0.2}B_2$/ct	440	165	385	183

To understand the alternations in the surface of electrocatalyst in terms of morphological and compositional after stability measurements, SEM and EDS analyses were performed. According to the **Figure 49**, the surface of $Mo_{0.9}Ni_{0.1}B_2$/ms didn't suffer any distinguishable change and deterioration after 12 h HER stability. This gives information about the high tolerance for the alkaline medium. Additionally, although it has been 12 h with the 10 mA cm^{-2} current density, there is still a homogeneous distribution of Ni at the related EDS elemental mappings.

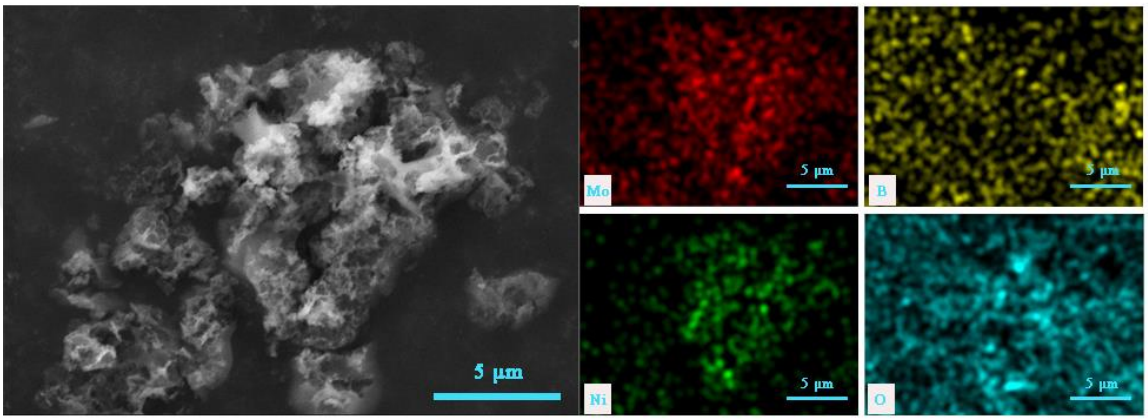

Figure 49. SEM images and related EDS elemental mapping analyses showing electrode surface morphology and structural elements of best performing $Mo_{0.9}Ni_{0.1}B_2$/ms after 12 h d) HER stability.

Chapter 4:**CONCLUSION**

In this thesis, the transition metal substitution effect (Ni and Co) into WB_2 and MoB_2 structures with various substitution amounts and the effect of synthesis technique on electrochemical performance were examined. Samples were synthesized via molten salt technique with the help of eutectic point in NaCl-KCl system, and carbothermal reduction technique via mechanical activation. XRD patterns of WB_2 for both ms-ct and MoB_2/ms were successfully obtained with theoretical diffraction peaks by having less intense secondary phases especially for the saturation limit. For the MoB_2/ct, a different phase formation was encountered with different crystal structure ($Mo_2B_{4.026}$). SEM with EDS analysis provided information about the successful and homogeneous distribution of transition metals into the metal diborides for ms technique. However, when the substitution metal was introduced into the metal diborides/ct, changes in the particle size and shape were encountered. XPS analysis proved the binding between Co 2p and Ni 2p with boron by replacing the W and Mo place in the structure. Electrochemical investigations were conducted for parent and substituted metal diborides with 0.5 mg cm^{-2} catalyst loadings on the glassy carbon electrode under the 1 M KOH alkaline environment. The commercial electrocatalyst were plotted to a sake comparison.

$W_{0.8}Co_{0.2}B_2$/ms showed the best performing bifunctional feature in HER and OER among the substituted WB_2 electrocatalysts for both synthesis techniques. For OER, $W_{0.8}Co_{0.2}B_2$/ms displayed 113.6 mV/dec Tafel slope while 93.2 mV/dec for HER. The remaining WB_2 electrocatalysts provided higher Tafel slopes which related to the slower kinetics. $W_{0.8}Co_{0.2}B_2$/ms ensured 340 mV and 360 mV overpotentials for OER and HER, respectively. These values were significantly higher than the pristine WB_2 electrocatalysts that was discussed in this thesis. For HER, the closest one was the $W_{0.8}Co_{0.2}B_2$/ct with the 373 mV overpotential. The second electrocatalysts was the $W_{0.9}Co_{0.1}B_2$/ct by providing 370 mV OER overpotential. The findings revealed that x=0.2 concentration was the best for HER in terms of Co substitution. According to the C_{dl} values, $W_{0.8}Co_{0.2}B_2$/ms was nearly higher twice than the WB_2/ms and $W_{0.8}Co_{0.2}B_2$/ct. By comparing the Co and Ni, Ni was less active than the Co for the WB_2 samples. $W_{0.8}Co_{0.2}B_2$/ms was conducted to 12 h stability with 22 % performance loss.

Among the MoB_2 samples, $Mo_{0.8}Co_{0.2}B_2$/ms showed the best OER performance with the 340 mV overpotential relatively higher than the others and by having 98 mV/dec of

Tafel slope. Ni-substituted MoB_2/ms electrocatalysts couldn't have reached 10 mA cm^{-2} current density for OER while Ni-substituted MoB_2/ct have intermediate OER performance (420 mV). In the case of HER, $Mo_{0.9}Ni_{0.1}B_2$/ms provided remarkable activity by reaching 10 mA cm^{-2} current density via 220 mV overpotential which was very close to Pt/C (198 mV). Also, it has 71 mV/dec of Tafel slope which was smaller than the Pt/C (85.2 mV/dec). Pristine MoB_2 and $Mo_{0.9}Ni_{0.1}B_2$/ms have the C_{dl} values of 137 mV/dec and 517 mV/dec, respectively which brings the important of substitution into the structure as providing the more available active sites for HER. Again, for OER, the best performance was obtained from x=0.2 concentration, while x_{Ni}=0.1 was the superior one in HER. $Mo_{0.9}Ni_{0.1}B_2$/ms showed remarkable stability for 12 h in HER by loosing just 14 % of its feature.

The important outcome in MoB_2 cases is that when the layered structure of metal diborides evolved to another phase structure, it loses its HER catalytic activity even though substituted with Ni and Co. According to OER performances for two different metal diborides, the presence of Co-containing species on the surface tailors the binding energy of oxygen intermediates during the OER mechanism and leads to increase in catalytic activity towards OER.

In conclusion, designing and synthesizing alternative transition metal diborides electrocatalysts in this thesis study have demonstrated their considerable catalytic activities for electrochemical water splitting applications. These valuable results give opportunity to further enhancement of the electrocatalytic performances of metal diborides and leading to bifunctional property.

BIBLIOGRAPHY

[1] D. J. Lockwood, A. Lavacchi, H. Miller, and F. Vizza, “Nanotechnology in Electrocatalysis for Energy.” [Online]. Available: http://www.springer.com/series/6331

[2] X. Li *et al.*, “Water Splitting: From Electrode to Green Energy System,” *Nano-Micro Letters*, vol. 12, no. 1. Springer, Jun. 01, 2020. doi: 10.1007/s40820-020-00469-3.

[3] S. Anantharaj, S. R. Ede, K. Sakthikumar, K. Karthick, S. Mishra, and S. Kundu, “Recent Trends and Perspectives in Electrochemical Water Splitting with an Emphasis on Sulfide, Selenide, and Phosphide Catalysts of Fe, Co, and Ni: A Review,” *ACS Catalysis*, vol. 6, no. 12. American Chemical Society, pp. 8069–8097, Dec. 02, 2016. doi: 10.1021/acscatal.6b02479.

[4] H. Chen and X. Zou, “Intermetallic borides: Structures, synthesis and applications in electrocatalysis,” *Inorganic Chemistry Frontiers*, vol. 7, no. 11. Royal Society of Chemistry, pp. 2248–2264, Jun. 07, 2020. doi: 10.1039/d0qi00146e.

[5] D. Zhu, L. Wang, M. Qiao, and J. Liu, “Phosphate ion functionalized CoP nanowire arrays for efficient alkaline hydrogen evolution,” *Chemical Communications*, vol. 56, no. 52, pp. 7159–7162, Jul. 2020, doi: 10.1039/d0cc02246b.

[6] H. Park, Y. Zhang, E. Lee, P. Shankhari, and B. P. T. Fokwa, “High-Current-Density HER Electrocatalysts: Graphene-like Boron Layer and Tungsten as Key Ingredients in Metal Diborides,” *ChemSusChem*, vol. 12, no. 16, pp. 3726–3731, Aug. 2019, doi: 10.1002/cssc.201901301.

[7] Q. Hu *et al.*, “Nonmetal Doping as a Robust Route for Boosting the Hydrogen Evolution of Metal-Based Electrocatalysts,” *Chemistry - A European Journal*, vol. 26, no. 18. John Wiley and Sons Inc, pp. 3930–3942, Mar. 26, 2020. doi: 10.1002/chem.201902998.

[8] V. R. Stamenkovic, D. Strmcnik, P. P. Lopes, and N. M. Markovic, “Energy and fuels from electrochemical interfaces,” *Nature Materials*, vol. 16, no. 1. Nature Publishing Group, pp. 57–69, Dec. 20, 2016. doi: 10.1038/nmat4738.

[9] K. Zeng and D. Zhang, “Recent progress in alkaline water electrolysis for hydrogen production and applications,” *Progress in Energy and Combustion Science*, vol. 36, no. 3. pp. 307–326, Jun. 2010. doi: 10.1016/j.pecs.2009.11.002.

[10] S. Zhang, X. Zhang, Y. Rui, R. Wang, and X. Li, “Recent advances in non-precious metal electrocatalysts for pH-universal hydrogen evolution reaction,” *Green Energy and Environment*, vol. 6, no. 4. KeAi Publishing Communications Ltd., pp. 458–478, Aug. 01, 2021. doi: 10.1016/j.gee.2020.10.013.

[11] M. Zeng and Y. Li, “Recent advances in heterogeneous electrocatalysts for the hydrogen evolution reaction,” *Journal of Materials Chemistry A*, vol. 3, no. 29. Royal Society of Chemistry, pp. 14942–14962, Jun. 01, 2015. doi: 10.1039/c5ta02974k.

[12] B. You and Y. Sun, “Innovative Strategies for Electrocatalytic Water Splitting,” *Accounts of Chemical Research*, vol. 51, no. 7, pp. 1571–1580, Jul. 2018, doi: 10.1021/acs.accounts.8b00002.

[13] W. Han, M. Li, Y. Ma, and J. Yang, “Cobalt-Based Metal-Organic Frameworks and Their Derivatives for Hydrogen Evolution Reaction,” *Frontiers in Chemistry*, vol. 8. Frontiers Media S.A., Nov. 20, 2020. doi: 10.3389/fchem.2020.592915.

[14] V. Mazánek, H. Nahdi, J. Luxa, Z. Sofer, and M. Pumera, “Electrochemistry of layered metal diborides,” *Nanoscale*, vol. 10, no. 24, pp. 11544–11552, Jun. 2018, doi: 10.1039/c8nr02142b.

[15] Z. Chen, X. Duan, W. Wei, S. Wang, Z. Zhang, and B. J. Ni, “Boride-based electrocatalysts: Emerging candidates for water splitting,” *Nano Research*, vol. 13, no. 2. Tsinghua University Press, pp. 293–314, Feb. 01, 2020. doi: 10.1007/s12274-020-2618-y.

[16] S. Gupta *et al.*, “Co-Ni-B nanocatalyst for efficient hydrogen evolution reaction in wide pH range,” *Applied Catalysis B: Environmental*, vol. 192, pp. 126–133, Sep. 2016, doi: 10.1016/j.apcatb.2016.03.032.

[17] O. Schmidt, A. Gambhir, I. Staffell, A. Hawkes, J. Nelson, and S. Few, “Future cost and performance of water electrolysis: An expert elicitation study,” *International Journal of Hydrogen Energy*, vol. 42, no. 52, pp. 30470–30492, Dec. 2017, doi: 10.1016/j.ijhydene.2017.10.045.

[18] A. N. Colli, H. H. Girault, and A. Battistel, “Non-precious electrodes for practical alkaline water electrolysis,” *Materials*, vol. 12, no. 8, 2019, doi: 10.3390/ma12081336.

[19] Q. Li, X. Zou, X. Ai, H. Chen, L. Sun, and X. Zou, “Revealing Activity Trends of Metal Diborides Toward pH-Universal Hydrogen Evolution Electrocatalysts with Pt-Like Activity,” *Advanced Energy Materials*, vol. 9, no. 5, Feb. 2019, doi: 10.1002/aenm.201803369.

[20] S. Gupta, M. K. Patel, A. Miotello, and N. Patel, “Metal Boride-Based Catalysts for Electrochemical Water-Splitting: A Review,” *Advanced Functional Materials*, vol. 30, no. 1. Wiley-VCH Verlag, Jan. 01, 2020. doi: 10.1002/adfm.201906481.

[21] M. Tahir *et al.*, “Electrocatalytic oxygen evolution reaction for energy conversion and storage: A comprehensive review,” *Nano Energy*, vol. 37. Elsevier Ltd, pp. 136–157, Jul. 01, 2017. doi: 10.1016/j.nanoen.2017.05.022.

[22] S. Gupta *et al.*, “Cobalt-Boride Nanostructured Thin Films with High Performance and Stability for Alkaline Water Oxidation,” *ACS Sustainable Chemistry and Engineering*, vol. 7, no. 19, pp. 16651–16658, Oct. 2019, doi: 10.1021/acssuschemeng.9b03995.

[23] S. Carenco, D. Portehault, C. Boissière, N. Mézailles, and C. Sanchez, “Nanoscaled metal borides and phosphides: Recent developments and perspectives,” *Chemical Reviews*, vol. 113, no. 10. American Chemical Society, pp. 7981–8065, Oct. 09, 2013. doi: 10.1021/cr400020d.

[24] R. K. Shervedani and A. Lasia, “Study of the Hydrogen Evolution Reaction on Ni-Mo-P Electrodes in Alkaline Solutions.”

[25] H. Vrubel and X. Hu, “Molybdenum boride and carbide catalyze hydrogen evolution in both acidic and basic solutions,” *Angewandte Chemie - International Edition*, vol. 51, no. 51, pp. 12703–12706, Dec. 2012, doi: 10.1002/anie.201207111.

[26] H. Y. Chung, M. B. Weinberger, J. M. Yang, S. H. Tolbert, and R. B. Kaner, “Correlation between hardness and elastic moduli of the ultraincompressible transition metal diborides RuB#!2, OsB2, and ReB2,” *Applied Physics Letters*, vol. 92, no. 26, 2008, doi: 10.1063/1.2946665.

[27] F. Guo *et al.*, “A class of metal diboride electrocatalysts synthesized by a molten salt-assisted reaction for the hydrogen evolution reaction,” *Chemical Communications*, vol. 55, no. 59, pp. 8627–8630, 2019, doi: 10.1039/c9cc03638e.

[28] N. Du, C. Wang, X. Wang, Y. Lin, J. Jiang, and Y. Xiong, “Trimetallic TriStar Nanostructures: Tuning Electronic and Surface Structures for Enhanced Electrocatalytic Hydrogen Evolution,” *Advanced Materials*, vol. 28, no. 10, pp. 2077–2084, Mar. 2016, doi: 10.1002/adma.201504785.

[29] Q. Li, X. Zou, X. Ai, H. Chen, L. Sun, and X. Zou, “Revealing Activity Trends of Metal Diborides Toward pH-Universal Hydrogen Evolution Electrocatalysts with Pt-Like Activity,” *Advanced Energy Materials*, vol. 9, no. 5, Feb. 2019, doi: 10.1002/aenm.201803369.

[30] M. Jin *et al.*, “Iron covalent doping in WB2to boost its hydrogen evolution activity,” *Inorganic Chemistry Frontiers*, vol. 9, no. 3, pp. 524–530, Feb. 2022, doi: 10.1039/d1qi01419f.

[31] T. Feng *et al.*, “Morphological and Interfacial Engineering of Cobalt-Based Electrocatalysts by Carbon Dots for Enhanced Water Splitting,” *ACS Sustainable Chemistry and Engineering*, vol. 7, no. 7, pp. 7047–7057, Apr. 2019, doi: 10.1021/acssuschemeng.8b06832.

[32] N. S. Peighambardoust, E. Sadeghi, B. Mete, M. Baris Yagci, and U. Aydemir, “Evaluating electrocatalytic activity of metal-substituted hafnium diboride (Hf1-xTMxB2; TM = Ni and Co) toward water splitting,” *Journal of Alloys and Compounds*, vol. 905, Apr. 2022, doi: 10.1016/j.jallcom.2022.164148.

[33] H. Li *et al.*, “Earth-Abundant Iron Diboride (FeB2) Nanoparticles as Highly Active Bifunctional Electrocatalysts for Overall Water Splitting,” *Advanced Energy Materials*, vol. 7, no. 17, Sep. 2017, doi: 10.1002/aenm.201700513.

[34] N. K. Chaudhari, H. Jin, B. Kim, and K. Lee, “Nanostructured materials on 3D nickel foam as electrocatalysts for water splitting,” *Nanoscale*, vol. 9, no. 34. Royal Society of Chemistry, pp. 12231–12247, Sep. 14, 2017. doi: 10.1039/c7nr04187j.

[35] D. Merki, S. Fierro, H. Vrubel, and X. Hu, “Amorphous molybdenum sulfide films as catalysts for electrochemical hydrogen production in water,” *Chemical Science*, vol. 2, no. 7, pp. 1262–1267, Jul. 2011, doi: 10.1039/c1sc00117e.

[36] Z. Wu, D. Nie, M. Song, T. Jiao, G. Fu, and X. Liu, “Facile synthesis of Co-Fe-B-P nanochains as an efficient bifunctional electrocatalyst for overall water-

splitting," *Nanoscale*, vol. 11, no. 15, pp. 7506–7512, Apr. 2019, doi: 10.1039/c9nr01794a.

[37] Y. Jiang and Y. Lu, "Designing transition-metal-boride-based electrocatalysts for applications in electrochemical water splitting," *Nanoscale*, vol. 12, no. 17. Royal Society of Chemistry, pp. 9327–9351, May 07, 2020. doi: 10.1039/d0nr01279c.

[38] W.-J. Jiang *et al.*, " Crystallinity-Modulated Electrocatalytic Activity of a Nickel(II) Borate Thin Layer on Ni 3 B for Efficient Water Oxidation ," *Angewandte Chemie*, vol. 129, no. 23, pp. 6672–6677, Jun. 2017, doi: 10.1002/ange.201703183.

[39] G. X. Cao, N. Xu, Z. J. Chen, Q. Kang, H. bin Dai, and P. Wang, "Cobalt-Tungsten-Boron as an Active Electrocatalyst for Water Electrolysis," *ChemistrySelect*, vol. 2, no. 21, pp. 6187–6193, Jul. 2017, doi: 10.1002/slct.201701459.

[40] H. Park, A. Encinas, J. P. Scheifers, Y. Zhang, and B. P. T. Fokwa, "Boron-Dependency of Molybdenum Boride Electrocatalysts for the Hydrogen Evolution Reaction," *Angewandte Chemie - International Edition*, vol. 56, no. 20, pp. 5575–5578, May 2017, doi: 10.1002/anie.201611756.

[41] P. Zhang, M. Wang, Y. Yang, T. Yao, H. Han, and L. Sun, "Electroless plated Ni-Bx films as highly active electrocatalysts for hydrogen production from water over a wide pH range," *Nano Energy*, vol. 19, pp. 98–107, Jan. 2016, doi: 10.1016/j.nanoen.2015.11.020.

[42] C. C. L. McCrory, S. Jung, J. C. Peters, and T. F. Jaramillo, "Benchmarking heterogeneous electrocatalysts for the oxygen evolution reaction," *J Am Chem Soc*, vol. 135, no. 45, pp. 16977–16987, Nov. 2013, doi: 10.1021/ja407115p.

[43] M. Broström, S. Enestam, R. Backman, and K. Mäkelä, "Condensation in the KCl-NaCl system," in *Fuel Processing Technology*, Jan. 2013, vol. 105, pp. 142–148. doi: 10.1016/j.fuproc.2011.08.006.

[44] S. P. Ong, L. Wang, B. Kang, and G. Ceder, "Li - Fe - P - O2 phase diagram from first principles calculations," *Chemistry of Materials*, vol. 20, no. 5, pp. 1798–1807, Mar. 2008, doi: 10.1021/cm702327g.

[45] Y. Long, Z. Wu, X. Zheng, H. T. Lin, and F. Zhang, "Mechanochemical synthesis and annealing of tungsten di- and tetra-boride," *Journal of the American Ceramic Society*, vol. 103, no. 2, pp. 831–838, Feb. 2020, doi: 10.1111/jace.16788.

[46] C. Wang *et al.*, “WB2: Not a superhard material for strong polarization character of interlayer W-B bonding,” *Physical Chemistry Chemical Physics*, vol. 19, no. 13, pp. 8919–8924, 2017, doi: 10.1039/c6cp04287b.

[47] T. Dash and B. B. Nayak, “Preparation of multi-phase composite of tungsten carbide, tungsten boride and carbon by arc plasma melting: characterization of melt-cast product,” *Ceramics International*, vol. 42, no. 1, pp. 445–459, 2016, doi: 10.1016/j.ceramint.2015.08.129.

[48] Z. Wu, Y. Long, H. T. Lin, and F. Zhang, “Effect of tantalum on phase transition and thermal stability of metastable tungsten tetra-boride,” *Ceramics International*, vol. 46, no. 11, pp. 17217–17223, Aug. 2020, doi: 10.1016/j.ceramint.2020.03.294.

[49] G. Hai, X. Jia, K. Zhang, X. Liu, Z. Wu, and G. Wang, “High-performance oxygen evolution catalyst using two-dimensional ultrathin metal-organic frameworks nanosheets,” *Nano Energy*, vol. 44, pp. 345–352, Feb. 2018, doi: 10.1016/j.nanoen.2017.11.071.

[50] J. Masa *et al.*, “Amorphous Cobalt Boride (Co 2 B) as a Highly Efficient Nonprecious Catalyst for Electrochemical Water Splitting: Oxygen and Hydrogen Evolution,” *Advanced Energy Materials*, vol. 6, no. 6, Mar. 2016, doi: 10.1002/aenm.201502313.

[51] E. Sadeghi, N. S. Peighambardoust, and U. Aydemir, “Tailoring the Morphology of Cost-Effective Vanadium Diboride through Cobalt Substitution for Highly Efficient Alkaline Water Oxidation,” *Inorganic Chemistry*, vol. 60, no. 24, pp. 19457–19466, Dec. 2021, doi: 10.1021/acs.inorgchem.1c03374.

[52] Q. Li *et al.*, “Multiple crystal phases of intermetallic tungsten borides and phase-dependent electrocatalytic property for hydrogen evolution,” *Chemical Communications*, vol. 56, no. 90, pp. 13983–13986, Nov. 2020, doi: 10.1039/d0cc06072k.

[53] J. Wu *et al.*, “Controllable Heteroatom Doping Effects of Cr xCo2-xP Nanoparticles: A Robust Electrocatalyst for Overall Water Splitting in Alkaline Solutions,” *ACS Applied Materials and Interfaces*, vol. 12, no. 42, pp. 47397–47407, Oct. 2020, doi: 10.1021/acsami.0c10441.

[54] S. Gupta, N. Patel, R. Fernandes, S. Hanchate, A. Miotello, and D. C. Kothari, “Co-Mo-B Nanoparticles as a non-precious and efficient Bifunctional

Electrocatalyst for Hydrogen and Oxygen Evolution," *Electrochimica Acta*, vol. 232, pp. 64–71, Apr. 2017, doi: 10.1016/j.electacta.2017.02.100.

[55] X. Ma *et al.*, "Crystal CoxB (x = 1-3) Synthesized by a Ball-Milling Method as High-Performance Electrocatalysts for the Oxygen Evolution Reaction," *ACS Sustainable Chemistry and Engineering*, vol. 5, no. 11, pp. 10266–10274, Nov. 2017, doi: 10.1021/acssuschemeng.7b02281.

[56] H. Ang *et al.*, "Hydrophilic Nitrogen and Sulfur Co-doped Molybdenum Carbide Nanosheets for Electrochemical Hydrogen Evolution," *Small*, vol. 11, no. 47, pp. 6278–6284, Dec. 2015, doi: 10.1002/smll.201502106.

[57] F. Calle-Vallejo, J. I. Martínez, and J. Rossmeisl, "Density functional studies of functionalized graphitic materials with late transition metals for oxygen reduction reactions," *Physical Chemistry Chemical Physics*, vol. 13, no. 34, pp. 15639–15643, Sep. 2011, doi: 10.1039/c1cp21228a.

[58] S. Sun, X. Zhou, B. Cong, W. Hong, and G. Chen, "Tailoring the d-Band Centers Endows (NixFe1- x)2P Nanosheets with Efficient Oxygen Evolution Catalysis," *ACS Catalysis*, vol. 10, no. 16, pp. 9086–9097, Aug. 2020, doi: 10.1021/acscatal.0c01273.

[59] B. Mete, N. S. Peighambardoust, S. Aydin, E. Sadeghi, and U. Aydemir, "Metal-substituted zirconium diboride (Zr1-xTMxB2; TM = Ni, Co, and Fe) as low-cost and high-performance bifunctional electrocatalyst for water splitting," *Electrochimica Acta*, vol. 389, Sep. 2021, doi: 10.1016/j.electacta.2021.138789.

[60] X. Zou, L. Wang, X. Ai, H. Chen, and X. Zou, "Crystal phase-dependent electrocatalytic hydrogen evolution performance of ruthenium-boron intermetallics," *Chemical Communications*, vol. 56, no. 20, pp. 3061–3064, Mar. 2020, doi: 10.1039/d0cc00070a.

[61] X. Ai *et al.*, "Transition-Metal–Boron Intermetallics with Strong Interatomic d–sp Orbital Hybridization for High-Performance Electrocatalysis," *Angewandte Chemie - International Edition*, vol. 59, no. 10, pp. 3961–3965, Mar. 2020, doi: 10.1002/anie.201915663.

[62] G. Zhang, X. Zheng, Q. Xu, J. Zhang, W. Liu, and J. Chen, "Carbon nanotube-induced phase and stability engineering: A strained cobalt-doped WSe2/MWNT heterostructure for enhanced hydrogen evolution reaction," *Journal of Materials Chemistry A*, vol. 6, no. 11, pp. 4793–4800, 2018, doi: 10.1039/c8ta00163d.

[63] J. Wang, T. Liao, Z. Wei, J. Sun, J. Guo, and Z. Sun, “Heteroatom-Doping of Non-Noble Metal-Based Catalysts for Electrocatalytic Hydrogen Evolution: An Electronic Structure Tuning Strategy,” *Small Methods*, vol. 5, no. 4. John Wiley and Sons Inc, Apr. 01, 2021. doi: 10.1002/smtd.202000988.

[64] E. Sadeghi, N. S. Peighambardoust, M. Khatamian, U. Unal, and U. Aydemir, “Metal doped layered MgB2 nanoparticles as novel electrocatalysts for water splitting,” *Scientific Reports*, vol. 11, no. 1, Dec. 2021, doi: 10.1038/s41598-021-83066-7.

[65] B. Mete, N. S. Peighambardoust, S. Aydin, E. Sadeghi, and U. Aydemir, “Metal-substituted zirconium diboride (Zr1-xTMxB2; TM = Ni, Co, and Fe) as low-cost and high-performance bifunctional electrocatalyst for water splitting,” *Electrochimica Acta*, vol. 389, Sep. 2021, doi: 10.1016/j.electacta.2021.138789.

[66] V. E. Guterman *et al.*, “PtM/C (M=Ni, Cu, or Ag) electrocatalysts: Effects of alloying components on morphology and electrochemically active surface areas,” *Journal of Solid State Electrochemistry*, vol. 18, no. 5, pp. 1307–1317, 2014, doi: 10.1007/s10008-013-2314-x.

[67] E. Sadeghi, N. S. Peighambardoust, M. Khatamian, U. Unal, and U. Aydemir, “Metal doped layered MgB2 nanoparticles as novel electrocatalysts for water splitting,” *Scientific Reports*, vol. 11, no. 1, Dec. 2021, doi: 10.1038/s41598-021-83066-7.

[68] N. S. Peighambardoust, E. Sadeghi, B. Mete, M. Baris Yagci, and U. Aydemir, “Evaluating electrocatalytic activity of metal-substituted hafnium diboride (Hf1-xTMxB2; TM = Ni and Co) toward water splitting,” *Journal of Alloys and Compounds*, vol. 905, Apr. 2022, doi: 10.1016/j.jallcom.2022.164148.

[69] P. R. Jothi, Y. Zhang, J. P. Scheifers, H. Park, and B. P. T. Fokwa, “Molybdenum diboride nanoparticles as a highly efficient electrocatalyst for the hydrogen evolution reaction,” *Sustainable Energy and Fuels*, vol. 1, no. 9, pp. 1928–1934, 2017, doi: 10.1039/C7SE00397H.